

Nanoscale architecture of cadherin-based cell adhesions

Cristina Bertocchi¹, Yilin Wang^{1,8}, Andrea Ravasio¹, Yusuke Hara¹, Yao Wu¹, Talgat Sailov^{1,8}, Michelle A. Baird^{2,8}, Michael W. Davidson^{2,3,9}, Ronen Zaidel-Bar^{1,4}, Yusuke Toyama^{1,5,6}, Benoit Ladoux^{1,7}, Rene-Marc Mege⁷ and Pakorn Kanchanawong^{1,4,10}

Multicellularity in animals requires dynamic maintenance of cell–cell contacts. Intercellularly ligated cadherins recruit numerous proteins to form supramolecular complexes that connect with the actin cytoskeleton and support force transmission. However, the molecular organization within such structures remains unknown. Here we mapped protein organization in cadherin-based adhesions by super-resolution microscopy, revealing a multi-compartment nanoscale architecture, with the plasma-membrane-proximal cadherin–catenin compartment segregated from the actin cytoskeletal compartment, bridged by an interface zone containing vinculin. Vinculin position is determined by α -catenin, and following activation, vinculin can extend ~ 30 nm to bridge the cadherin–catenin and actin compartments, while modulating the nanoscale positions of the actin regulators zyxin and VASP. Vinculin conformational activation requires tension and tyrosine phosphorylation, regulated by Abl kinase and PTP1B phosphatase. Such modular architecture provides a structural framework for mechanical and biochemical signal integration by vinculin, which may differentially engage cadherin–catenin complexes with the actomyosin machinery to regulate cell adhesions.

The mechanisms by which animal cells self-organize into complex and patterned structures at the tissue and organism levels are intrinsically multiscale, depending on an intricate interplay of local and long-range forces within tissues and cells, as well as exquisite coordination of sub-cellular programs ranging from genetic and signalling pathways to cell morphodynamic behaviours^{1,2}. While recent advances in the understanding of these processes have prominently focused at the length scale of tissues and cells^{3,4}, much has remained unexplored at the level of the very molecular machines that enable intercellular adhesions, cytomechanical adaptation, and mechanotransduction processes underlying these morphogenetic events. Cell–cell junctions mediated by the cadherin transmembrane receptors are among the most important molecular machinery that interlink and coordinate neighbouring cells, participating in important cellular pathways including transcriptional control, cell polarization, cytoskeletal regulation, and cellular mechanotransduction^{5–10}. Adhesions of cadherin recruit numerous proteins, collectively known as ‘cadhesome’¹¹, to form supramolecular complexes closely associated

with the actin cytoskeleton. However, the nanoscale dimension and the compositional complexity of the cadherin adhesions have long defied available structure-determination or imaging techniques, and thus the structural framework for understanding how such complex multi-protein assembly is physically organized to perform biological functions has not been available.

Previously, astigmatism-based three-dimensional (3D) super-resolution microscopy¹² has been applied to resolve nanocluster organization of cadherins in adherens junctions where neighbouring epithelial cells form contact sites^{13,14}. However, the spatial resolution thus attained, >20 – 100 nm, poses a challenge for quantifying protein organization at the sub- 20 nm molecular length scale. Likewise, it has been difficult to decipher molecular organization of cadhesome proteins from electron microscopy images^{15,16}. Therefore, to provide a structural framework for understanding cadherin-based cell adhesions, we adopted a planarized biomimetic platform based on oriented cadherin-F_c arrayed on IgG-coated substrates¹⁷. This format confers a greater optical accessibility amenable to

¹Mechanobiology Institute, Singapore 117411, Republic of Singapore. ²National High Magnetic Field Laboratory, The Florida State University, Tallahassee, Florida 32310, USA. ³Department of Biological Science, The Florida State University, Tallahassee, Florida 32306, USA. ⁴Department of Biomedical Engineering, National University of Singapore, Singapore 117583, Republic of Singapore. ⁵Department of Biological Sciences, National University of Singapore, Singapore 117543, Republic of Singapore. ⁶Temasek Life Sciences Laboratory, National University of Singapore, Singapore 117604, Republic of Singapore. ⁷Institut Jacques Monod, Université Paris Diderot, CNRS UMR 7592, Paris, France. ⁸Present addresses: Department of Biology, South University of Science and Technology, Shenzhen 518055, China (Y.W.); Singapore Centre on Environmental Life Sciences Engineering, Nanyang Technological University, Singapore 637551, Republic of Singapore (T.S.); National Heart Lung and Blood Institute, National Institutes of Health, Bethesda, Maryland 20892, USA (M.A.B.). ⁹Deceased. ¹⁰Correspondence should be addressed to P.K. (e-mail: biekp@nus.edu.sg)

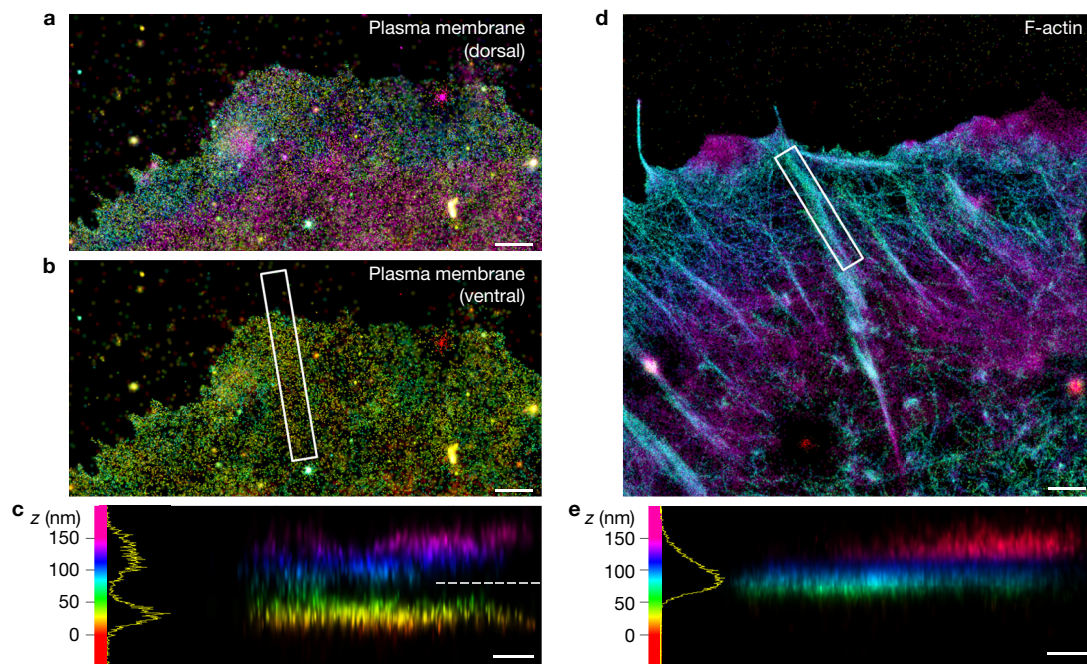


Figure 1 Interferometric photoactivated localization microscopy imaging of plasma membrane marker and F-actin. **(a–c)** The plasma membrane of a MDCK cell labelled by the DiD fluorophore. **(a)** Top view of the dorsal plasma membrane. **(b)** Top view of the ventral plasma membrane ($z < 80$ nm). **(c)** Side view (white box in **b**). **(d,e)** F-actin in a MDCK cell labelled by Alexa Fluor 647

phalloidin. **(d)** Top view. **(e)** Side view of the white box in **d**. Colours (hue scale in **c,e**, 0–150 nm) indicate the vertical (z) coordinate, relative to the substrate surface ($z = 0$ nm, red). The dashed line in **c** marks the $z = 80$ nm threshold used for **b**. Histograms in **c,e** (bin size, 1 nm). Scale bars, 1 μm (**a,b,d**) and 250 nm (**c,e**).

high-precision (sub-20 nm) super-resolution fluorescence microscopy techniques^{18–22}, allowing molecular-scale interrogation with current fluorescent protein (FP) technologies.

In this study, we mapped protein organization within planar cadherin-based adhesions, observing a compartmentalized nanoscale architecture, whereby the plasma membrane-proximal cadherin–catenin compartment is physically segregated by ~ 30 nm from the uppermost compartment containing actin and actin-regulatory proteins, bridged by an interface compartment containing vinculin. We showed that the nanoscale positioning of vinculin is determined by α -catenin. Following conformational activation, vinculin extends ~ 30 nm to bridge the cadherin–catenin and actin compartments, while also modulating the nanoscale positions of the actin polymerization regulators zyxin and VASP. The extended conformation of vinculin requires both tension and tyrosine phosphorylation at residue Tyr822 by Abl kinase, while we also identified PTP1B as the tyrosine phosphatase that dephosphorylates vinculin. The observed multi-layer nanoscale architecture of cadherin-based adhesions appears to centrally position vinculin to act as an integrator of mechanical and biochemical signals, suggesting how the cadherin-based adhesions could selectively engage the actin cytoskeleton in response to regulatory input signals, effectively as a ‘molecular clutch’, to mediate intercellular interactions.

RESULTS

Mapping protein position in planar cadherin-based adhesions by super-resolution microscopy

The multi-micrometre vertical (z) depth of the adherens junctions in epithelial monolayers limited our ability to map molecular-scale organization by astigmatism-based super-resolution microscopy¹⁴

(Supplementary Fig. 1a). We noted that the planar cadherin-coated substrate format has been employed in earlier studies^{17,23–25} to obtain key molecular insights into interactions between cadherin and associated proteins. On this platform cells formed cadherin-based adhesions that recruited cadhesome proteins but not integrin-associated proteins (Supplementary Fig. 1b,c), suggesting that salient protein–protein interactions are probably recapitulated. To demarcate the plasma membrane position in this format, we first applied 3D interferometric photoactivated localization microscopy¹⁹ (Supplementary Fig. 2a,b) to image MDCK (Madin–Darby canine kidney) epithelial cells cultured on E-cadherin-coated substrate, using DiD membrane-targeting fluorophores²⁶. This clearly resolved dorsal and ventral plasma membranes, with the z -position of the latter at ~ 30 – 40 nm above the substrate (Fig. 1a–c). We then imaged filamentous (F)-actin using Alexa Fluor 647 phalloidin, observing that F-actin bundles reside at a higher z -position, centring around ~ 70 – 80 nm, (Fig. 1d,e). The spatial separation of ~ 30 nm between the ventral plasma membrane and the actin cytoskeleton thereby minimizes direct cadherin–actin interaction. The F-actin angle of approach is nearly parallel to the adhesion plane (Supplementary Fig. 3a–d), geometrically comparable to the F-actin orientation around adherens junctions⁴. Altogether, these data are suggestive of the nanoscale similarity between planar cadherin adhesions and native cell–cell contacts.

Nanoscale compartmentalization of E-cadherin-based adhesions

We next applied a surface-generated structured illumination technique^{20,21} (Supplementary Fig. 2c–g) to characterize nanoscale organization of FP-conjugated cadhesome proteins (Supplementary Fig. 4a).

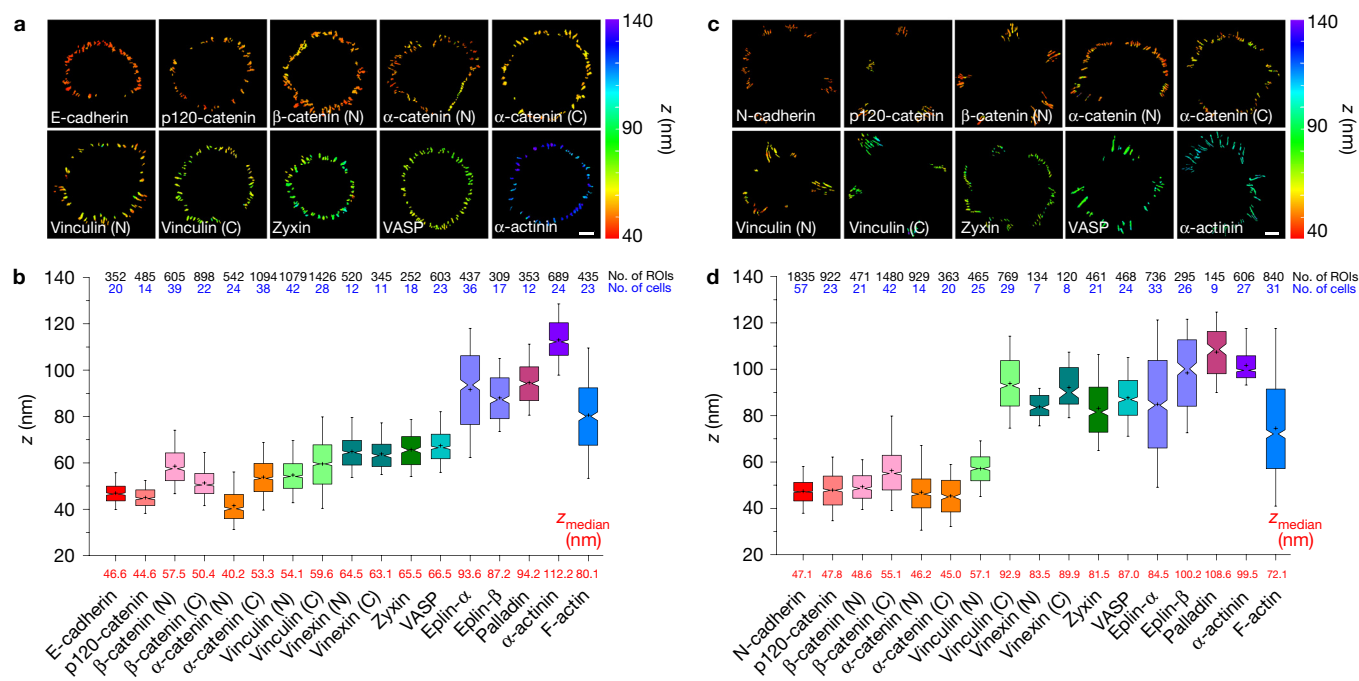


Figure 2 Protein stratifications in MDCK and C2C12 cadherin-based adhesions. **(a,b)** Topographic maps of protein z -positions (nanometres) **(a)** and notched box plots for the z -position of the indicated proteins **(b)** in E-cadherin-based adhesions of MDCK cells. **(c,d)** Topographic maps of protein z -positions (nanometres) **(c)** and notched box plots for the z -position of the indicated proteins **(d)** in N-cadherin-based adhesions of C2C12 cells. The colour bars in **a,c** indicate the z -position relative to the

substrate surface. Scale bars, 10 μm . Notched box plots in **b,d** indicate first and third quartiles, median and confidence intervals; whiskers, 5th and 95th percentiles. Median z_{centre} values are indicated below each box plot (red). n values are shown above each box plot and indicate the numbers of adhesions (number of ROIs, black). Numbers of cells are indicated in blue. Statistics are described in Supplementary Tables 1 and 2.

The fluorophore z -position relative to the substrate surface ($z = 0$ nm) was analysed pixel-wise, with the median value, z_{centre} , for adhesion regions of interest (ROIs) used as the representative protein z -position²⁷, while the z -position histograms denote the spatial distribution of proteins (Fig. 3 and Supplementary Note 1.3 and Supplementary Fig. 2h,i). We observed that E-cadherin (cytoplasmic domain GFP fusion) is positioned at $z_{\text{centre}} = 46.6$ nm, consistent with the dimensions of cadherin and other substrate components (Figs 2b and 3a).

Subsequently, we surveyed the nanoscale organization of key cadhesome proteins, observing a surprising degree of compartmentalization along the z -dimension that effectively spans between the plasma membrane and the actin cytoskeleton. Proteins observed in close proximity to cadherin include p120-catenin (44.6 nm), β -catenin (57.5 nm, amino terminus; 50.4 nm, carboxy terminus), and α -catenin (40.2 nm, N terminus). Their z -positions are consistent with their close association with the E-cadherin cytodomain⁶, thus defining the cadherin–catenin compartment. In contrast, actin-binding proteins were observed at significantly elevated z -positions, largely coinciding with the actin cytoskeleton. Eplins were found at 93.6 nm (α -isoform) and 87.2 nm (β -isoform), palladin at 94.2 nm, and α -actinin at 112.2 nm. A number of proteins were observed at intermediate z -positions, including vinculin (54.1 nm, N terminus), zyxin (65.5 nm), VASP (vasodilator-stimulated protein; 66.5 nm), and vinexin (64.5 nm, N terminus; 63.1 nm, C terminus) (Figs 2a,b and 3a, and Supplementary Fig. 5 and Supplementary Tables 1 and 2). Our measurements suggest that these centrally positioned proteins probably play an important role

as an interface compartment that mediates structural connection and mechanical coupling between the cadherin–catenin and the actomyosin compartments.

The conformation and nanoscale organization of α -catenin

Since α -catenin and vinculin have been implicated as mechanotransducers^{28–31}, we next investigated their configurations and spatial organization within the cadherin adhesions. Using a monoclonal antibody ($\alpha 18$) against the activated conformation of α -catenin³², we observed prominent staining (Fig. 4b and Supplementary Fig. 4d,e) consistent with measurements by a fluorescence resonance energy transfer (FRET) conformation probe⁹ (Fig. 4c and Supplementary Fig. 6d). Furthermore, the high precision of our technique enables inference of protein orientation and/or conformation via the use of the N- and C-terminal FP fusion constructs (Supplementary Note 2 and Supplementary Fig. 5e–h). We thus determined the C-terminal z -position of α -catenin, obtaining $z_{\text{centre}} = 53.3$ nm, compared with $z_{\text{centre}} = 40.2$ nm for the N terminus, indicative of an oriented and activated configuration (Figs 3c–e and 4d and Supplementary Note 3). We next probed the z -position of the α -catenin vinculin-binding domain (VBD) by imaging the vinculin head domain (Vd1, residues 1–258) N-terminal-tagged with GFP, observing the z -position of 57.1 nm closely overlapping with the α -catenin C terminus, consistent with vinculin association to α -catenin (Fig. 4d). To further explore the role of α -catenin in vinculin positioning, we imaged vinculin-FP expressed in MDCK cells with stable α -catenin short hairpin RNA (shRNA) expression³³ (Supplementary Fig. 4b). We found that with α -catenin depleted, vinculin

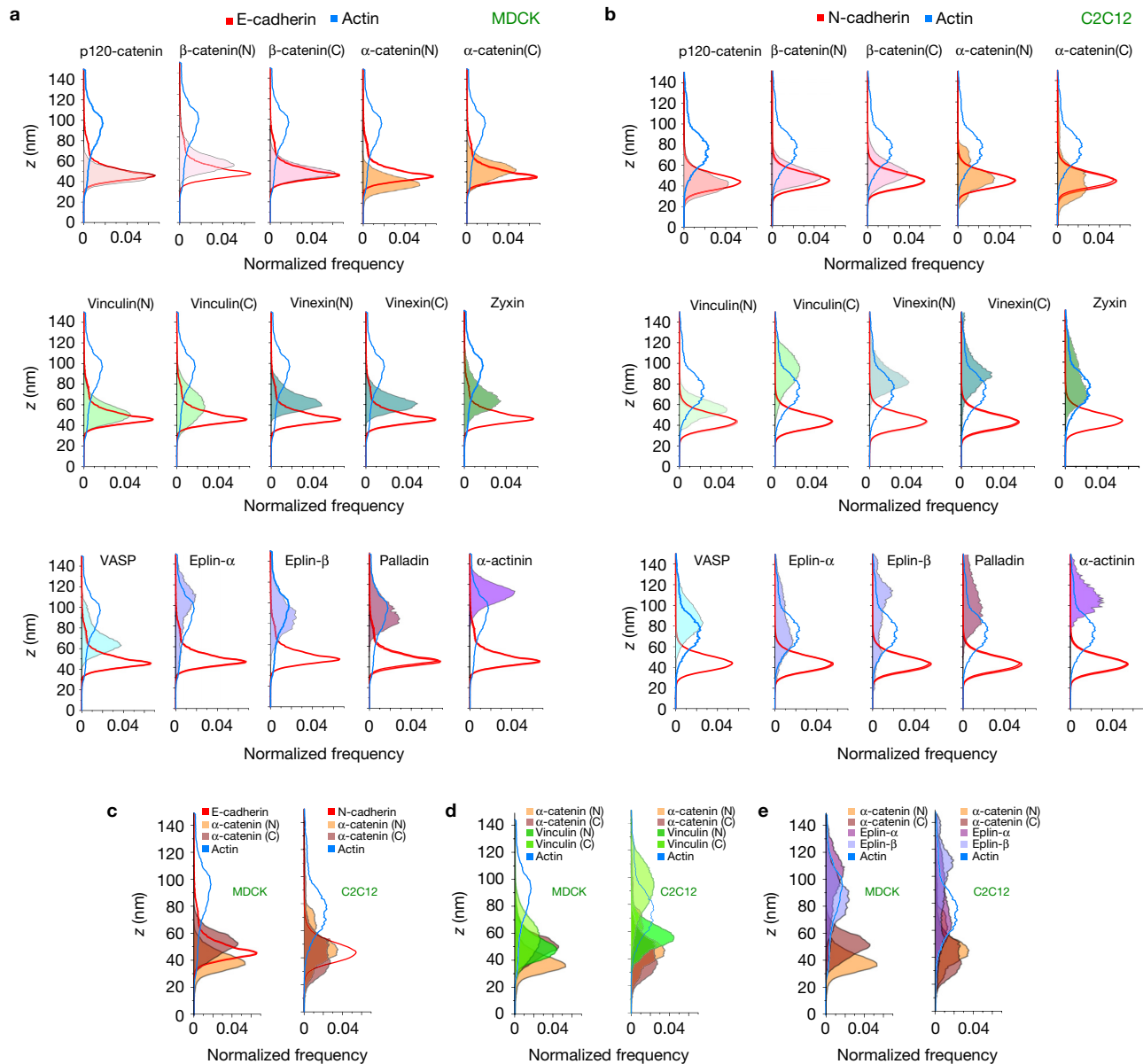


Figure 3 z-dimension profiles of cadhesome proteins. **(a,b)** A normalized histogram of the pixel z-position of the indicated proteins (filled colours) in MDCK **(a)** and C2C12 **(b)** cells, relative to E- or N-cadherin (solid red) and F-actin (solid blue). The integrated areas under each histogram are normalized to unity, such that each histogram reflects the probability

distribution of locating a given protein as a function of the z-position. **(c–e)** A comparison of the protein z-profiles of α -catenin (N- and C-terminal probes, shades of brown) **(c)** and vinculin (N- and C-terminal probes shades of green) **(d)**, or eplins (α and β isoforms, shades of purple) **(e)** between MDCK and C2C12 cells.

localizes to a higher z-position within the actomyosin compartment, probably via the association with actin³⁴ or actin-regulatory proteins such as VASP or α -actinin. On the other hand, following re-expression of α -catenin-FP, the intermediate z-positioning of vinculin is restored (Supplementary Fig. 6a and Supplementary Note 3).

Activated vinculin spans between the cadherin–catenin and actin cytoskeletal compartments

We next characterized how vinculin is organized within the cadherin adhesions. In MDCK, the wild-type (wt) vinculin C terminus was observed at $z_{\text{centre}} = 59.6$ nm, compared with 54.1 nm for the N terminus (Fig. 2b). Since vinculin conformation is able to switch

between the compact and the extended, uninhibited forms, the small N–C z-positional differences observed may correspond to either a relatively compact conformation, or an extended conformation that is oriented nearly parallel to the plasma membrane ($<10^\circ$). To differentiate these, we first probed vinculin configuration by FRET. Using a vinculin tension biosensor (vinculin-TS)²⁹ or a vinculin conformation biosensor³⁵, we observed comparatively high FRET efficiencies, indicative of low vinculin tension and a relatively compact conformation, respectively (Fig. 4f,g and Supplementary Fig. 6b,c,e–h). Additionally, the z-position of the mTFP1 fluorophore within vinculin-TS (Fig. 4a) was mapped to report the z-position of the vinculin linker region, obtaining z_{centre} of 67.6 nm, further

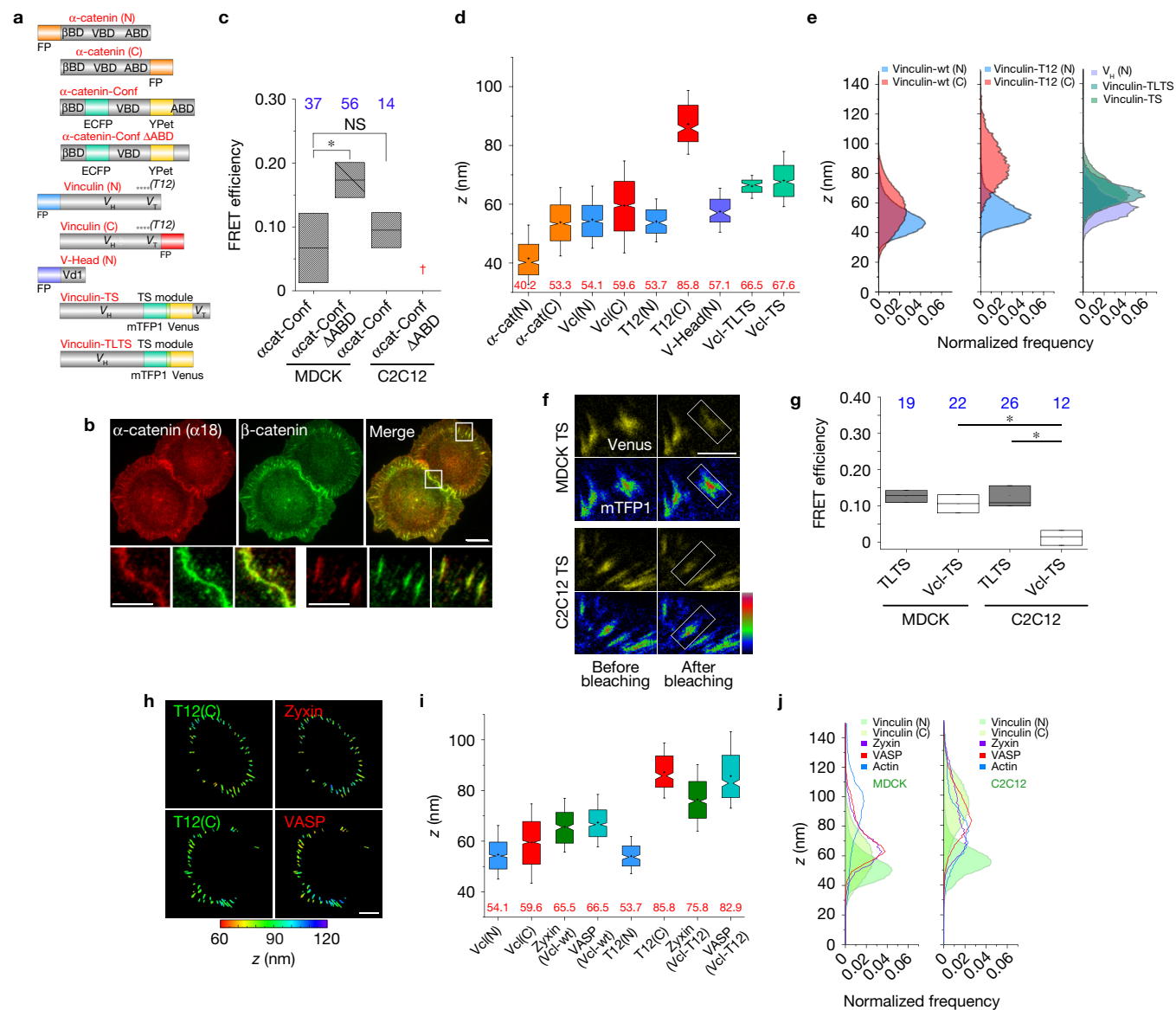


Figure 4 Nanoscale positions and conformations of vinculin and α -catenin in cadherin-based adhesions. **(a)** Diagrams of α -catenin and vinculin probes. FP, fluorescent protein (orange, α -catenin-FP probes; blue, vinculin N terminus; red, vinculin C terminus); α -catenin-conf, α -catenin conformation sensor (teal, ECFP; yellow, YPet); α -catenin-conf Δ ABD, α -catenin conformation sensor with actin-binding domain deletion; β BD, VBD and ABD, binding sites on α -catenin for β -catenin, vinculin and actin, respectively; V_H , V_T , and V_d1 , vinculin head-domain, vinculin tail-domain, and the d1 sub-domain of V_H , respectively; vinculin-TS (Vcl-TS), vinculin tension-sensor (teal, mTFP1; yellow, Venus); vinculin-TLTS, tailless vinculin-TS. ****Approximated positions of point mutations. **(b)** Immunofluorescence for activated α -catenin (α 18) (red) and β -catenin (green) in MDCK cells on E-cadherin substrate. Bottom row, insets zoom-in: native cell–cell contacts and planar cadherin adhesions. Scale bars, $10\mu\text{m}$ (insets, $5\mu\text{m}$). **(c)** FRET efficiency of α -cat-Conf and α -cat-Conf Δ ABD. †Construct did not localize in C212. **(d)** Box plots for z_{centre} of α -catenin and vinculin FP probes in MDCK. **(e)** Z-profiles of vinculin probes in MDCK. N-terminal (blue), C-terminal (red), vinculin-TS and vinculin-TL TS (shades of teal), and vinculin head

domain (V_H , residues 1–258, purple) probes. **(f)** FRET measurement of intra-vinculin tension. MDCK (top) and C2C12 (bottom) cells expressing vinculin-TS, on E- or N-cadherin substrate, respectively. Rainbow look-up table (colour bar) used for donor channel (mTFP1). Scale bar, $5\mu\text{m}$. **(g)** FRET efficiency in MDCK and C2C12. **(h)** Vinculin conformation modulates the position of zyxin and VASP. Topographic map of z-positions: vinculin-T12 C-terminal (left) and zyxin or VASP (right), co-expressed in MDCK cells. Colour bar: z-position relative to substrate surface. Scale bar, $10\mu\text{m}$. **(i)** Box plots for z_{centre} of vinculin, zyxin and VASP (green and teal), with wild-type vinculin (Vcl-wt) or vinculin-T12. **(j)** Comparison of protein z-profiles for vinculin (N- and C-terminal probes, shades of green), zyxin (purple) and VASP (red), overlaid with F-actin z-profile (blue), between MDCK and C2C12 cells. **(c,g)** Box plots for FRET efficiency (acceptor photobleaching): median, 1st and 3rd quartiles. * $P < 0.05$. NS, not significant. Number of cells (n values) in blue. **(d,i)** Notched box plots: 1st and 3rd quartiles, median and confidence intervals; whiskers, 5th and 95th percentiles, with n values (number of adhesions) in Supplementary Table 3.

supporting a compact conformation of vinculin, with the linker region arching upward (Fig. 4d,e and Supplementary Fig. 5e–h and Supplementary Note 2). In contrast, when we probed the orientation

of the constitutively active vinculin-T12 mutant³⁶, we observed a drastic upshift of the C-terminal z-position (85.8 nm) relative to the N terminus (53.7 nm) (Fig. 4d,e). Thus, activated vinculin effectively

spans ~ 30 nm or greater, a distance comparable to the fully extended length of vinculin³⁷. Taken together, these results illustrate how α -catenin emplaces vinculin in the interface zone, a central position that enables activated vinculin to robustly couple the cadherin–catenin with the actomyosin compartments (Supplementary Note 3.4). We also note that a more subtle interplay between α -catenin, β -catenin, and vinculin configuration may also be present (Supplementary Fig. 6a and Supplementary Notes 3.2 and 3.3). Our approach may thus be of further use in unravelling how the cadherin/ β -catenin/ α -catenin module is structurally and mechanically integrated with the cortical actin cytoskeleton^{15,23,28}, an important long-standing question, but which is beyond the scope of the current study.

Vinculin conformation modulates nanoscale position of zyxin and VASP

We next investigated how vinculin conformational states may regulate the spatial organization of other cadhesome components. We performed two-colour nanoscale z -mapping experiments by imaging FP fusion of vinculin partners such as zyxin or VASP, together with vinculin-T12. As shown in Fig. 4h–j, zyxin and VASP, in the presence of endogenous vinculin (wt), were observed at $z_{\text{centre}} = 65.5$ nm and $z_{\text{centre}} = 66.5$ nm, respectively. In contrast, following co-expression with vinculin-T12, we observed significant upshifts in their z -positions with $z_{\text{centre}} = 75.8$ nm for zyxin and $z_{\text{centre}} = 82.9$ nm for VASP. These results suggest that vinculin conformation may modulate the positioning of proteins such as zyxin and VASP that bind to its proline-rich linker region, which may in turn help promote actin polymerization in cadherin adhesions⁵ (Supplementary Note 3.4).

Vinculin conformational switch is regulated by Abl kinase and PTP1B phosphatase

To probe how vinculin conformational transition is regulated, we mapped the C-terminal z -position of vinculin (wt) under various biochemical or pharmacological perturbations. We observed that vinculin remains in the compact state with the overexpression of contractility effectors such as myosin IIA, myosin IIB, activated Src, or constitutively active RhoA. Interestingly, the overexpression of constitutively active Rac1 or cdc42 led to even lower C-terminal z -positions of vinculin of ~ 46 nm, coinciding with the membrane-proximal cadherin–catenin layer (Fig. 5a and Supplementary Table 3). This probably results from the vinculin-tail (V_T) phospholipid interaction³¹, and will be investigated in a more thorough manner separately. Intriguingly, we found that the inhibition of tyrosine phosphatases by orthovanadate results in the upshift of the vinculin C terminus to $z_{\text{centre}} \sim 70$ nm, indicative of a more open conformation whereas the vinculin N terminus remains at $z_{\text{centre}} \sim 54$ nm (Fig. 5b). Since the phosphorylation of vinculin Tyr822 by Abl kinase has recently been shown to be specific to cell–cell contacts³⁸, we mapped vinculin C-terminal z -position following co-treatment of orthovanadate and Gleevec³⁹, a specific Abl kinase inhibitor, observing the reversion of vinculin to the compact conformation ($z_{\text{centre}} = 59.1$ nm, Fig. 5b). In contrast, the vinculin C terminus remains at an elevated z -position following co-treatment of orthovanadate and the Src kinase inhibitor PP2 ($z_{\text{centre}} = 67.8$ nm, Fig. 5b), thus arguing against the involvement of Src kinase. To assess the contribution of the vinculin residue

Tyr822, we expressed vinculin-FP constructs in MDCK cells with stable vinculin shRNA expression³⁴ (vinculin-KD cells, Fig. 5c). For vinculin-wt, we observed similar z -positions of the N and C termini ($z_{\text{centre}} = 56.9$ nm and 56.8 nm, respectively), indicative of a compact conformation as expected. With the non-phosphorylatable mutation Y822F, the C-terminal z -position remained low ($z_{\text{centre}} = 57.5$ nm). In contrast, the phosphomimetic mutation Y822E resulted in the open conformation ($z_{\text{centre}} = 67.8$ nm). Thus, Abl kinase phosphorylation of Tyr822 appears to promote vinculin conformational activation.

Our results also imply that in MDCK, vinculin Tyr822 may be maintained in the unphosphorylated state by an as-yet-unidentified tyrosine phosphatase. Previous studies have documented a few cadherin-associated tyrosine phosphatases such as SHP2 (ref. 40) and PTP1B⁴¹. We therefore assayed for their involvement in vinculin conformational regulation by mapping vinculin C-terminal z -positions in the presence of their specific inhibitors. We observed that vinculin remains compact following treatment with PTP1B inhibitor ($z_{\text{centre}} = 57.9$ nm), but opened up following treatment with RK682, a PTP1B inhibitor, ($z_{\text{centre}} = 68.8$ nm, Fig. 5d). Furthermore, co-treatment of RK682 and Gleevec led to the compact conformation of vinculin. These results therefore implicate the Abl kinase/PTP1B phosphatase switch in regulating vinculin conformational opening in MDCK E-cadherin-based adhesions.

Nanoscale compartmentalization of N-cadherin-based adhesions

We next examined whether the nanoscale stratification of proteins observed in E-cadherin adhesions is present in other classical cadherin adhesions. We mapped cadhesome components in C2C12 mouse myoblast cells, which form N-cadherin-based adhesions when cultured on oriented N-cadherin substrate¹⁷. Remarkably, we observed a comparable extent of nanoscale compartmentalization (Figs 2c,d and 3b and Supplementary Fig. 5c,d). Most prominently, in contrast to the E-cadherin adhesions of MDCK cells, the wild-type vinculin is in a highly extended configuration in C2C12 cells, with the N and C termini at z_{centre} of 57.1 nm and 92.9 nm, respectively. Furthermore, zyxin, VASP and vinexin were also observed at elevated z -positions of 81.5 nm, 87.0 nm and 83.5/89.9 nm (vinexin N/C termini), respectively, supporting the notion that their nanoscale positioning might be vinculin conformation dependent.

Vinculin conformational switch integrates tension and phosphorylation signals to modulate the mechanical properties of cell–cell junctions

The comparatively high tension in C2C12 vinculin as measured by FRET (Fig. 4f,g and Supplementary Fig. 6b,c,d–h,j), together with the extended conformation (Figs 2c,d and 3b), suggests that tension may also promote vinculin activation. Indeed, vinculin-T12 expressed in C2C12 adopts a similarly extended conformation with the C-terminal z -position of 102.0 nm, corroborating the activated state observed for wild-type vinculin (Fig. 5f). To test this further, we treated C2C12 cells with ROCK inhibitor (Y-27632) to reduce tension at the cadherin-based adhesions and imaged the vinculin C-terminal z -position, observing a significant downshift to 64.6 nm, suggestive of a more compact configuration. Interestingly, the treatment of C2C12 by Gleevec also results in a similar extent of z -downshift (69.2 nm).

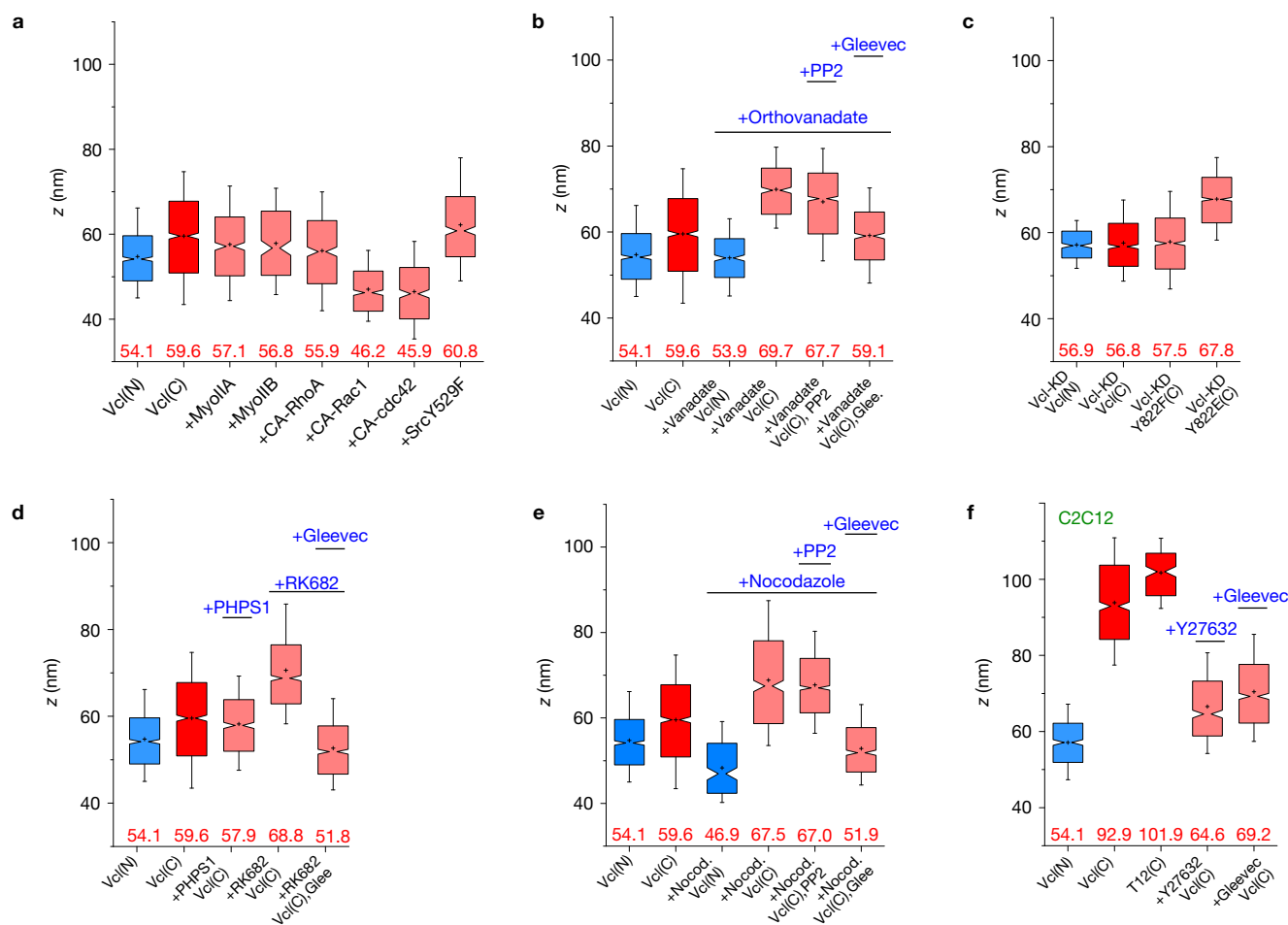


Figure 5 Vinculin conformation is modulated by tyrosine phosphorylation and tension. Notched box plots for vinculin z -positions. Blue and red indicate N- and C-terminal z -positions of WT vinculin, and coral indicates vinculin C-terminal z -position with perturbations. (a) Overexpression of myosin IIA and IIB, constitutively active (CA) RhoGTPases (RhoA, Rac1, cdc42) and Src kinase. (b) Treatment with orthovanadate, PP2 and Gleevec. (c) Vinculin Tyr822 phosphorylation mutants (Y822F, and Y822E) in MDCK vinculin-KD

cells. (d) Treatment with PHPS1, RK682 and Gleevec. (e) Vinculin in MDCK cells, treated with nocodazole and PP2 or Gleevec. (f) Vinculin in C2C12 cells, treated with Y-27632 or Gleevec. Notched boxes in a–f indicate 1st and 3rd quartiles, median and confidence intervals; whiskers, 5th and 95th percentiles. Red numbers in a–f are the median z_{centre} values. n values (number of adhesions) for each box plot, the number of cells, and statistical comparison are described in Supplementary Tables 3 and 4.

In light of these results, we treated MDCK cells with nocodazole, which upregulates contractility via microtubule depolymerization⁴², observing that the vinculin C-terminal z -position upshifted to $z_{\text{centre}} = 67.5$ nm, indicative of a conformational opening (Fig. 5e). Likewise, following co-treatment of nocodazole and Gleevec, vinculin reverted to the compact conformation ($z_{\text{centre}} = 51.9$ nm). Taken together, these results suggest that both tension and Tyr822 phosphorylation may be required for vinculin conformational activation.

We next sought to ascertain whether the native adherens junctions in epithelial monolayers are also regulated by the interplay of vinculin conformation, tension, and Tyr822 phosphorylation as delineated above. Using laser nanoscissor⁴³ to probe tension in cell–cell contacts, we measured the dynamics of recoil following junction scission in MDCK monolayers, observing that the treatment of cells with nocodazole to upregulate tension, or RK682 to inhibit Tyr822 dephosphorylation, resulted in higher initial recoil rates relative to control. Consistent with this, a similar effect is observed with greater recoil rates following the expression of vinculin-T12 or

Y822E, in comparison with the control, vinculin-KD, or Y822F (Fig. 6a–e and Supplementary Tables 6 and 7). Therefore, a similar mechanism probably governs vinculin conformational regulation in both planar cadherin adhesions and native adherens junctions of epithelial monolayers.

DISCUSSION

Our study elucidated how proteins in cadherin-based adhesions are organized to form multi-layered supramolecular complexes that couple cadherin to the actin cytoskeleton. We propose that this stratified architecture (Fig. 6g) may provide the structural framework for regulatory complexity in response to diverse mechanical and signalling cues under different tissue contexts, developmental processes, or disease states^{1–4,6}. For example, how vinculin appears to differentially engage the actin cytoskeleton can be conceptualized in terms of the molecular clutch, while how vinculin conformation is controlled by both mechanical (tension exerted via V_T domain) and biochemical cues (Tyr822 phosphorylation/dephosphorylation by Abl

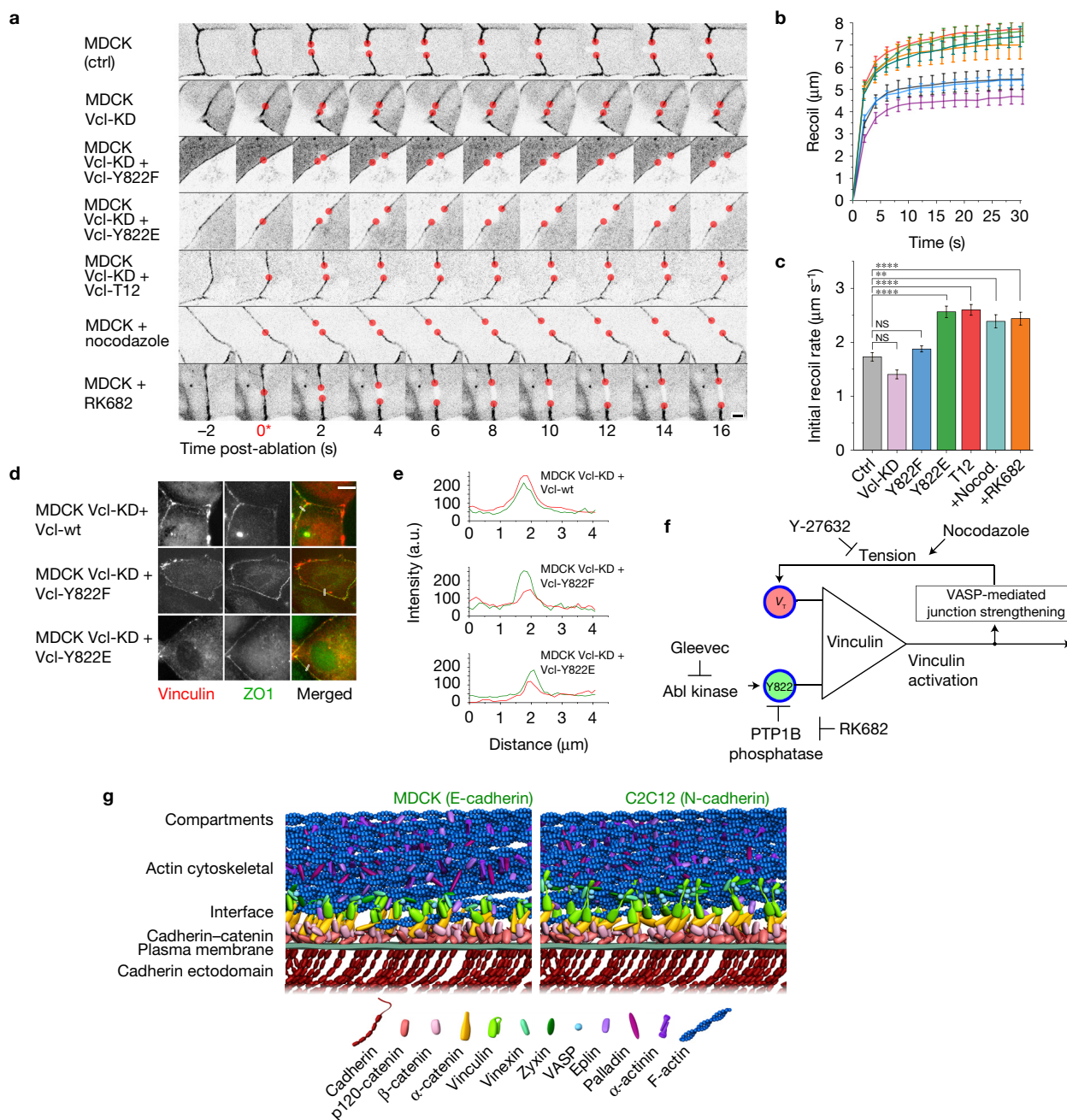


Figure 6 Integration of mechanical and biochemical signals by vinculin regulates mechanical properties of cell–cell contacts. **(a)** MDCK cells were cultured on fibronectin-coated substrate to form confluent monolayers, with cell–cell contacts labelled by ZO-1 fused with either mEmerald or mCherry. Cells were co-transfected with vinculin constructs or treated with pharmacological inhibitors as indicated. A montage of consecutive frames (interval: 2 s) is shown with junction excision at $t=0$ s. Recoiling edges of the junctions (red circles) were used to quantify the recoil trajectory. Untreated MDCK (ctrl) were compared with MDCK stably expressing shRNA against vinculin (MDCK Vcl-KD), MDCK Vcl-KD rescued with Y822F, Y822E, or T12 vinculin mutants, MDCK cells treated with nocodazole (to promote contractility, $10\ \mu\text{M}$ for 1 h), and RK682 (PTP1B inhibitor to inhibit Tyr822 dephosphorylation, $10\ \mu\text{g ml}^{-1}$ for 1 h). Scale bar, $5\ \mu\text{m}$. **(b,c)** Junction recoil **(b)** and initial recoil rate **(c)** following laser ablation of native cell–cell junctions in MDCK epithelial monolayers, with vinculin mutants, or pharmacological treatment. The colours of the plots in **b** correspond to the bar graphs in **c**. Ablation occurred at 0 s. Data in **b**

and **c** represent mean \pm error bars (s.e.m.). $n=19$ (ctrl); 18 (Vcl-KD); 16 (Vcl-KD + Y822F); 17 (Vcl-KD + Y822E); 18 (Vcl-KD + Vcl-T12); 11 (+Nocodazole); 24 (+RK682). $**P < 0.005$, $****P = 5 \times 10^{-5}$. Statistics in Supplementary Tables 6 and 7. **(d)** Fluorescence micrographs of MDCK vinculin KD epithelial monolayers rescued with vinculin wt, vinculin Y822F (non-phosphorylatable), vinculin Y822E (phosphomimetic) fusion constructs to demonstrate their localization at native adherens junctions. Cells were co-transfected with ZO-1 constructs. Scale bar, $10\ \mu\text{m}$. **(e)** Fluorescence intensity line profiles along the lines (white) in **d**, showing co-localization of vinculin (red) with ZO-1 (green) at the cell–cell junctions. **(f)** Diagram of vinculin conformational regulation by tension and Tyr822 phosphorylation, and a putative positive feedback loop. **(g)** Schematic models of protein organization in cadherin-based adhesions, with stratified compartments along the vertical axis at empirically determined z-positions, for MDCK E-cadherin-based adhesions (left, with compact vinculin) and C2C12 N-cadherin-based adhesions (right, with extended vinculin). Note that the model does not depict protein stoichiometry.

kinase/PTP1B phosphatase) (Fig. 6d) is evocative of a rudimentary AND logic gate. Subsequent to both inputs, vinculin activation upshifts the position of proteins such as VASP, probably promoting further actin polymerization and a further increase in vinculin tension⁵, thereby resulting in a positive feedback loop, which may help impart robustness, bi-stability, and tunability⁴⁴.

Interestingly, the nanoscale architecture of the cadherin-based cell adhesions is reminiscent of focal adhesions (FAs) characterized earlier¹⁸. Functionally, both these adhesion types serve to integrate the cortical actin cytoskeletal networks with membrane-anchored receptor complexes. As the integrins and cadherins are fundamentally dissimilar classes of receptors, we suggest that such differences necessitate a centrally positioned protein compartment to serve as a structural and mechanical interface, akin to a universal adaptor, so that the common actomyosin machinery can be coupled with different membrane-bound cell-adhesion apparatuses. Vinculin appears to be properly positioned for such a role, while also possessing an appropriate domain organization, with an actin-binding tail domain (V_T) flexibly linked to the head domain (V_H) that can alternately engage with α - or β -catenin^{45,46}, in cadherin adhesions, or talin, in FAs⁴⁷.

Nevertheless the molecular mechanisms governing vinculin spatial organization appear to diverge between the cadherin adhesions and FAs, despite the comparable stratified architecture. Unlike in FAs, where a large (relative molecular mass of 270,000) and highly elongated protein, talin, plays a dominant structural role comprising the FA core²⁷, directly tethering integrin to actin, in cadherin adhesions such a singularly dominant scaffold is not present. Instead, cadherin-actin linkage appears to be mediated by a plurality of multi-protein complexes. For example, in addition to the cadherin/ β -catenin/ α -catenin complex, α -catenin/Epln⁴⁸ and β -catenin/vinculin⁴⁶ have also been implicated. Furthermore, vinculin stoichiometry probably differs significantly between cadherin adhesions and FAs. In the former, the central placement of vinculin appears to be determined by a single binding site on α -catenin, while in the latter, at least 11 vinculin-binding sites⁴⁹ have been identified in talin. One may conjecture that this difference may reflect the contrasting mechanical context between cell-matrix and cell-cell adhesions. The rigidity of the extracellular matrix spans several orders of magnitude⁵⁰, and thus variable and cooperative interaction between multiple vinculin-binding sites on talin could play a role in fine-tuning FA mechanosensitivity over such a wide dynamic range. On the contrary, cell-cell junction forces are exerted between neighbouring cells, and thus much fewer vinculin-binding sites may be required to respond to the narrower dynamic range of rigidity.

Our data, together with recent studies on vinculin in FAs and cell-cell contacts^{34,38,45}, suggest that the conformational landscape of vinculin may be more complex than a simple two-state on-off model. For example, studies in FAs using FRET biosensors for either conformation or tension revealed that while conformationally open or high-tension vinculin (that is, low FRET efficiency) was highly enriched at adhesion sites, high FRET efficiency vinculin biosensors also localize there^{29,35}, suggesting that conformationally compact or low-tension vinculin is capable of adhesion localization. In cell-cell contacts, our data show that vinculin in a relatively compact, low-tension state is recruited to the MDCK E-cadherin adhesions via activated α -catenin. It is unclear yet how this pool of low-tension

and compact vinculin differs structurally from the autoinhibited cytoplasmic pool. We surmise that vinculin could be partially unfurled such that α -catenin binding is enabled. This allows vinculin to be emplaced in the interface compartment, poised to engage the actin cytoskeleton, while remaining in the unphosphorylated low-tension state due to the prevailing PTP1B activity. The relief of PTP1B enables Abl kinase phosphorylation of Tyr822 and an upward extension of the vinculin C terminus by actomyosin contraction, although the extent of conformational opening in MDCK appears to be lower than fully active, probably due to the low tension generated by this cell type as documented previously²⁸. In contrast, C2C12 vinculin may become fully activated due to both higher contractility and probably lower PTP1B activity (both PTP1B and Abl are expressed in these cell types, Supplementary Fig. 4c). At present, we do not know yet whether such differences reflect cell-type specificity or E-/N-cadherin specificity, and whether Tyr822 phosphorylation actuates vinculin conformational changes directly, or indirectly by recruiting vinculin binding partners to stabilize the open conformation. It is also unclear whether a similar phosphorylation-dependent conformational modulation is operational in FAs, since the Tyr822 phosphorylation is reportedly cell-cell contact specific³⁸. For FAs, the presence of a large number of vinculin-binding sites, such as on talin and paxillin^{31,47}, would probably require the generation of proper molecular tools for a similar conformational analysis to be tractable.

Finally, we note that while the planar cadherin substrate has greatly facilitated nanoscale optical imaging, the adhesions thus formed probably differ from native cell-cell contacts in important aspects such as cadherin mobility, rigidity, and junctional topology, and thus not all aspects of *in vivo* cell-cell junction mechanics may be captured. As such, alternative explanations for the extended conformation of vinculin thus observed may include recruitment of as-yet-unexplored proteins, modulation of affinity to binding partners, indirect effects on cellular contractility, or other changes in protein stability that affect functions. Nevertheless, we suggest that the use of physically well-defined substrate can be highly valuable in revealing molecular-scale behaviours, particularly since native cell-cell contacts often undergo concerted and complicated changes in their mechanical, compositional, and morphological properties following perturbations, which can greatly obfuscate molecular mechanistic dissection. Given the resolution limitation of current super-resolution microscopy methods, an alternative approach to further probe native cell-cell contacts could be via correlative electron microscopy-super-resolution microscopy techniques⁵¹. □

METHODS

Methods, including statements of data availability and any associated accession codes and references, are available in the [online version of this paper](#).

Note: Supplementary Information is available in the online version of the paper

ACKNOWLEDGEMENTS

We thank C. Ajo-Franklin (Lawrence Berkeley National Laboratory), G. Shtengel and H. Hess (Howard Hughes Medical Institute, Janelia Research Campus) for generous help with super-resolution microscopy instrumentation and analysis. We thank H. Chen (Protein Expression Facility, Mechanobiology Institute, Singapore) for generation of mutant constructs, H. T. Ong and A. Sathe (Mechanobiology Institute) for assistance with FRET analysis, C. Zhang (Mechanobiology Institute) for assistance with 3D graphical model, and J. Yan (National University of Singapore)

for critical reading of the manuscript. P.K., C.B., Y.Wang, A.R., T.S. and R.Z.-B. are supported by Singapore National Research Foundation Fellowship awarded to P.K. (NRF-NRFF-2011-04), R.Z.-B. (NRF-RF2009-RF001-074), and Competitive Research Programme (NRF2012NRF-CRP001-084) to P.K. and R.Z.-B. Y.T. is supported by Mechanobiology Institute and National University of Singapore Startup Grants, and a Singapore Ministry of Education Tier 2 grant (MOE2015-T2-1-116). B.L. is supported by the European Research Council under the European Union's Seventh Framework Programme (FP7/2007–2013/ERC grant agreement no. 617233), the Mechanobiology Institute, and the Institut Universitaire de France, and USPC-NUS funding. B.L. and R.-M.M. are also supported by CNRS, the Human Frontier Science Program (grant RGP0040/2012) and Agence Nationale de la Recherche (ANR 2010 Blan1515).

AUTHOR CONTRIBUTIONS

C.B. and Y.Wang performed the super-resolution imaging experiments and conducted data analysis. C.B. and A.R. performed and analysed FRET experiments. C.B., A.R., Y.H. and Y.T. designed and C.B. performed and analysed laser ablation experiments. Y.Wu and R.Z.-B. performed imaging of Eph4 cell–cell junctions by astigmatism-based 3D super-resolution microscopy. C.B., T.S., M.B., M.W.D., B.L. and R.-M.M. designed and generated fusion constructs, and provided new reagents and analytical tools. C.B. and P.K. designed the study and wrote the manuscript. All authors discussed the results and commented on the manuscript.

COMPETING FINANCIAL INTERESTS

The authors declare no competing financial interests.

Published online at <http://dx.doi.org/10.1038/ncb3456>

Reprints and permissions information is available online at www.nature.com/reprints

- Heisenberg, C.-P. & Bellaïche, Y. Forces in tissue morphogenesis and patterning. *Cell* **153**, 948–962 (2013).
- Guillot, C. & Lecuit, T. Mechanics of epithelial tissue homeostasis and morphogenesis. *Science* **340**, 1185–1189 (2013).
- Lecuit, T. & Yap, A. S. E-cadherin junctions as active mechanical integrators in tissue dynamics. *Nat. Cell Biol.* **17**, 533–539 (2015).
- Takeichi, M. Dynamic contacts: rearranging adherens junctions to drive epithelial remodelling. *Nat. Rev. Mol. Cell Biol.* **15**, 397–410 (2014).
- Leerberg, J. M. *et al.* Tension-sensitive actin assembly supports contractility at the epithelial zonula adherens. *Curr. Biol.* **24**, 1689–1699 (2014).
- Leckband, D. & de Rooij, J. Cadherin adhesion and mechanotransduction. *Annu. Rev. Cell Dev. Biol.* **30**, 291–315 (2014).
- Niessen, C. M., Leckband, D. & Yap, A. S. Tissue organization by cadherin adhesion molecules: dynamic molecular and cellular mechanisms of morphogenetic regulation. *Physiol. Rev.* **91**, 691–731 (2011).
- Borghini, N. *et al.* E-cadherin is under constitutive actomyosin-generated tension that is increased at cell–cell contacts upon externally applied stretch. *Proc. Natl Acad. Sci. USA* **109**, 12568–12573 (2012).
- Kim, T. J. *et al.* Dynamic visualization of α -catenin reveals rapid, reversible conformation switching between tension states. *Curr. Biol.* **25**, 218–224 (2015).
- Bertocchi, C., Vaman Rao, M. & Zaidel-Bar, R. Regulation of adherens junction dynamics by phosphorylation switches. *J. Signal Transduct.* **2012**, 125295 (2012).
- Zaidel-Bar, R. Cadherin adhesomes at a glance. *J. Cell Sci.* **126**, 373–378 (2013).
- Huang, B., Wang, W., Bates, M. & Zhuang, X. Three-dimensional super-resolution imaging by stochastic optical reconstruction microscopy. *Science* **319**, 810–813 (2008).
- Truong Quang, B. A., Mani, M., Markova, O., Lecuit, T. & Lenne, P. F. Principles of E-cadherin supramolecular organization *in vivo*. *Curr. Biol.* **23**, 2197–2207 (2013).
- Wu, Y., Kanchanawong, P. & Zaidel-Bar, R. Actin-delimited adhesion-independent clustering of e-cadherin forms the nanoscale building blocks of adherens junctions. *Dev. Cell* **32**, 139–154 (2015).
- Buckley, C. D. *et al.* Cell adhesion. The minimal cadherin-catenin complex binds to actin filaments under force. *Science* **346**, 1254211 (2014).
- Yonemura, S., Itoh, M., Nagafuchi, A. & Tsukita, S. Cell-to-cell adherens junction formation and actin filament organization: similarities and differences between non-polarized fibroblasts and polarized epithelial cells. *J. Cell Sci.* **108**, 127–142 (1995).
- Gavard, J. *et al.* Lamellipodium extension and cadherin adhesion: two cell responses to cadherin activation relying on distinct signalling pathways. *J. Cell Sci.* **117**, 257–270 (2004).
- Kanchanawong, P. *et al.* Nanoscale architecture of integrin-based cell adhesions. *Nature* **468**, 580–584 (2010).
- Shtengel, G. *et al.* Interferometric fluorescent super-resolution microscopy resolves 3D cellular ultrastructure. *Proc. Natl Acad. Sci. USA* **106**, 3125–3130 (2009).
- Ajo-Franklin, C. M., Ganesan, P. V. & Boxer, S. G. Variable incidence angle fluorescence interference contrast microscopy for z-imaging single objects. *Biophys. J.* **89**, 2759–2769 (2005).
- Paszek, M. J. *et al.* Scanning angle interference microscopy reveals cell dynamics at the nanoscale. *Nat. Methods* **9**, 825–827 (2012).
- Bertocchi, C., Goh, W. I., Zhang, Z. & Kanchanawong, P. Nanoscale imaging by superresolution fluorescence microscopy and its emerging applications in biomedical research. *Crit. Rev. Biomed. Eng.* **41**, 281–308 (2013).
- Yamada, S., Pokutta, S., Drees, F., Weis, W. I. & Nelson, W. J. Deconstructing the cadherin-catenin-actin complex. *Cell* **123**, 889–901 (2005).
- Kovacs, E. M., Goodwin, M., Ali, R. G., Paterson, A. D. & Yap, A. S. Cadherin-directed actin assembly: E-cadherin physically associates with the Arp2/3 complex to direct actin assembly in nascent adhesive contacts. *Curr. Biol.* **12**, 379–382 (2002).
- Strale, P.-O. *et al.* The formation of ordered nanoclusters controls cadherin anchoring to actin and cell–cell contact fluidity. *J. Cell Biol.* **210**, 333–346 (2015).
- Shim, S. H. *et al.* Super-resolution fluorescence imaging of organelles in live cells with photoswitchable membrane probes. *Proc. Natl Acad. Sci. USA* **109**, 13978–13983 (2012).
- Liu, J. *et al.* Talin determines the nanoscale architecture of focal adhesions. *Proc. Natl Acad. Sci. USA* **112**, E4864–E4873 (2015).
- Yonemura, S., Wada, Y., Watanabe, T., Nagafuchi, A. & Shibata, M. α -Catenin as a tension transducer that induces adherens junction development. *Nat. Cell Biol.* **12**, 533–542 (2010).
- Grashoff, C. *et al.* Measuring mechanical tension across vinculin reveals regulation of focal adhesion dynamics. *Nature* **466**, 263–266 (2010).
- Yao, M. *et al.* Force-dependent conformational switch of α -catenin controls vinculin binding. *Nat. Commun.* **5**, 4525 (2014).
- Peng, X., Nelson, E. S., Maiers, J. L. & DeMali, K. A. New insights into vinculin function and regulation. *Int. Rev. Cell Mol. Biol.* **287**, 191–231 (2011).
- Nagafuchi, A. & Tsukita, S. The loss of the expression of α catenin, the 102 kD cadherin associated protein, in central nervous tissues during development. *Dev. Growth Differ.* **36**, 59–71 (1994).
- Benjamin, J. M. *et al.* α E-catenin regulates actin dynamics independently of cadherin-mediated cell–cell adhesion. *J. Cell Biol.* **189**, 339–352 (2010).
- Sumida, G. M., Tomita, T. M., Shih, W. & Yamada, S. Myosin II activity dependent and independent vinculin recruitment to the sites of E-cadherin-mediated cell–cell adhesion. *BMC Cell Biol.* **12**, 48 (2011).
- Chen, H., Cohen, D. M., Choudhury, D. M., Kioka, N. & Craig, S. W. Spatial distribution and functional significance of activated vinculin in living cells. *J. Cell Biol.* **169**, 459–470 (2005).
- Cohen, D. M., Chen, H., Johnson, R. P., Choudhury, B. & Craig, S. W. Two distinct head-tail interfaces cooperate to suppress activation of vinculin by talin. *J. Biol. Chem.* **280**, 17109–17117 (2005).
- Milam, L. M. Electron microscopy of rotary shadowed vinculin and vinculin complexes. *J. Mol. Biol.* **184**, 543–545 (1985).
- Bays, J. L. *et al.* Vinculin phosphorylation differentially regulates mechanotransduction at cell–cell and cell–matrix adhesions. *J. Cell Biol.* **205**, 251–263 (2014).
- Nagar, B. *et al.* Crystal structures of the kinase domain of c-Abl in complex with the small molecule inhibitors PD173955 and imatinib (STI-571). *Cancer Res.* **62**, 4236–4243 (2002).
- Ukropec, J. A., Hollinger, M. K., Salva, S. M. & Woolkalis, M. J. SHP2 association with VE-cadherin complexes in human endothelial cells is regulated by thrombin. *J. Biol. Chem.* **275**, 5983–5986 (2000).
- Xu, G., Arregui, C., Lilien, J. & Balsamo, J. PTP1B modulates the association of β -catenin with N-cadherin through binding to an adjacent and partially overlapping target site. *J. Biol. Chem.* **277**, 49989–49997 (2002).
- Chang, Y.-C., Nalbant, P., Birkenfeld, J., Chang, Z.-F. & Bokoch, G. M. GEF-H1 couples nocodazole-induced microtubule disassembly to cell contractility via RhoA. *Mol. Biol. Cell* **19**, 2147–2153 (2008).
- Hara, Y., Shagirov, M. & Toyama, Y. Cell boundary elongation by non-autonomous contractility in cell oscillation. *Curr. Biol.* **26**, 2388–2396 (2016).
- Tsai, T. Y. *et al.* Robust, tunable biological oscillations from interlinked positive and negative feedback loops. *Science* **321**, 126–129 (2008).
- Peng, X., Maiers, J. L., Choudhury, D., Craig, S. W. & DeMali, K. A. α -Catenin uses a novel mechanism to activate vinculin. *J. Biol. Chem.* **287**, 7728–7737 (2012).
- Peng, X., Cuff, L. E., Lawton, C. D. & DeMali, K. A. Vinculin regulates cell-surface E-cadherin expression by binding to β -catenin. *J. Cell Sci.* **123**, 567–577 (2010).
- Critchley, D. R. Biochemical and structural properties of the integrin-associated cytoskeletal protein talin. *Annu. Rev. Biophys.* **38**, 235–254 (2009).
- Abe, K. & Takeichi, M. EPLIN mediates linkage of the cadherin catenin complex to F-actin and stabilizes the circumferential actin belt. *Proc. Natl Acad. Sci. USA* **105**, 13–19 (2008).
- Gingras, A. R. *et al.* Mapping and consensus sequence identification for multiple vinculin binding sites within the talin rod. *J. Biol. Chem.* **280**, 37217–37224 (2005).
- Engler, A. J., Sen, S., Sweeney, H. L. & Discher, D. E. Matrix elasticity directs stem cell lineage specification. *Cell* **126**, 677–689 (2006).
- Shtengel, G. *et al.* Imaging cellular ultrastructure by PALM, iPALM, and correlative iPALM-EM. *Methods Cell Biol.* **123**, 273–294 (2014).

METHODS

Surface modification of imaging substrates by oriented cadherin extracellular domains. Coverglasses (no. 1.5, 18 mm diameter) with pre-embedded plasmonic nanoparticles (Hestzig, LLC) were UV-sterilized for 15 min in a sterile laminar flow hood and rinsed with DPBS. Silicon oxide wafers, p-type (100)-orientation with ~500 nm thermal oxide (Bondatek; Addison Engineering), were pre-treated as described previously²¹, cut into ~1.2 cm × 1.2 cm chips with a diamond-tip pen, pre-rinsed with distilled water, sonicated for 20 min in 100% acetone, rinsed with distilled water, sonicated in 1 M potassium hydroxide, and post-rinsed with distilled water. Both the coverglasses and the silicon wafers were silanized for protein conjugation by incubation with 3-glycidyloxy-propyl-dimethoxymethylsilane (Sigma) (0.045% in 100% ethanol) for 1 h on a shaker at room temperature, and then cured at 110 °C for 1 h. Silanized substrates were rinsed with 70% ethanol and distilled water, and then air-dried. Subsequently, following a previously published protocol¹⁷, the substrates were incubated with goat anti-human or goat anti-mouse F_c fragment specific antibody for E-cadherin and N-cadherin substrate, respectively (Jackson ImmunoResearch, West Grove), at 1 μg cm⁻² in 0.1 M pH 8 borate buffer, and incubated at 4 °C overnight in a humidity chamber. The substrates were then rinsed with PBS and neutralized by NaHCO₃ (100 mM, pH 8.3) and aminoethoxy-ethanol (Sigma) for 1 h. After rinsing with PBS, the substrates were incubated for 2 h with human E-cadherin-F_c or mouse N-cadherin-F_c (R&D system) at 1 μg cm⁻², rinsed with PBS (with Ca²⁺ and Mg²⁺), and blocked with 0.2 % pluronic acid (Sigma) in PBS for 20 min at room temperature.

Cell culture and sample preparation. MDCK (Madin–Darby canine kidney) cells were cultured in DMEM media supplemented with 10% fetal bovine serum (FBS), and 100 units ml⁻¹ of penicillin/streptomycin (Life Technologies). The MDCK cell line with stable α-catenin shRNA expression³³ was a gift from W. J. Nelson (Stanford University, USA). The MDCK cell line with stable vinculin shRNA expression was a gift from S. Yamada (University of California, Davis)³⁴. The Eph4 mouse mammary epithelial cell line was a gift from J.-P. Thiery (IMCB, A-STAR, Singapore). Eph4 cells were cultured in DMEM with 10% FBS and 1% penicillin–streptomycin (complete DMEM). C2C12 (murine myoblast) cells were cultured in DMEM media supplemented with 20% FBS, to maintain the undifferentiated state, and 100 units ml⁻¹ of penicillin/streptomycin. Cells were transfected by electroporation with ~10 μg of endotoxin-free plasmid DNA per ~1 × 10⁶ cells using the Neon transfection system (Life Technologies) according to the manufacturer's protocol, except where indicated otherwise. No cell lines used in this study were found in the database of commonly misidentified cell lines that is maintained by ICLAC and NCBI Biosample. The cell lines were not authenticated. The cell lines used were regularly tested for mycoplasma contamination by PCR methods.

For astigmatism-based 3D super-resolution microscopy (Supplementary Fig. 1a) and wide-field fluorescence microscopy (Supplementary Fig. 4a) of epithelial monolayers, MDCK or Eph4 cells were cultured until confluent on sterile fibronectin-coated no. 1.5 fiducial coverslips (Hestzig LLC). Cells were fixed for 15 min with 4% paraformaldehyde (Electron Microscopy Sciences), rinsed, and blocked by 10% FBS in DPBS. The samples were then permeabilized by 0.2% Triton X-100 in DPBS for 2 min, followed by 1 h incubation at room temperature with the primary antibodies and followed by the secondary antibodies. Primary antibodies used were mouse anti-E-cadherin cytodomain (BD Biosciences) at a dilution of 1:200; mouse anti-β-catenin (Sigma-Aldrich), 1:400; mouse anti-vinculin (Sigma-Aldrich), 1:200; rabbit anti-α-catenin (Abcam), 1:400; and rabbit anti-myosin IIA (Sigma-Aldrich), 1:400. Afterwards, cells were post-fixed for 5 min in 3% PFA with 0.05% glutaraldehyde. Secondary antibodies used were donkey anti-mouse, and goat anti-rabbit, conjugated with Alexa Fluor 488, Alexa Fluor 568, or Alexa Fluor 647 (Life Technologies) at a dilution of 1:400.

For MDCK and C2C12 on planarized cadherin substrates, transfected cells were trypsinized and replated onto the silicon wafers or coverglasses, pre-coated with IgG and cadherin-F_c as described above, and incubated at 37 °C in 5% CO₂. Cells were replated using serum-free medium, since fetal bovine serum contains fibronectin, which may induce integrin-based focal adhesion formation. For the measurements of cell–cell junction recoil following laser ablation, MDCK cells were cultured on fibronectin-coated coverglass prepared by incubating 10 μg ml⁻¹ of bovine fibronectin (F1141, Sigma) in PBS for 1 h at 37 °C in a humidified atmosphere. Cells were transfected with the expression vectors for ZO-1 fused with either mEmerald or mApple as a marker for cell–cell junctions, in conjunction with vinculin constructs as appropriate.

For actin imaging, cytoskeleton buffer (CB: 10 mM MES, pH 6.1, 150 mM NaCl, 5 mM EGTA, 5 mM glucose and 5 mM MgCl₂) was used. Cells were briefly first washed with warm (37 °C) calcium-containing PBS, and pre-fixed by 0.2% glutaraldehyde and 0.1% Triton X-100 in CB for 2 min, followed by 2% glutaraldehyde in CB for 10 min. Afterwards, glutaraldehyde autofluorescence was quenched by incubation for 7 min in freshly prepared 0.1% NaBH₄ in PBS, followed

by three rinses in PBS for 10 min each. Samples were then incubated with 0.33 μM of Alexa Fluor 647 phalloidin (Life Technologies) for either 30 min at room temperature or overnight at 4 °C.

For pharmacological inhibition, cells were treated at the following concentration prior to fixation or laser ablation experiment: sodium orthovanadate (S6508, Sigma), 100 μM; PP2 (P0042, Sigma), 20 μM; Gleevec (imatinib, SML1027, Sigma), 20 μM; PPHS1 (P0039, Sigma), 15 μM; RK682 (RK2033, Sigma), 10 μg ml⁻¹; nocodazole (M1404, Sigma), 10 μM; Y-27632 (Y0503, Sigma), 10 μM. Cells were fixed for imaging ~4–6 h after replating, using 4% paraformaldehyde and stored in PHEM buffer (PIPES 60 mM, HEPES 25 mM, MgCl₂ 2 mM, without EGTA, pH 7.0). Rat monoclonal antibody against activated α-catenin (α18—dilution 1:50) was provided by A. Nagafuchi (Nara Medical University, Japan)³², rabbit anti-β-catenin (ab2365, Abcam) was used at a dilution 1:100 and mouse anti-vinculin (V9131, Sigma) at 1:100. For plasma membrane imaging, live cells were incubated for 1 h at 37 °C with DiD membrane-targeting fluorophore (Life Technologies) at 10 μM in phenol-red free cell culture medium, fixed for 10 min in 4% paraformaldehyde, and quenched with 50 mM NaBH₄ for 12 min.

Three-dimensional super-resolution microscopy by astigmatism-based single-molecule localization. The three-dimensional super-resolution micrographs of adherens junctions shown in Supplementary Fig. 1 were obtained using fixed Eph4 cells mounted in a PBS-based imaging buffer containing oxygen scavenger, made fresh before imaging: 45 mM Tris-HCl, 9.4 mM NaCl, 9% glucose, 100 mM mercaptoethylamine, 0.56 mg ml⁻¹ glucose oxidase, and 0.034 mg ml⁻¹ catalase. The imaging samples were assembled by placing a clean coverslip on top of the cell-containing coverslip. Excess imaging buffer was removed and the samples sealed by nail polish. In cases where cells were cultured on non-fiducial coverglasses, 80–100 nm gold nanoparticles (790122-010, Corpuscular Inc.) were added prior to imaging to serve as fiducial markers for drift correction.

Raw single-molecule fluorescence images of Alexa Fluor 647 blinking were acquired on a Nikon N-STORM microscope, operated by NIS-Elements AR software and equipped with a piezo z stage (Mad City Labs), an Ixon3 EMCCD camera (Andor, Belfast), a cylindrical lens insert, and a motorized TIRF illuminator. Lasers used were fibre-coupled into the illuminator from 640 nm 100 mW and 405 nm 50 mW laser heads. The objective lens used was a Nikon 100× Apo TIRF NA 1.49. Thirty thousand frames were acquired at 30 frames per second for each data set. Since the adherens junctions in Eph4 are typically >2 μm into the sample, fluorophores in the basal region of cells were first illuminated for 5 min with the imaging laser using a low incidence angle for pre-depletion. Subsequently, the adherens junctions were imaged using a highly oblique incidence angle slightly smaller than the critical angle.

Image processing and super-resolution reconstruction were carried out by custom-developed software written in IDL described previously¹⁹. Briefly, each single-molecule peak is fitted to a 2D Gaussian approximation of the point spread function (PSF): $I(x, y) = I_b + I_a e^{-((x-x_c)^2/2s_x^2 - (y-y_c)^2/2s_y^2)}$, where $I(x, y)$ is the best-fit PSF, I_b is the background intensity, I_a is the amplitude, s_x and s_y are the Gaussian widths, and x_c and y_c are the centroid coordinate. The Thompson–Webb uncertainty of the centroid estimate⁵² is determined by: $\sigma_{x,y} = \sqrt{(s^2/N) + ((a^2/12)/N) + (8\pi s^2 b^2/a^2 N^2)}$, where $\sigma_{x,y}$ is the localization uncertainty, s is the peak width, N is the photon number, a is the pixel size, and b is the background photons. A z-coordinate calibration curve was measured by translating the piezo z stage over 2 μm at 25 nm steps, while imaging a fluorescent fiducial, yielding a plot of z versus ellipticity (ϵ), as defined by: $\epsilon = (\sigma_x - \sigma_y)/(\sigma_x + \sigma_y)$, which is then fitted to a polynomial function. Subsequently, z coordinates were extracted for each single molecule using ϵ calculated from the Gaussian fitting⁵³. Super-resolution images were reconstructed using a normalized 2D Gaussian to represent each molecule⁵⁴, with the widths corresponding to σ_x and σ_y . 3D data are rendered with colour encoding the z coordinate¹⁸.

Three-dimensional super-resolution microscopy by interferometric photoactivated localization microscopy (iPALM). The iPALM 3D super-resolution microscope system was built, calibrated, and operated as described earlier^{18,19,51} (Supplementary Fig. 2a). Briefly, a pair of dual-opposed 60× NA 1.49 Apo TIRF (Nikon Instruments) objective lenses were aligned and focused using Picomotors piezoelectric actuators (Newport). The custom-manufactured three-way Hess multiphase beamsplitter (Rocky Mountain Instruments) was positioned by a 5-axis Picomotor actuator (Newport). Optimal mutual phase interference was adjusted by a dielectric mirror on a z-tip-tilt piezoelectric mount (Physik Instrument), index-matched to the beamsplitter⁵¹. All major optical parts are mounted on custom-machined Invar parts to minimize drift. Three deep-cooled back-illuminated EMCCD cameras (Ixon Ultra, Andor) were used for acquisition of raw images in frame transfer mode (50 ms exposure time), each controlled by a dedicated computer. Room-temperature control was overridden prior to experiments by a custom-installed switch and allowed to equilibrate for minimal temperature fluctuation. Calibration,

alignment, and acquisition were performed using custom-written codes in LabVIEW (National Instruments), while image processing and data analysis were performed using custom-written IDL software, described previously^{18,19}. Light sources for excitation and photoswitching were 642 nm 100 mW and 405 nm 100 mW lasers (Coherent), respectively, with intensity and timing controlled by an AOTF (A-A Optoelectronics). Emission filters used for each camera are BrightLine FF01-676/37 and a 4-band notch filter, NF03-405488/561/635E-25 (Semrock), to reject stray excitation light. PHEM buffer supplemented with 100 mM cysteamine to promote blinking was used as the imaging buffer. Samples were sealed by epoxy and vaseline-paraffin mixture and mounted on a custom-machined stainless-steel holder equipped with dual piezo actuators (Physik Instruments). The *z*-coordinate was determined from a calibration curve recorded pre-acquisition for each imaging site by scanning the piezo sample holder in 8-nm steps (Supplementary Fig. 2b). Channel registration and drift correction was performed using plasmonic fiducials immobilized in coverglasses, while super-resolution images were reconstructed using hue-encoding for the *z* coordinate and normalized Gaussian as described previously¹⁸.

Nanoscale-precision *z*-position measurement by surface-generated structured illumination. The theoretical foundation and implementations of protein *z*-position mapping by surface-generated structured illumination techniques (variable incidence angle fluorescence interference contrast microscopy, or scanning angle interference microscopy) were described previously^{20,21}, and were performed on a Nikon Eclipse Ti inverted microscope (Nikon Instruments), with a motorized TIRF illuminator, a 60× NA 1.49 ApoTIRF objective lens, a sCMOS camera (Orca Flash 4.0, Hamamatsu), and a laser combiner (488 nm and 561 nm, Omicron Laserage) coupled with a polarization-maintaining optical fibre. The thermal oxide thickness of each batch of silicon wafers was determined to nanometre-precision using an ellipsometer (UV-VIS-VASE, JA-Woollam) at the Institute of Materials Research and Engineering, A-STAR, Singapore.

For imaging, the sample side of the silicon wafer was placed into a PBS-filled 27-mm glass-bottom dish (Iwaki), facing downward, maintained at neutral buoyancy by a thumb screw²⁷. Raw fluorescence image series were acquired at 4° incidence angle interval between 0° (normal) and 52°, as described previously²⁷, using pre-tabulated values for either 488 nm (for EGFP, mTFP1, or mEmerald) or 561 nm laser (for mCherry, mApple, or photoconverted EosFP), with a typical exposure time of 100–200 ms per frame. As needed, photoconversion of mEos2 and tEOS was carried out using LED excitation and a DAPI filter set (Lumencor SOLA). Two-colour measurements were performed sequentially. Analysis was performed using IDL-based custom-written software (available upon request). Simple or Otsu thresholding was used to generate binary masks for regions of interest (ROIs). Topographic height (*z*) and other model parameters were determined by Levenberg–Marquardt nonlinear least-square fitting, with multiple initial guesses for exhaustive search, for each pixel in the ROI²⁷. The median *z*-position value of each ROI was denoted z_{centre} , and used as the representative *z*-position for a given ROI. The representative protein positions, z_{median} , were obtained from the distributions of z_{centre} , such as shown in Supplementary Fig. 2h and Supplementary Fig. 5a,c. Alternative, histograms were calculated using the *z*-position of all pixels, and normalized with the integrated area set to unity to reflect the probability distribution of locating a protein as a function of *z*-position (Figs 3 and 4e,j and Supplementary Fig. 2i). Topographic *z* maps were plotted using colour to encode the *z*-position.

Fluorescent protein fusion constructs. The E-cadherin-EGFP expression vector was a gift from W. J. Nelson (Stanford University, USA). N-cadherin-EGFP was obtained from the Addgene depository (no. 18870, contributed by V. Vasioukhin, Fred Hutchinson Cancer Center, USA). The mouse α_6 -catenin expression vector was created in the laboratory of R.-M.M. (Université Paris Diderot/CNRS, France), based on a previously described vector²⁵, as a dual tag construct with EGFP at the N terminus and mCherry at the C terminus in the pEGFP-C2 vector, via recombination of overlapping PCR products (Infusion, Clontech). Based on this, a dual tag construct with mApple at the N terminus and EGFP at the C terminus was also generated using a forward primer 5'-AAAAAAGGATCCCTGTCAGCTCGCCACCA TGGTGAGCAAGGGCGAG-3' and reverse primer 5'-GGGCCGAATTCTCT TGTACAGCTCGTCCATGC-3', for AgeI and EcoRI restriction sites. Forward primer 5'-AAAAAAGCGATCGGGTGGATGTTGAGCAAGGGCGAGGA-3' and reverse primer 5'-AAAAAAGGATCCCTGTCAGCTCGTCCATGC-3' were used for PvuII and BamHI restriction sites for the cloning of EGFP to the C terminus of α_6 -catenin. The α -catenin conformational FRET sensor⁹ and α -catenin delta ABD (actin-binding domain) FRET sensor were generously provided by Y. Wang (University of California, USA). N- and C-terminal EGFP fusions of β -catenin were provided by R. Kypta (MRC Laboratory for Molecular Cell Biology, University College London, UK) and described previously⁵⁶. EGFP fusion of p120-catenin was obtained from Reynolds laboratory, Vanderbilt University, Nashville,

Tennessee, and described previously⁵⁷. FP fusion constructs of vinculin, zyxin, VASP, vinexin, palladin, myosinIIA, myosinIIB, α -actinin, and ZO-1 were created in the laboratory of M.W.D., The Florida State University, and are available from Addgene depository.

EGFP-vinculin head (residues 1–258), the N-terminal fusion of vinculin-T12, and Vinculin 'tail-probe' conformational FRET sensor³⁵ were obtained from Addgene (no. 46270, no. 46266 and no. 46268 contributed by S. Craig, Johns Hopkins University, USA). The vinculin FRET-based tension sensor (TS) and tailless-tension sensor²⁹ were obtained from Addgene (no. 26019 and 26020, contributed by M. Schwartz, Yale University, USA). The C-terminal fusion of vinculin-T12 and the Y822E and Y822F mutants of vinculin were generated by H. Chen (MBI Protein Expression Facility, Singapore). Briefly, forward primer 5'-CCCTCGAGATGCCCGTCTTCCACACGC-3' and reverse primer 5'-CGGAATTGCTGATACCATGGGGTTC-3', for XhoI and EcoRI sites, were used for the creation of the vinculin-T12 C-terminal fusion. The primer 5'-TTTCGGATCTGGGAGCTGTGGCCAAG-3' was used for the Y822F (the reverse primer is the same as for Y822E) mutagenesis based on wt-vinculin C-terminal fusion construct Y822E. EGFP fusions of the Eplin α and β isoforms were obtained from Addgene (no. 40947-8, contributed by E. Luna, University of Massachusetts Medical School, USA). RhoA-V12-EGFP construct was a gift from M. Sheetz (Mechanobiology Institute, Singapore). Rac1-V12-BFP and cdc42-Q61L-EGFP were gifts from C. Waterman (National Institutes of Health). Src Y529F was obtained from Addgene (no. 17686, contributed by D. Shalloway, Cornell University, USA). All constructs created in-house were verified by sequencing. Localizations to the cell–cell junctions were verified in MDCK or C2C12 cells plated on fibronectin, cultured to confluence, and imaged by epifluorescence microscopy (Supplementary Fig. 4a,f).

Western blot analysis. Whole-cell lysates of MDCK cells (control), MDCK with stable expression of shRNA against vinculin (Vcl-KD)³⁴ or α -catenin (α -catenin KD)³³ and C2C12 cells were prepared in 1× RIPA lysis buffer (Pierce) supplemented with 1× protease inhibitor cocktail (04693159001, Roche). Cells were freeze–thawed thrice at –80 °C and clarified by centrifugation at 4 °C at 14,000 r.p.m. (21,000g) for 20 min. Protein amounts in the supernatants were quantified by the BCA Pierce kit (Thermo Scientific). Thirty micrograms was separated via SDS–PAGE using 4–15% Mini-PROTEAN TGX Precast Protein Gels (Bio-Rad) and transferred to Immobilon-P PVDF (poly-vinylidene fluoride) membranes. The membranes were blocked for 1 h at room temperature with 5% non-fat dry milk (wt/vol) in TBS-T buffer (0.1% vol/vol of Tween-20 in 1× TBS buffer solution, no. 1706435 Bio-Rad), and were subsequently incubated for 1 h at room temperature or overnight at 4 °C with antibodies in 3% non-fat dry milk (wt/vol) in TBS-T buffer. Antibodies used were: vinculin (V9131, Sigma), 1:5,000; α -catenin (EP1793Y, Sigma), 1:10,000; Abl kinase (no. ab15130, Abcam), 1:500; PTP1B (no. ab124375, Abcam), 1:500; and α -tubulin (Abcam ab18251), 1:5,000. After primary antibody incubation, the membranes were washed once in TBS-T, once in 2.5% non-fat dry milk (wt/vol) in TBS-T buffer, and once in 5% non-fat dry milk (wt/vol) in TBS-T buffer (10 min each). After the washing steps, the membranes were incubated with the appropriate horse radish peroxidase-conjugated antibodies in 3% non-fat dry milk (wt/vol) in TBS-T buffer at a dilution of 1:5,000. After secondary antibody incubation, membranes were washed three times in TBS-T (10 min each). The membranes were then incubated for 3–5 min with SuperSignal West Pico Chemiluminescent Substrate and imaged using the Chemidoc MP Gel Documentation System (Bio-Rad). In case of PVDF membrane reprobing by different antibodies, the membranes were stripped using Restore Western Blot Stripping Buffer (21059, Thermo Scientific) for 15 min, washed in TBS-T for 10 min, and blocked in 5% non-fat dry milk (wt/vol) in TBS-T buffer at 4 °C overnight.

Preparation of compliant substrates. Soft substrates, used for FRET experiments, were generated using Cy52-276 silicone (Dow Corning). The two components (A and B) of the silicone were mixed at 1:1 ratio (w/w). Approximately 50 μ l of the viscous mixture was placed in the centre of a coverglass and spread into a thin film by a spin-coater (1 min at 800 r.p.m.) to achieve a thickness of ~50 μ m. The silicone gel was allowed to crosslink for 2 h at 80 °C to obtain a final Young's modulus of ~15 kPa (ref. 58). The silicon-coated glass coverslips were then treated for E- or N-cadherin deposition as described above.

Forster resonance energy transfer (FRET) measurements. The method of acceptor photobleaching was used to measure the FRET efficiency for intramolecular tension in vinculin (Vinculin-TS)²⁹, conformational change in the vinculin tail region (tail-probe)³⁵, and conformational change in α -catenin⁹. These constructs rely on FRET between the donor in the cyan fluorescent protein channel (mTFP1, CFP or ECFP) and the acceptor in the yellow fluorescent protein channel (YFP, YPet or Venus). MDCK and C2C12 cells were transfected with the FRET sensors or their respective control constructs, and cultured on E- or N-cadherin substrates described above. Imaging was performed using a Nikon Eclipse Ti-E inverted microscope

(Nikon) equipped with a spinning-disc confocal unit, CSU-W1 (Yokogawa), an iLas² illumination system, and a ProEM HS EMCCD camera (Princeton instruments). The objective lens used was a CFI Plan Apo 100× NA 1.45 oil immersion (Nikon).

Nine consecutive images were acquired every two seconds using the settings shown in Supplementary Table 4. Cross-excitation and cross-emission between channels were determined to be negligible. After the fourth acquisition, acceptor photobleaching in an ROI was carried out by scanning the 514 nm laser at 10 mW power for 180 ms. Acquired images were background subtracted and thresholded to segment for cadherin adhesions. Donor and acceptor images were adjusted for structural photobleaching⁵⁹. FRET efficiency extrapolated for full acceptor photobleaching (extFRETEff) was calculated⁶⁰ as follows: $\text{extFRETEff} = 1 - (\alpha \times D^b / (D^a - (\beta \times D^b)))$, where D^b and D^a are the intensities of the donor before (second acquisition) and after acceptor photobleaching (third acquisition), respectively. α and β are the correction factors and are calculated as follows: $\alpha = 1 - \beta$, and $\beta = (A^a / A^b)$, where A^b and A^a are the intensities of the acceptor before (second acquisition) and after (third acquisition) photobleaching, respectively.

Laser ablation of cell–cell junctions. Cell–cell junctions in MDCK epithelial monolayers were selectively excised by UV laser nanoscissor ablation performed on a Nikon A1R MP laser scanning confocal microscope, equipped with an ultraviolet laser (PowerChip PNV-0150-100, Team Photonics: 355 nm, 300 ps pulse duration, 1 kHz repetition rate). The UV laser beam was merged onto the optical axis via a customized optical path and a dichroic filter, with the beam controlled independently from the microscope to allow simultaneous ablation and imaging. The beam position was steered by a mirror mounted on two linear actuators (TRA12CC), adjusted via an actuator controller (ESP301-3G). The exposure time was controlled by a mechanical shutter (VS25S2ZM0, Uniblitz). A custom ImageJ plug-in was used to control both the actuators and the shutter⁶¹. Laser ablation was carried out at the z -plane of adherens junctions using 15 nW laser power focused at the back aperture of the objective lens with an exposure time of 350 ms. Time-lapse confocal images were acquired every 2 s, starting from 3 frames prior to the ablation until 30 frames post-ablation with a scan speed of 1 frame s⁻¹, and a pinhole size of 74 μm .

Image analysis of the recoil speed was performed in ImageJ using the MTrackJ plug-in⁶². This plug-in allows the tracking of the two edges of the cut in subsequent frames and extracts the coordinates of the two points of time. The recoil speed ($\mu\text{m s}^{-1}$) was defined as the rate of change of the two edges⁶³. The initial recoil speeds were measured using the first 2 s after ablation.

Statistics and reproducibility. Plotting and statistical analysis for super-resolution z -position measurements and FRET (Welch's t -test), and laser ablation data (one-way ANOVA, followed by pairwise Tukey test), were performed using OriginPro software (Northampton). For protein z -position, data are presented as the median, with the full distribution shown in Fig. 3 and Supplementary Fig. 5, and the mean, median, and standard deviation, and n values (number of adhesions) in

Supplementary Tables 1–3. P values (Welch's t -test) are indicated in Supplementary Table 4. For laser ablation experiments, the mean, standard deviation, s.e.m., and n are indicated in Supplementary Table 6, with pairwise Tukey test in Supplementary Table 7. Differences were considered significant at $P < 0.05$ (as stated in each individual figure legend). Western blots and immunofluorescence microscopy were performed with at least three independent repeats. All representative microscopy images are presented with quantification of the entire data set. Detailed information on replication of experiments can be found indicated on the plots and in their corresponding legends. For determination of sample size, s.d. from initial trials was used to estimate the sample size based on confidence interval calculations at confidence levels of 95%. The number of adhesions analysed was assessed from 9–30 cells from at least 3 independent sample preparations per condition.

Code availability. Computation code used in this study is available from the corresponding author on request.

Data availability. All data supporting the conclusions are available from the corresponding author on request.

52. Thompson, R. E., Larson, D. R. & Webb, W. W. Precise nanometer localization analysis for individual fluorescent probes. *Biophys. J.* **82**, 2775–2783 (2002).
53. Brown, T. A. *et al.* Superresolution fluorescence imaging of mitochondrial nucleoids reveals their spatial range, limits, and membrane interaction. *Mol. Cell. Biol.* **31**, 4994–5010 (2011).
54. Betzig, E. *et al.* Imaging intracellular fluorescent proteins at nanometer resolution. *Science* **313**, 1642–1645 (2006).
55. Thomas, W. A. *et al.* α -Catenin and vinculin cooperate to promote high E-cadherin-based adhesion strength. *J. Biol. Chem.* **288**, 4957–4969 (2013).
56. Giannini, A. L., Vivanco, M. M. & Kypta, R. M. Analysis of β -catenin aggregation and localization using GFP fusion proteins: nuclear import of α -catenin by the β -catenin/Tcf complex. *Exp. Cell Res.* **255**, 207–220 (2000).
57. Roczniak-Ferguson, A. & Reynolds, A. B. Regulation of p120-catenin nucleocytoplasmic shuttling activity. *J. Cell Sci.* **116**, 4201–4212 (2003).
58. Rivasio, A. *et al.* Regulation of epithelial cell organization by tuning cell–substrate adhesion. *Integr. Biol.* **7**, 1228–1241 (2015).
59. Hodgson, L., Nalbant, P., Shen, F. & Hahn, K. Imaging and photobleach correction of Mero-CBD, sensor of endogenous Cdc42 activation. *Methods Enzymol.* **406**, 140–156 (2006).
60. Jobin, C. M. *et al.* Receptor-regulated dynamic interaction between endothelial nitric oxide synthase and calmodulin revealed by fluorescence resonance energy transfer in living cells. *Biochemistry* **42**, 11716–11725 (2003).
61. Hutson, M. S. *et al.* Forces for morphogenesis investigated with laser microsurgery and quantitative modeling. *Science* **300**, 145–149 (2003).
62. Meijering, E., Dzyubachyk, O. & Smal, I. Methods for cell and particle tracking. *Methods Enzymol.* **504**, 183–200 (2012).
63. Rivasio, A. *et al.* Gap geometry dictates epithelial closure efficiency. *Nat. Commun.* **6**, 7683 (2015).

Nanoscale architecture of cadherin-based cell adhesions

Cristina Bertocchi¹, Yilin Wang^{1,8}, Andrea Ravasio¹, Yusuke Hara¹, Yao Wu¹, Talgat Sailov^{1,8}, Michelle A. Baird^{2,8}, Michael W. Davidson^{2,3,9}, Ronen Zaidel-Bar^{1,4}, Yusuke Toyama^{1,5,6}, Benoit Ladoux^{1,7}, Rene-Marc Mege⁷ and Pakorn Kanchanawong^{1,4,10}

Multicellularity in animals requires dynamic maintenance of cell–cell contacts. Intercellularly ligated cadherins recruit numerous proteins to form supramolecular complexes that connect with the actin cytoskeleton and support force transmission. However, the molecular organization within such structures remains unknown. Here we mapped protein organization in cadherin-based adhesions by super-resolution microscopy, revealing a multi-compartment nanoscale architecture, with the plasma-membrane-proximal cadherin–catenin compartment segregated from the actin cytoskeletal compartment, bridged by an interface zone containing vinculin. Vinculin position is determined by α -catenin, and following activation, vinculin can extend ~ 30 nm to bridge the cadherin–catenin and actin compartments, while modulating the nanoscale positions of the actin regulators zyxin and VASP. Vinculin conformational activation requires tension and tyrosine phosphorylation, regulated by Abl kinase and PTP1B phosphatase. Such modular architecture provides a structural framework for mechanical and biochemical signal integration by vinculin, which may differentially engage cadherin–catenin complexes with the actomyosin machinery to regulate cell adhesions.

The mechanisms by which animal cells self-organize into complex and patterned structures at the tissue and organism levels are intrinsically multiscale, depending on an intricate interplay of local and long-range forces within tissues and cells, as well as exquisite coordination of sub-cellular programs ranging from genetic and signalling pathways to cell morphodynamic behaviours^{1,2}. While recent advances in the understanding of these processes have prominently focused at the length scale of tissues and cells^{3,4}, much has remained unexplored at the level of the very molecular machines that enable intercellular adhesions, cytomechanical adaptation, and mechanotransduction processes underlying these morphogenetic events. Cell–cell junctions mediated by the cadherin transmembrane receptors are among the most important molecular machinery that interlink and coordinate neighbouring cells, participating in important cellular pathways including transcriptional control, cell polarization, cytoskeletal regulation, and cellular mechanotransduction^{5–10}. Adhesions of cadherin recruit numerous proteins, collectively known as ‘cadhesome’¹¹, to form supramolecular complexes closely associated

with the actin cytoskeleton. However, the nanoscale dimension and the compositional complexity of the cadherin adhesions have long defied available structure-determination or imaging techniques, and thus the structural framework for understanding how such complex multi-protein assembly is physically organized to perform biological functions has not been available.

Previously, astigmatism-based three-dimensional (3D) super-resolution microscopy¹² has been applied to resolve nanocluster organization of cadherins in adherens junctions where neighbouring epithelial cells form contact sites^{13,14}. However, the spatial resolution thus attained, >20 – 100 nm, poses a challenge for quantifying protein organization at the sub- 20 nm molecular length scale. Likewise, it has been difficult to decipher molecular organization of cadhesome proteins from electron microscopy images^{15,16}. Therefore, to provide a structural framework for understanding cadherin-based cell adhesions, we adopted a planarized biomimetic platform based on oriented cadherin-Fc arrayed on IgG-coated substrates¹⁷. This format confers a greater optical accessibility amenable to

¹Mechanobiology Institute, Singapore 117411, Republic of Singapore. ²National High Magnetic Field Laboratory, The Florida State University, Tallahassee, Florida 32310, USA. ³Department of Biological Science, The Florida State University, Tallahassee, Florida 32306, USA. ⁴Department of Biomedical Engineering, National University of Singapore, Singapore 117583, Republic of Singapore. ⁵Department of Biological Sciences, National University of Singapore, Singapore 117543, Republic of Singapore. ⁶Temasek Life Sciences Laboratory, National University of Singapore, Singapore 117604, Republic of Singapore. ⁷Institut Jacques Monod, Université Paris Diderot, CNRS UMR 7592, Paris, France. ⁸Present addresses: Department of Biology, South University of Science and Technology, Shenzhen 518055, China (Y.W.); Singapore Centre on Environmental Life Sciences Engineering, Nanyang Technological University, Singapore 637551, Republic of Singapore (T.S.); National Heart Lung and Blood Institute, National Institutes of Health, Bethesda, Maryland 20892, USA (M.A.B.). ⁹Deceased. ¹⁰Correspondence should be addressed to P.K. (e-mail: biekp@nus.edu.sg)

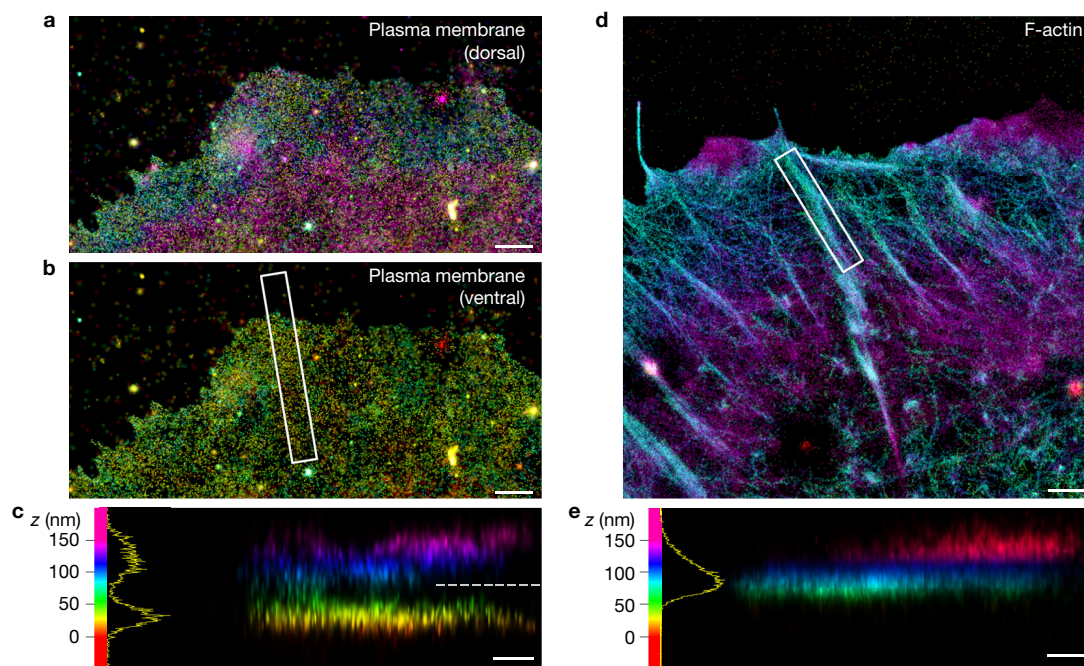


Figure 1 Interferometric photoactivated localization microscopy imaging of plasma membrane marker and F-actin. (**a–c**) The plasma membrane of a MDCK cell labelled by the DiD fluorophore. (**a**) Top view of the dorsal plasma membrane. (**b**) Top view of the ventral plasma membrane ($z < 80$ nm). (**c**) Side view (white box in **b**). (**d,e**) F-actin in a MDCK cell labelled by Alexa Fluor 647

phalloidin. (**d**) Top view. (**e**) Side view of the white box in **d**. Colours (hue scale in **c,e**, 0–150 nm) indicate the vertical (z) coordinate, relative to the substrate surface ($z = 0$ nm, red). The dashed line in **c** marks the $z = 80$ nm threshold used for **b**. Histograms in **c,e** (bin size, 1 nm). Scale bars, 1 μm (**a,b,d**) and 250 nm (**c,e**).

high-precision (sub-20 nm) super-resolution fluorescence microscopy techniques^{18–22}, allowing molecular-scale interrogation with current fluorescent protein (FP) technologies.

In this study, we mapped protein organization within planar cadherin-based adhesions, observing a compartmentalized nanoscale architecture, whereby the plasma membrane-proximal cadherin–catenin compartment is physically segregated by ~ 30 nm from the uppermost compartment containing actin and actin-regulatory proteins, bridged by an interface compartment containing vinculin. We showed that the nanoscale positioning of vinculin is determined by α -catenin. Following conformational activation, vinculin extends ~ 30 nm to bridge the cadherin–catenin and actin compartments, while also modulating the nanoscale positions of the actin polymerization regulators zyxin and VASP. The extended conformation of vinculin requires both tension and tyrosine phosphorylation at residue Tyr822 by Abl kinase, while we also identified PTP1B as the tyrosine phosphatase that dephosphorylates vinculin. The observed multi-layer nanoscale architecture of cadherin-based adhesions appears to centrally position vinculin to act as an integrator of mechanical and biochemical signals, suggesting how the cadherin-based adhesions could selectively engage the actin cytoskeleton in response to regulatory input signals, effectively as a ‘molecular clutch’, to mediate intercellular interactions.

RESULTS

Mapping protein position in planar cadherin-based adhesions by super-resolution microscopy

The multi-micrometre vertical (z) depth of the adherens junctions in epithelial monolayers limited our ability to map molecular-scale organization by astigmatism-based super-resolution microscopy¹⁴

(Supplementary Fig. 1a). We noted that the planar cadherin-coated substrate format has been employed in earlier studies^{17,23–25} to obtain key molecular insights into interactions between cadherin and associated proteins. On this platform cells formed cadherin-based adhesions that recruited cadhesome proteins but not integrin-associated proteins (Supplementary Fig. 1b,c), suggesting that salient protein–protein interactions are probably recapitulated. To demarcate the plasma membrane position in this format, we first applied 3D interferometric photoactivated localization microscopy¹⁹ (Supplementary Fig. 2a,b) to image MDCK (Madin–Darby canine kidney) epithelial cells cultured on E-cadherin-coated substrate, using DiD membrane-targeting fluorophores²⁶. This clearly resolved dorsal and ventral plasma membranes, with the z -position of the latter at ~ 30 – 40 nm above the substrate (Fig. 1a–c). We then imaged filamentous (F)-actin using Alexa Fluor 647 phalloidin, observing that F-actin bundles reside at a higher z -position, centring around ~ 70 – 80 nm, (Fig. 1d,e). The spatial separation of ~ 30 nm between the ventral plasma membrane and the actin cytoskeleton thereby minimizes direct cadherin–actin interaction. The F-actin angle of approach is nearly parallel to the adhesion plane (Supplementary Fig. 3a–d), geometrically comparable to the F-actin orientation around adherens junctions⁴. Altogether, these data are suggestive of the nanoscale similarity between planar cadherin adhesions and native cell–cell contacts.

Nanoscale compartmentalization of E-cadherin-based adhesions

We next applied a surface-generated structured illumination technique^{20,21} (Supplementary Fig. 2c–g) to characterize nanoscale organization of FP-conjugated cadhesome proteins (Supplementary Fig. 4a).

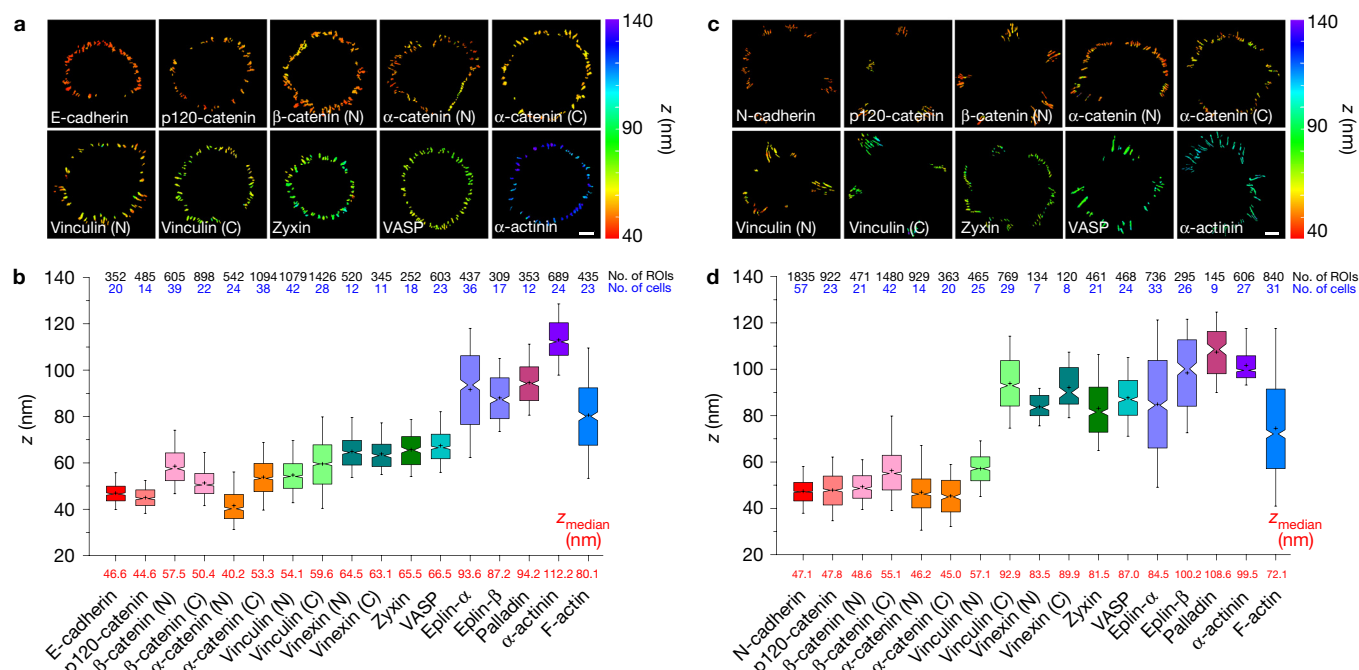


Figure 2 Protein stratifications in MDCK and C2C12 cadherin-based adhesions. **(a,b)** Topographic maps of protein z -positions (nanometres) **(a)** and notched box plots for the z -position of the indicated proteins **(b)** in E-cadherin-based adhesions of MDCK cells. **(c,d)** Topographic maps of protein z -positions (nanometres) **(c)** and notched box plots for the z -position of the indicated proteins **(d)** in N-cadherin-based adhesions of C2C12 cells. The colour bars in **a,c** indicate the z -position relative to the

substrate surface. Scale bars, $10\mu\text{m}$. Notched box plots in **b,d** indicate first and third quartiles, median and confidence intervals; whiskers, 5th and 95th percentiles. Median z_{centre} values are indicated below each box plot (red). n values are shown above each box plot and indicate the numbers of adhesions (number of ROIs, black). Numbers of cells are indicated in blue. Statistics are described in Supplementary Tables 1 and 2.

The fluorophore z -position relative to the substrate surface ($z = 0\text{ nm}$) was analysed pixel-wise, with the median value, z_{centre} , for adhesion regions of interest (ROIs) used as the representative protein z -position²⁷, while the z -position histograms denote the spatial distribution of proteins (Fig. 3 and Supplementary Note 1.3 and Supplementary Fig. 2h,i). We observed that E-cadherin (cytoplasmic domain GFP fusion) is positioned at $z_{\text{centre}} = 46.6\text{ nm}$, consistent with the dimensions of cadherin and other substrate components (Figs 2b and 3a).

Subsequently, we surveyed the nanoscale organization of key cadhesome proteins, observing a surprising degree of compartmentalization along the z -dimension that effectively spans between the plasma membrane and the actin cytoskeleton. Proteins observed in close proximity to cadherin include p120-catenin (44.6 nm), β -catenin (57.5 nm, amino terminus; 50.4 nm, carboxy terminus), and α -catenin (40.2 nm, N terminus). Their z -positions are consistent with their close association with the E-cadherin cytodomain⁶, thus defining the cadherin–catenin compartment. In contrast, actin-binding proteins were observed at significantly elevated z -positions, largely coinciding with the actin cytoskeleton. Eplins were found at 93.6 nm (α -isoform) and 87.2 nm (β -isoform), palladin at 94.2 nm, and α -actinin at 112.2 nm. A number of proteins were observed at intermediate z -positions, including vinculin (54.1 nm, N terminus), zyxin (65.5 nm), VASP (vasodilator-stimulated protein; 66.5 nm), and vinexin (64.5 nm, N terminus; 63.1 nm, C terminus) (Figs 2a,b and 3a, and Supplementary Fig. 5 and Supplementary Tables 1 and 2). Our measurements suggest that these centrally positioned proteins probably play an important role

as an interface compartment that mediates structural connection and mechanical coupling between the cadherin–catenin and the actomyosin compartments.

The conformation and nanoscale organization of α -catenin

Since α -catenin and vinculin have been implicated as mechanotransducers^{28–31}, we next investigated their configurations and spatial organization within the cadherin adhesions. Using a monoclonal antibody ($\alpha 18$) against the activated conformation of α -catenin³², we observed prominent staining (Fig. 4b and Supplementary Fig. 4d,e) consistent with measurements by a fluorescence resonance energy transfer (FRET) conformation probe⁹ (Fig. 4c and Supplementary Fig. 6d). Furthermore, the high precision of our technique enables inference of protein orientation and/or conformation via the use of the N- and C-terminal FP fusion constructs (Supplementary Note 2 and Supplementary Fig. 5e–h). We thus determined the C-terminal z -position of α -catenin, obtaining $z_{\text{centre}} = 53.3\text{ nm}$, compared with $z_{\text{centre}} = 40.2\text{ nm}$ for the N terminus, indicative of an oriented and activated configuration (Figs 3c–e and 4d and Supplementary Note 3). We next probed the z -position of the α -catenin vinculin-binding domain (VBD) by imaging the vinculin head domain (Vd1, residues 1–258) N-terminal-tagged with GFP, observing the z -position of 57.1 nm closely overlapping with the α -catenin C terminus, consistent with vinculin association to α -catenin (Fig. 4d). To further explore the role of α -catenin in vinculin positioning, we imaged vinculin-FP expressed in MDCK cells with stable α -catenin short hairpin RNA (shRNA) expression³³ (Supplementary Fig. 4b). We found that with α -catenin depleted, vinculin

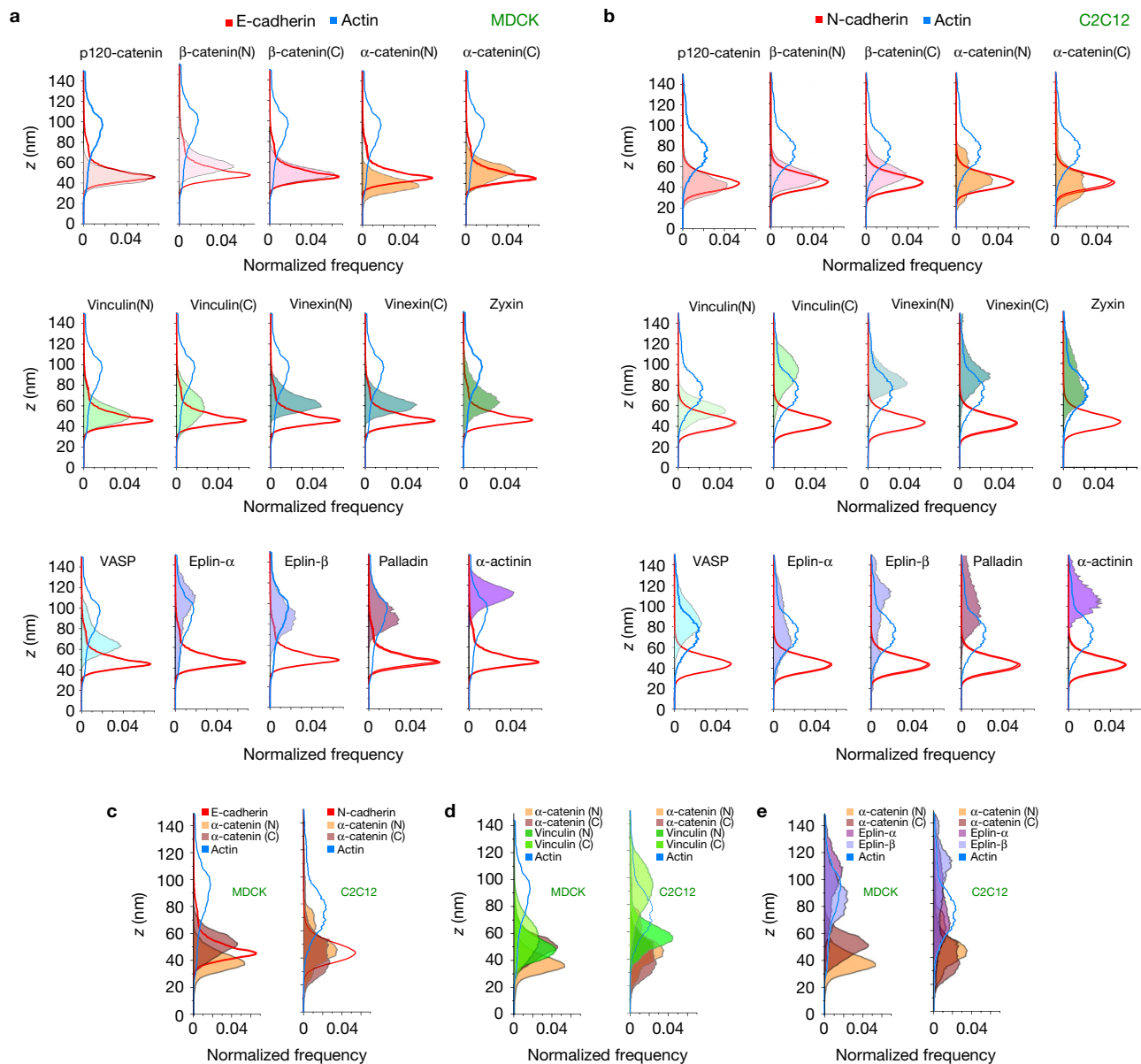


Figure 3 z-dimension profiles of cadhesome proteins. **(a,b)** A normalized histogram of the pixel z-position of the indicated proteins (filled colours) in MDCK **(a)** and C2C12 **(b)** cells, relative to E- or N-cadherin (solid red) and F-actin (solid blue). The integrated areas under each histogram are normalized to unity, such that each histogram reflects the probability

distribution of locating a given protein as a function of the z-position. **(c–e)** A comparison of the protein z-profiles of α -catenin (N- and C-terminal probes, shades of brown) **(c)** and vinculin (N- and C-terminal probes shades of green) **(d)**, or eplins (α and β isoforms, shades of purple) **(e)** between MDCK and C2C12 cells.

localizes to a higher z-position within the actomyosin compartment, probably via the association with actin³⁴ or actin-regulatory proteins such as VASP or α -actinin. On the other hand, following re-expression of α -catenin-FP, the intermediate z-positioning of vinculin is restored (Supplementary Fig. 6a and Supplementary Note 3).

Activated vinculin spans between the cadherin–catenin and actin cytoskeletal compartments

We next characterized how vinculin is organized within the cadherin adhesions. In MDCK, the wild-type (wt) vinculin C terminus was observed at $z_{\text{centre}} = 59.6$ nm, compared with 54.1 nm for the N terminus (Fig. 2b). Since vinculin conformation is able to switch

between the compact and the extended, uninhibited forms, the small N–C z-positional differences observed may correspond to either a relatively compact conformation, or an extended conformation that is oriented nearly parallel to the plasma membrane ($<10^\circ$). To differentiate these, we first probed vinculin configuration by FRET. Using a vinculin tension biosensor (vinculin-TS)²⁹ or a vinculin conformation biosensor³⁵, we observed comparatively high FRET efficiencies, indicative of low vinculin tension and a relatively compact conformation, respectively (Fig. 4f,g and Supplementary Fig. 6b,c,e–h). Additionally, the z-position of the mTFP1 fluorophore within vinculin-TS (Fig. 4a) was mapped to report the z-position of the vinculin linker region, obtaining z_{centre} of 67.6 nm, further

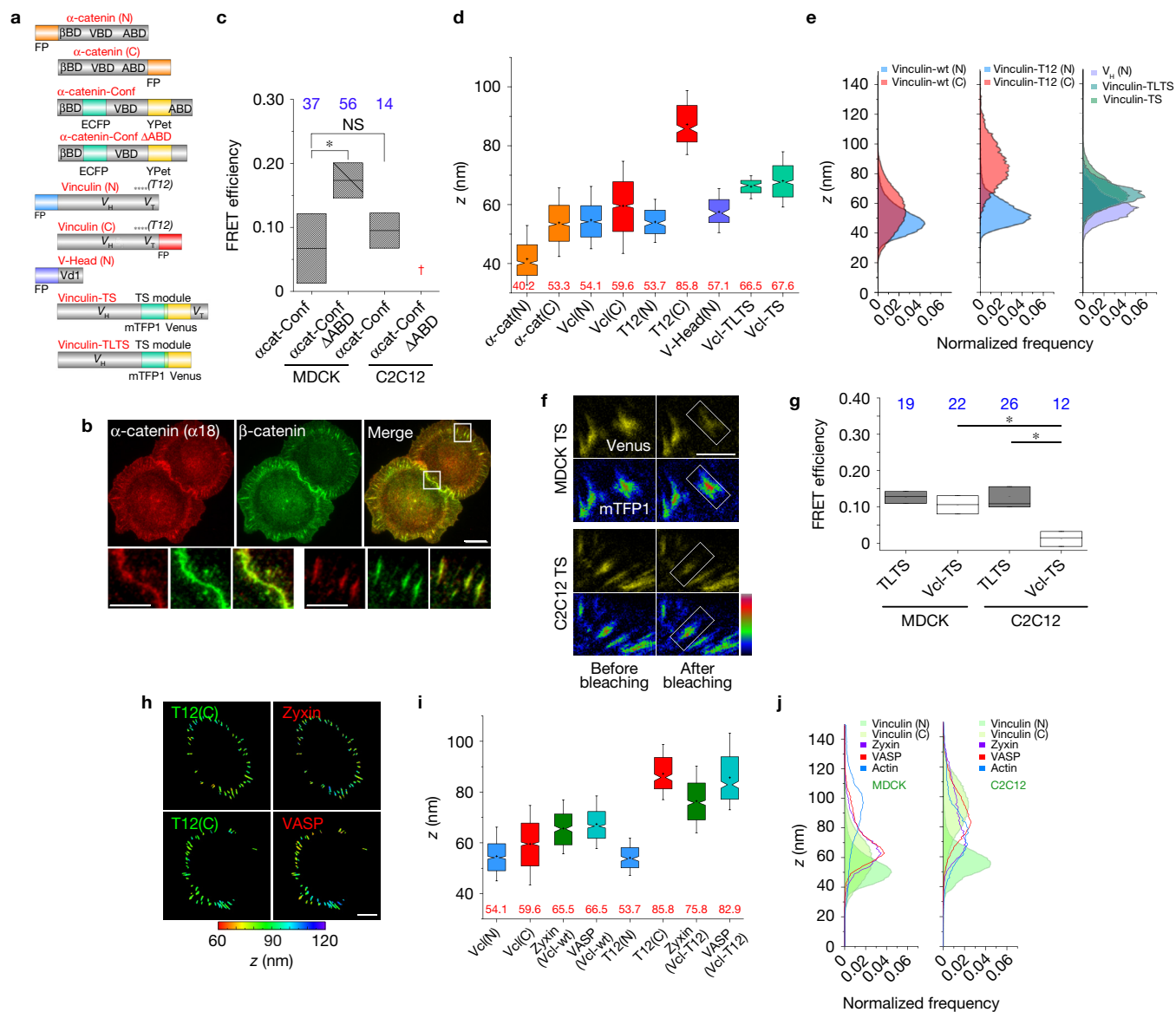


Figure 4 Nanoscale positions and conformations of vinculin and α -catenin in cadherin-based adhesions. **(a)** Diagrams of α -catenin and vinculin probes. FP, fluorescent protein (orange, α -catenin-FP probes; blue, vinculin N terminus; red, vinculin C terminus); α -catenin-conf, α -catenin conformation sensor (teal, ECFP; yellow, YPet); α -catenin-conf Δ ABD, α -catenin conformation sensor with actin-binding domain deletion; β BD, VBD and ABD, binding sites on α -catenin for β -catenin, vinculin and actin, respectively; V_H , V_T , and V_d1 , vinculin head-domain, vinculin tail-domain, and the d1 sub-domain of V_H , respectively; vinculin-TS (Vcl-TS), vinculin tension-sensor (teal, mTFP1; yellow, Venus); vinculin-TLTS, tailless vinculin-TS. ****Approximated positions of point mutations. **(b)** Immunofluorescence for activated α -catenin (α 18) (red) and β -catenin (green) in MDCK cells on E-cadherin substrate. Bottom row, insets zoom-in: native cell–cell contacts and planar cadherin adhesions. Scale bars, $10\mu\text{m}$ (insets, $5\mu\text{m}$). **(c)** FRET efficiency of α -cat-conf and α -cat-conf Δ ABD. †Construct did not localize in C212. **(d)** Box plots for z_{centre} of α -catenin and vinculin FP probes in MDCK. **(e)** Z-profiles of vinculin probes in MDCK. N-terminal (blue), C-terminal (red), vinculin-TS and vinculin-TL TS (shades of teal), and vinculin head

domain (V_H , residues 1–258, purple) probes. **(f)** FRET measurement of intra-vinculin tension. MDCK (top) and C2C12 (bottom) cells expressing vinculin-TS, on E- or N-cadherin substrate, respectively. Rainbow look-up table (colour bar) used for donor channel (mTFP1). Scale bar, $5\mu\text{m}$. **(g)** FRET efficiency in MDCK and C2C12. **(h)** Vinculin conformation modulates the position of zyxin and VASP. Topographic map of z-positions: vinculin-T12 C-terminal (left) and zyxin or VASP (right), co-expressed in MDCK cells. Colour bar: z-position relative to substrate surface. Scale bar, $10\mu\text{m}$. **(i)** Box plots for z_{centre} of vinculin, zyxin and VASP (green and teal), with wild-type vinculin (Vcl-wt) or vinculin-T12. **(j)** Comparison of protein z-profiles for vinculin (N- and C-terminal probes, shades of green), zyxin (purple) and VASP (red), overlaid with F-actin z-profile (blue), between MDCK and C2C12 cells. **(c,g)** Box plots for FRET efficiency (acceptor photobleaching): median, 1st and 3rd quartiles. * $P < 0.05$. NS, not significant. Number of cells (n values) in blue. **(d,i)** Notched box plots: 1st and 3rd quartiles, median and confidence intervals; whiskers, 5th and 95th percentiles, with n values (number of adhesions) in Supplementary Table 3.

supporting a compact conformation of vinculin, with the linker region arching upward (Fig. 4d,e and Supplementary Fig. 5e–h and Supplementary Note 2). In contrast, when we probed the orientation

of the constitutively active vinculin-T12 mutant³⁶, we observed a drastic upshift of the C-terminal z-position (85.8 nm) relative to the N terminus (53.7 nm) (Fig. 4d,e). Thus, activated vinculin effectively

spans ~ 30 nm or greater, a distance comparable to the fully extended length of vinculin³⁷. Taken together, these results illustrate how α -catenin emplaces vinculin in the interface zone, a central position that enables activated vinculin to robustly couple the cadherin–catenin with the actomyosin compartments (Supplementary Note 3.4). We also note that a more subtle interplay between α -catenin, β -catenin, and vinculin configuration may also be present (Supplementary Fig. 6a and Supplementary Notes 3.2 and 3.3). Our approach may thus be of further use in unravelling how the cadherin/ β -catenin/ α -catenin module is structurally and mechanically integrated with the cortical actin cytoskeleton^{15,23,28}, an important long-standing question, but which is beyond the scope of the current study.

Vinculin conformation modulates nanoscale position of zyxin and VASP

We next investigated how vinculin conformational states may regulate the spatial organization of other cadhesome components. We performed two-colour nanoscale z -mapping experiments by imaging FP fusion of vinculin partners such as zyxin or VASP, together with vinculin-T12. As shown in Fig. 4h–j, zyxin and VASP, in the presence of endogenous vinculin (wt), were observed at $z_{\text{centre}} = 65.5$ nm and $z_{\text{centre}} = 66.5$ nm, respectively. In contrast, following co-expression with vinculin-T12, we observed significant upshifts in their z -positions with $z_{\text{centre}} = 75.8$ nm for zyxin and $z_{\text{centre}} = 82.9$ nm for VASP. These results suggest that vinculin conformation may modulate the positioning of proteins such as zyxin and VASP that bind to its proline-rich linker region, which may in turn help promote actin polymerization in cadherin adhesions⁵ (Supplementary Note 3.4).

Vinculin conformational switch is regulated by Abl kinase and PTP1B phosphatase

To probe how vinculin conformational transition is regulated, we mapped the C-terminal z -position of vinculin (wt) under various biochemical or pharmacological perturbations. We observed that vinculin remains in the compact state with the overexpression of contractility effectors such as myosin IIA, myosin IIB, activated Src, or constitutively active RhoA. Interestingly, the overexpression of constitutively active Rac1 or cdc42 led to even lower C-terminal z -positions of vinculin of ~ 46 nm, coinciding with the membrane-proximal cadherin–catenin layer (Fig. 5a and Supplementary Table 3). This probably results from the vinculin-tail (V_T) phospholipid interaction³¹, and will be investigated in a more thorough manner separately. Intriguingly, we found that the inhibition of tyrosine phosphatases by orthovanadate results in the upshift of the vinculin C terminus to $z_{\text{centre}} \sim 70$ nm, indicative of a more open conformation whereas the vinculin N terminus remains at $z_{\text{centre}} \sim 54$ nm (Fig. 5b). Since the phosphorylation of vinculin Tyr822 by Abl kinase has recently been shown to be specific to cell–cell contacts³⁸, we mapped vinculin C-terminal z -position following co-treatment of orthovanadate and Gleevec³⁹, a specific Abl kinase inhibitor, observing the reversion of vinculin to the compact conformation ($z_{\text{centre}} = 59.1$ nm, Fig. 5b). In contrast, the vinculin C terminus remains at an elevated z -position following co-treatment of orthovanadate and the Src kinase inhibitor PP2 ($z_{\text{centre}} = 67.8$ nm, Fig. 5b), thus arguing against the involvement of Src kinase. To assess the contribution of the vinculin residue

Tyr822, we expressed vinculin-FP constructs in MDCK cells with stable vinculin shRNA expression³⁴ (vinculin-KD cells, Fig. 5c). For vinculin-wt, we observed similar z -positions of the N and C termini ($z_{\text{centre}} = 56.9$ nm and 56.8 nm, respectively), indicative of a compact conformation as expected. With the non-phosphorylatable mutation Y822F, the C-terminal z -position remained low ($z_{\text{centre}} = 57.5$ nm). In contrast, the phosphomimetic mutation Y822E resulted in the open conformation ($z_{\text{centre}} = 67.8$ nm). Thus, Abl kinase phosphorylation of Tyr822 appears to promote vinculin conformational activation.

Our results also imply that in MDCK, vinculin Tyr822 may be maintained in the unphosphorylated state by an as-yet-unidentified tyrosine phosphatase. Previous studies have documented a few cadherin-associated tyrosine phosphatases such as SHP2 (ref. 40) and PTP1B⁴¹. We therefore assayed for their involvement in vinculin conformational regulation by mapping vinculin C-terminal z -positions in the presence of their specific inhibitors. We observed that vinculin remains compact following treatment with PTP1B inhibitor ($z_{\text{centre}} = 57.9$ nm), but opened up following treatment with RK682, a PTP1B inhibitor, ($z_{\text{centre}} = 68.8$ nm, Fig. 5d). Furthermore, co-treatment of RK682 and Gleevec led to the compact conformation of vinculin. These results therefore implicate the Abl kinase/PTP1B phosphatase switch in regulating vinculin conformational opening in MDCK E-cadherin-based adhesions.

Nanoscale compartmentalization of N-cadherin-based adhesions

We next examined whether the nanoscale stratification of proteins observed in E-cadherin adhesions is present in other classical cadherin adhesions. We mapped cadhesome components in C2C12 mouse myoblast cells, which form N-cadherin-based adhesions when cultured on oriented N-cadherin substrate¹⁷. Remarkably, we observed a comparable extent of nanoscale compartmentalization (Figs 2c,d and 3b and Supplementary Fig. 5c,d). Most prominently, in contrast to the E-cadherin adhesions of MDCK cells, the wild-type vinculin is in a highly extended configuration in C2C12 cells, with the N and C termini at z_{centre} of 57.1 nm and 92.9 nm, respectively. Furthermore, zyxin, VASP and vinexin were also observed at elevated z -positions of 81.5 nm, 87.0 nm and 83.5/89.9 nm (vinexin N/C termini), respectively, supporting the notion that their nanoscale positioning might be vinculin conformation dependent.

Vinculin conformational switch integrates tension and phosphorylation signals to modulate the mechanical properties of cell–cell junctions

The comparatively high tension in C2C12 vinculin as measured by FRET (Fig. 4f,g and Supplementary Fig. 6b,c,d–h,j), together with the extended conformation (Figs 2c,d and 3b), suggests that tension may also promote vinculin activation. Indeed, vinculin-T12 expressed in C2C12 adopts a similarly extended conformation with the C-terminal z -position of 102.0 nm, corroborating the activated state observed for wild-type vinculin (Fig. 5f). To test this further, we treated C2C12 cells with ROCK inhibitor (Y-27632) to reduce tension at the cadherin-based adhesions and imaged the vinculin C-terminal z -position, observing a significant downshift to 64.6 nm, suggestive of a more compact configuration. Interestingly, the treatment of C2C12 by Gleevec also results in a similar extent of z -downshift (69.2 nm).

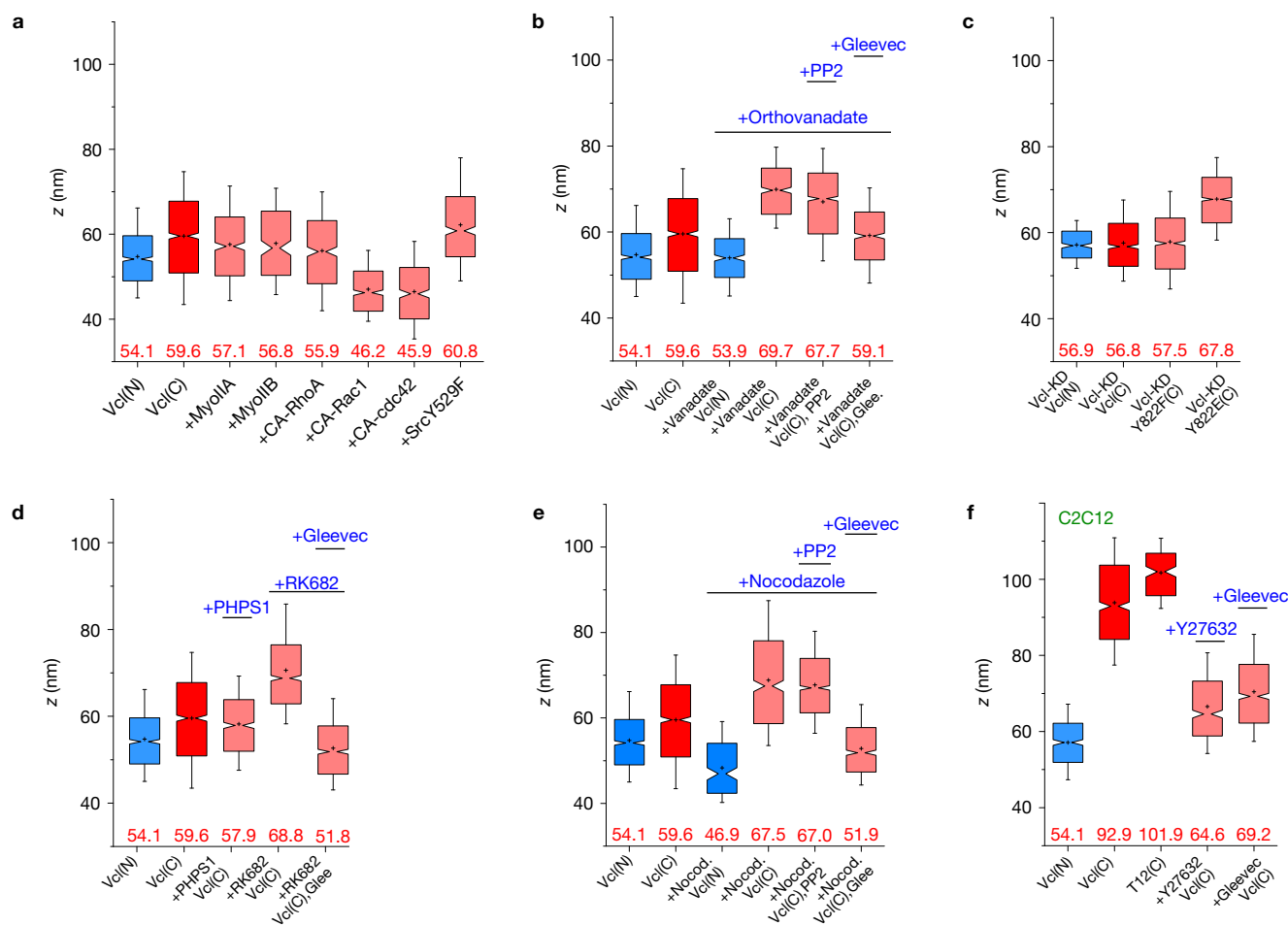


Figure 5 Vinculin conformation is modulated by tyrosine phosphorylation and tension. Notched box plots for vinculin z -positions. Blue and red indicate N- and C-terminal z -positions of WT vinculin, and coral indicates vinculin C-terminal z -position with perturbations. **(a)** Overexpression of myosin IIA and IIB, constitutively active (CA) RhoGTPases (RhoA, Rac1, cdc42) and Src kinase. **(b)** Treatment with orthovanadate, PP2 and Gleevec. **(c)** Vinculin Tyr822 phosphorylation mutants (Y822F, and Y822E) in MDCK vinculin-KD

cells. **(d)** Treatment with PHPS1, RK682 and Gleevec. **(e)** Vinculin in MDCK cells, treated with nocodazole and PP2 or Gleevec. **(f)** Vinculin in C2C12 cells, treated with Y-27632 or Gleevec. Notched boxes in **a–f** indicate 1st and 3rd quartiles, median and confidence intervals; whiskers, 5th and 95th percentiles. Red numbers in **a–f** are the median z_{centre} values. n values (number of adhesions) for each box plot, the number of cells, and statistical comparison are described in Supplementary Tables 3 and 4.

In light of these results, we treated MDCK cells with nocodazole, which upregulates contractility via microtubule depolymerization⁴², observing that the vinculin C-terminal z -position upshifted to $z_{\text{centre}} = 67.5$ nm, indicative of a conformational opening (Fig. 5e). Likewise, following co-treatment of nocodazole and Gleevec, vinculin reverted to the compact conformation ($z_{\text{centre}} = 51.9$ nm). Taken together, these results suggest that both tension and Tyr822 phosphorylation may be required for vinculin conformational activation.

We next sought to ascertain whether the native adherens junctions in epithelial monolayers are also regulated by the interplay of vinculin conformation, tension, and Tyr822 phosphorylation as delineated above. Using laser nanoscissor⁴³ to probe tension in cell–cell contacts, we measured the dynamics of recoil following junction scission in MDCK monolayers, observing that the treatment of cells with nocodazole to upregulate tension, or RK682 to inhibit Tyr822 dephosphorylation, resulted in higher initial recoil rates relative to control. Consistent with this, a similar effect is observed with greater recoil rates following the expression of vinculin-T12 or

Y822E, in comparison with the control, vinculin-KD, or Y822F (Fig. 6a–e and Supplementary Tables 6 and 7). Therefore, a similar mechanism probably governs vinculin conformational regulation in both planar cadherin adhesions and native adherens junctions of epithelial monolayers.

DISCUSSION

Our study elucidated how proteins in cadherin-based adhesions are organized to form multi-layered supramolecular complexes that couple cadherin to the actin cytoskeleton. We propose that this stratified architecture (Fig. 6g) may provide the structural framework for regulatory complexity in response to diverse mechanical and signalling cues under different tissue contexts, developmental processes, or disease states^{1–4,6}. For example, how vinculin appears to differentially engage the actin cytoskeleton can be conceptualized in terms of the molecular clutch, while how vinculin conformation is controlled by both mechanical (tension exerted via V_T domain) and biochemical cues (Tyr822 phosphorylation/dephosphorylation by Abl

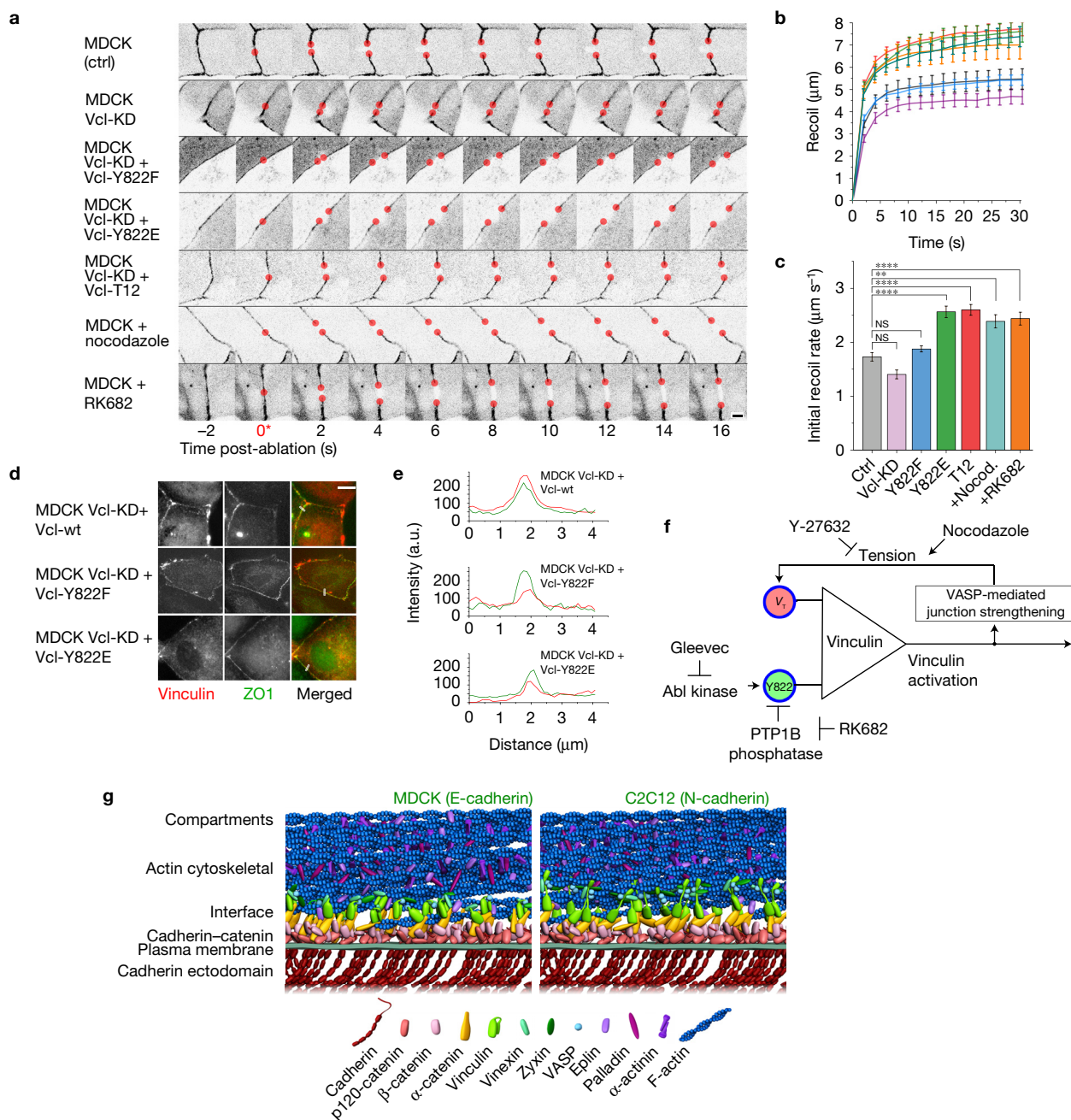


Figure 6 Integration of mechanical and biochemical signals by vinculin regulates mechanical properties of cell–cell contacts. **(a)** MDCK cells were cultured on fibronectin-coated substrate to form confluent monolayers, with cell–cell contacts labelled by ZO-1 fused with either mEmerald or mCherry. Cells were co-transfected with vinculin constructs or treated with pharmacological inhibitors as indicated. A montage of consecutive frames (interval: 2 s) is shown with junction excision at $t=0$ s. Recoiling edges of the junctions (red circles) were used to quantify the recoil trajectory. Untreated MDCK (ctrl) were compared with MDCK stably expressing shRNA against vinculin (MDCK Vcl-KD), MDCK Vcl-KD rescued with Y822F, Y88E, or T12 vinculin mutants, MDCK cells treated with nocodazole (to promote contractility, $10\ \mu\text{M}$ for 1 h), and RK682 (PTP1B inhibitor to inhibit Tyr822 dephosphorylation, $10\ \mu\text{g ml}^{-1}$ for 1 h). Scale bar, $5\ \mu\text{m}$. **(b,c)** Junction recoil **(b)** and initial recoil rate **(c)** following laser ablation of native cell–cell junctions in MDCK epithelial monolayers, with vinculin mutants, or pharmacological treatment. The colours of the plots in **b** correspond to the bar graphs in **c**. Ablation occurred at 0 s. Data in **b**

and **c** represent mean \pm error bars (s.e.m.). $n=19$ (ctrl); 18 (Vcl-KD); 16 (Vcl-KD + Y822F); 17 (Vcl-KD + Y822E); 18 (Vcl-KD + Vcl-T12); 11 (+Nocodazole); 24 (+RK682). $**P < 0.005$, $****P = 5 \times 10^{-5}$. Statistics in Supplementary Tables 6 and 7. **(d)** Fluorescence micrographs of MDCK vinculin KD epithelial monolayers rescued with vinculin wt, vinculin Y822F (non-phosphorylatable), vinculin Y822E (phosphomimetic) fusion constructs to demonstrate their localization at native adherens junctions. Cells were co-transfected with ZO-1 constructs. Scale bar, $10\ \mu\text{m}$. **(e)** Fluorescence intensity line profiles along the lines (white) in **d**, showing co-localization of vinculin (red) with ZO-1 (green) at the cell–cell junctions. **(f)** Diagram of vinculin conformational regulation by tension and Tyr822 phosphorylation, and a putative positive feedback loop. **(g)** Schematic models of protein organization in cadherin-based adhesions, with stratified compartments along the vertical axis at empirically determined z-positions, for MDCK E-cadherin-based adhesions (left, with compact vinculin) and C2C12 N-cadherin-based adhesions (right, with extended vinculin). Note that the model does not depict protein stoichiometry.

kinase/PTP1B phosphatase) (Fig. 6d) is evocative of a rudimentary AND logic gate. Subsequent to both inputs, vinculin activation upshifts the position of proteins such as VASP, probably promoting further actin polymerization and a further increase in vinculin tension⁵, thereby resulting in a positive feedback loop, which may help impart robustness, bi-stability, and tunability⁴⁴.

Interestingly, the nanoscale architecture of the cadherin-based cell adhesions is reminiscent of focal adhesions (FAs) characterized earlier¹⁸. Functionally, both these adhesion types serve to integrate the cortical actin cytoskeletal networks with membrane-anchored receptor complexes. As the integrins and cadherins are fundamentally dissimilar classes of receptors, we suggest that such differences necessitate a centrally positioned protein compartment to serve as a structural and mechanical interface, akin to a universal adaptor, so that the common actomyosin machinery can be coupled with different membrane-bound cell-adhesion apparatuses. Vinculin appears to be properly positioned for such a role, while also possessing an appropriate domain organization, with an actin-binding tail domain (V_T) flexibly linked to the head domain (V_H) that can alternately engage with α - or β -catenin^{45,46}, in cadherin adhesions, or talin, in FAs⁴⁷.

Nevertheless the molecular mechanisms governing vinculin spatial organization appear to diverge between the cadherin adhesions and FAs, despite the comparable stratified architecture. Unlike in FAs, where a large (relative molecular mass of 270,000) and highly elongated protein, talin, plays a dominant structural role comprising the FA core²⁷, directly tethering integrin to actin, in cadherin adhesions such a singularly dominant scaffold is not present. Instead, cadherin-actin linkage appears to be mediated by a plurality of multi-protein complexes. For example, in addition to the cadherin/ β -catenin/ α -catenin complex, α -catenin/Epln⁴⁸ and β -catenin/vinculin⁴⁶ have also been implicated. Furthermore, vinculin stoichiometry probably differs significantly between cadherin adhesions and FAs. In the former, the central placement of vinculin appears to be determined by a single binding site on α -catenin, while in the latter, at least 11 vinculin-binding sites⁴⁹ have been identified in talin. One may conjecture that this difference may reflect the contrasting mechanical context between cell-matrix and cell-cell adhesions. The rigidity of the extracellular matrix spans several orders of magnitude⁵⁰, and thus variable and cooperative interaction between multiple vinculin-binding sites on talin could play a role in fine-tuning FA mechanosensitivity over such a wide dynamic range. On the contrary, cell-cell junction forces are exerted between neighbouring cells, and thus much fewer vinculin-binding sites may be required to respond to the narrower dynamic range of rigidity.

Our data, together with recent studies on vinculin in FAs and cell-cell contacts^{34,38,45}, suggest that the conformational landscape of vinculin may be more complex than a simple two-state on-off model. For example, studies in FAs using FRET biosensors for either conformation or tension revealed that while conformationally open or high-tension vinculin (that is, low FRET efficiency) was highly enriched at adhesion sites, high FRET efficiency vinculin biosensors also localize there^{29,35}, suggesting that conformationally compact or low-tension vinculin is capable of adhesion localization. In cell-cell contacts, our data show that vinculin in a relatively compact, low-tension state is recruited to the MDCK E-cadherin adhesions via activated α -catenin. It is unclear yet how this pool of low-tension

and compact vinculin differs structurally from the autoinhibited cytoplasmic pool. We surmise that vinculin could be partially unfurled such that α -catenin binding is enabled. This allows vinculin to be emplaced in the interface compartment, poised to engage the actin cytoskeleton, while remaining in the unphosphorylated low-tension state due to the prevailing PTP1B activity. The relief of PTP1B enables Abl kinase phosphorylation of Tyr822 and an upward extension of the vinculin C terminus by actomyosin contraction, although the extent of conformational opening in MDCK appears to be lower than fully active, probably due to the low tension generated by this cell type as documented previously²⁸. In contrast, C2C12 vinculin may become fully activated due to both higher contractility and probably lower PTP1B activity (both PTP1B and Abl are expressed in these cell types, Supplementary Fig. 4c). At present, we do not know yet whether such differences reflect cell-type specificity or E-/N-cadherin specificity, and whether Tyr822 phosphorylation actuates vinculin conformational changes directly, or indirectly by recruiting vinculin binding partners to stabilize the open conformation. It is also unclear whether a similar phosphorylation-dependent conformational modulation is operational in FAs, since the Tyr822 phosphorylation is reportedly cell-cell contact specific³⁸. For FAs, the presence of a large number of vinculin-binding sites, such as on talin and paxillin^{31,47}, would probably require the generation of proper molecular tools for a similar conformational analysis to be tractable.

Finally, we note that while the planar cadherin substrate has greatly facilitated nanoscale optical imaging, the adhesions thus formed probably differ from native cell-cell contacts in important aspects such as cadherin mobility, rigidity, and junctional topology, and thus not all aspects of *in vivo* cell-cell junction mechanics may be captured. As such, alternative explanations for the extended conformation of vinculin thus observed may include recruitment of as-yet-unexplored proteins, modulation of affinity to binding partners, indirect effects on cellular contractility, or other changes in protein stability that affect functions. Nevertheless, we suggest that the use of physically well-defined substrate can be highly valuable in revealing molecular-scale behaviours, particularly since native cell-cell contacts often undergo concerted and complicated changes in their mechanical, compositional, and morphological properties following perturbations, which can greatly obfuscate molecular mechanistic dissection. Given the resolution limitation of current super-resolution microscopy methods, an alternative approach to further probe native cell-cell contacts could be via correlative electron microscopy-super-resolution microscopy techniques⁵¹. □

METHODS

Methods, including statements of data availability and any associated accession codes and references, are available in the [online version of this paper](#).

Note: Supplementary Information is available in the online version of the paper

ACKNOWLEDGEMENTS

We thank C. Ajo-Franklin (Lawrence Berkeley National Laboratory), G. Shtengel and H. Hess (Howard Hughes Medical Institute, Janelia Research Campus) for generous help with super-resolution microscopy instrumentation and analysis. We thank H. Chen (Protein Expression Facility, Mechanobiology Institute, Singapore) for generation of mutant constructs, H. T. Ong and A. Sathe (Mechanobiology Institute) for assistance with FRET analysis, C. Zhang (Mechanobiology Institute) for assistance with 3D graphical model, and J. Yan (National University of Singapore)

for critical reading of the manuscript. P.K., C.B., Y.Wang, A.R., T.S. and R.Z.-B. are supported by Singapore National Research Foundation Fellowship awarded to P.K. (NRF-NRFF-2011-04), R.Z.-B. (NRF-RF2009-RF001-074), and Competitive Research Programme (NRF2012NRF-CRP001-084) to P.K. and R.Z.-B. Y.T. is supported by Mechanobiology Institute and National University of Singapore Startup Grants, and a Singapore Ministry of Education Tier 2 grant (MOE2015-T2-1-116). B.L. is supported by the European Research Council under the European Union's Seventh Framework Programme (FP7/2007–2013/ERC grant agreement no. 617233), the Mechanobiology Institute, and the Institut Universitaire de France, and USPC-NUS funding. B.L. and R.-M.M. are also supported by CNRS, the Human Frontier Science Program (grant RGP0040/2012) and Agence Nationale de la Recherche (ANR 2010 Blan1515).

AUTHOR CONTRIBUTIONS

C.B. and Y.Wang performed the super-resolution imaging experiments and conducted data analysis. C.B. and A.R. performed and analysed FRET experiments. C.B., A.R., Y.H. and Y.T. designed and C.B. performed and analysed laser ablation experiments. Y.Wu and R.Z.-B. performed imaging of Eph4 cell–cell junctions by astigmatism-based 3D super-resolution microscopy. C.B., T.S., M.B., M.W.D., B.L. and R.-M.M. designed and generated fusion constructs, and provided new reagents and analytical tools. C.B. and P.K. designed the study and wrote the manuscript. All authors discussed the results and commented on the manuscript.

COMPETING FINANCIAL INTERESTS

The authors declare no competing financial interests.

Published online at <http://dx.doi.org/10.1038/ncb3456>

Reprints and permissions information is available online at www.nature.com/reprints

- Heisenberg, C.-P. & Bellaïche, Y. Forces in tissue morphogenesis and patterning. *Cell* **153**, 948–962 (2013).
- Guillot, C. & Lecuit, T. Mechanics of epithelial tissue homeostasis and morphogenesis. *Science* **340**, 1185–1189 (2013).
- Lecuit, T. & Yap, A. S. E-cadherin junctions as active mechanical integrators in tissue dynamics. *Nat. Cell Biol.* **17**, 533–539 (2015).
- Takeichi, M. Dynamic contacts: rearranging adherens junctions to drive epithelial remodelling. *Nat. Rev. Mol. Cell Biol.* **15**, 397–410 (2014).
- Leerberg, J. M. *et al.* Tension-sensitive actin assembly supports contractility at the epithelial zonula adherens. *Curr. Biol.* **24**, 1689–1699 (2014).
- Leckband, D. & de Rooij, J. Cadherin adhesion and mechanotransduction. *Annu. Rev. Cell Dev. Biol.* **30**, 291–315 (2014).
- Niessen, C. M., Leckband, D. & Yap, A. S. Tissue organization by cadherin adhesion molecules: dynamic molecular and cellular mechanisms of morphogenetic regulation. *Physiol. Rev.* **91**, 691–731 (2011).
- Borghini, N. *et al.* E-cadherin is under constitutive actomyosin-generated tension that is increased at cell–cell contacts upon externally applied stretch. *Proc. Natl Acad. Sci. USA* **109**, 12568–12573 (2012).
- Kim, T. J. *et al.* Dynamic visualization of α -catenin reveals rapid, reversible conformation switching between tension states. *Curr. Biol.* **25**, 218–224 (2015).
- Bertocchi, C., Vaman Rao, M. & Zaidel-Bar, R. Regulation of adherens junction dynamics by phosphorylation switches. *J. Signal Transduct.* **2012**, 125295 (2012).
- Zaidel-Bar, R. Cadherin adhesomes at a glance. *J. Cell Sci.* **126**, 373–378 (2013).
- Huang, B., Wang, W., Bates, M. & Zhuang, X. Three-dimensional super-resolution imaging by stochastic optical reconstruction microscopy. *Science* **319**, 810–813 (2008).
- Truong Quang, B. A., Mani, M., Markova, O., Lecuit, T. & Lenne, P. F. Principles of E-cadherin supramolecular organization *in vivo*. *Curr. Biol.* **23**, 2197–2207 (2013).
- Wu, Y., Kanchanawong, P. & Zaidel-Bar, R. Actin-delimited adhesion-independent clustering of e-cadherin forms the nanoscale building blocks of adherens junctions. *Dev. Cell* **32**, 139–154 (2015).
- Buckley, C. D. *et al.* Cell adhesion. The minimal cadherin-catenin complex binds to actin filaments under force. *Science* **346**, 1254211 (2014).
- Yonemura, S., Itoh, M., Nagafuchi, A. & Tsukita, S. Cell-to-cell adherens junction formation and actin filament organization: similarities and differences between non-polarized fibroblasts and polarized epithelial cells. *J. Cell Sci.* **108**, 127–142 (1995).
- Gavard, J. *et al.* Lamellipodium extension and cadherin adhesion: two cell responses to cadherin activation relying on distinct signalling pathways. *J. Cell Sci.* **117**, 257–270 (2004).
- Kanchanawong, P. *et al.* Nanoscale architecture of integrin-based cell adhesions. *Nature* **468**, 580–584 (2010).
- Shtengel, G. *et al.* Interferometric fluorescent super-resolution microscopy resolves 3D cellular ultrastructure. *Proc. Natl Acad. Sci. USA* **106**, 3125–3130 (2009).
- Ajo-Franklin, C. M., Ganesan, P. V. & Boxer, S. G. Variable incidence angle fluorescence interference contrast microscopy for z-imaging single objects. *Biophys. J.* **89**, 2759–2769 (2005).
- Paszek, M. J. *et al.* Scanning angle interference microscopy reveals cell dynamics at the nanoscale. *Nat. Methods* **9**, 825–827 (2012).
- Bertocchi, C., Goh, W. I., Zhang, Z. & Kanchanawong, P. Nanoscale imaging by superresolution fluorescence microscopy and its emerging applications in biomedical research. *Crit. Rev. Biomed. Eng.* **41**, 281–308 (2013).
- Yamada, S., Pokutta, S., Drees, F., Weis, W. I. & Nelson, W. J. Deconstructing the cadherin-catenin-actin complex. *Cell* **123**, 889–901 (2005).
- Kovacs, E. M., Goodwin, M., Ali, R. G., Paterson, A. D. & Yap, A. S. Cadherin-directed actin assembly: E-cadherin physically associates with the Arp2/3 complex to direct actin assembly in nascent adhesive contacts. *Curr. Biol.* **12**, 379–382 (2002).
- Strale, P.-O. *et al.* The formation of ordered nanoclusters controls cadherin anchoring to actin and cell–cell contact fluidity. *J. Cell Biol.* **210**, 333–346 (2015).
- Shim, S. H. *et al.* Super-resolution fluorescence imaging of organelles in live cells with photoswitchable membrane probes. *Proc. Natl Acad. Sci. USA* **109**, 13978–13983 (2012).
- Liu, J. *et al.* Talin determines the nanoscale architecture of focal adhesions. *Proc. Natl Acad. Sci. USA* **112**, E4864–E4873 (2015).
- Yonemura, S., Wada, Y., Watanabe, T., Nagafuchi, A. & Shibata, M. α -Catenin as a tension transducer that induces adherens junction development. *Nat. Cell Biol.* **12**, 533–542 (2010).
- Grashoff, C. *et al.* Measuring mechanical tension across vinculin reveals regulation of focal adhesion dynamics. *Nature* **466**, 263–266 (2010).
- Yao, M. *et al.* Force-dependent conformational switch of α -catenin controls vinculin binding. *Nat. Commun.* **5**, 4525 (2014).
- Peng, X., Nelson, E. S., Maiers, J. L. & DeMali, K. A. New insights into vinculin function and regulation. *Int. Rev. Cell Mol. Biol.* **287**, 191–231 (2011).
- Nagafuchi, A. & Tsukita, S. The loss of the expression of α catenin, the 102 kD cadherin associated protein, in central nervous tissues during development. *Dev. Growth Differ.* **36**, 59–71 (1994).
- Benjamin, J. M. *et al.* α E-catenin regulates actin dynamics independently of cadherin-mediated cell–cell adhesion. *J. Cell Biol.* **189**, 339–352 (2010).
- Sumida, G. M., Tomita, T. M., Shih, W. & Yamada, S. Myosin II activity dependent and independent vinculin recruitment to the sites of E-cadherin-mediated cell–cell adhesion. *BMC Cell Biol.* **12**, 48 (2011).
- Chen, H., Cohen, D. M., Choudhury, D. M., Kioka, N. & Craig, S. W. Spatial distribution and functional significance of activated vinculin in living cells. *J. Cell Biol.* **169**, 459–470 (2005).
- Cohen, D. M., Chen, H., Johnson, R. P., Choudhury, B. & Craig, S. W. Two distinct head-tail interfaces cooperate to suppress activation of vinculin by talin. *J. Biol. Chem.* **280**, 17109–17117 (2005).
- Milam, L. M. Electron microscopy of rotary shadowed vinculin and vinculin complexes. *J. Mol. Biol.* **184**, 543–545 (1985).
- Bays, J. L. *et al.* Vinculin phosphorylation differentially regulates mechanotransduction at cell–cell and cell–matrix adhesions. *J. Cell Biol.* **205**, 251–263 (2014).
- Nagar, B. *et al.* Crystal structures of the kinase domain of c-Abl in complex with the small molecule inhibitors PD173955 and imatinib (STI-571). *Cancer Res.* **62**, 4236–4243 (2002).
- Ukropec, J. A., Hollinger, M. K., Salva, S. M. & Woolkalis, M. J. SHP2 association with VE-cadherin complexes in human endothelial cells is regulated by thrombin. *J. Biol. Chem.* **275**, 5983–5986 (2000).
- Xu, G., Arregui, C., Lilien, J. & Balsamo, J. PTP1B modulates the association of β -catenin with N-cadherin through binding to an adjacent and partially overlapping target site. *J. Biol. Chem.* **277**, 49989–49997 (2002).
- Chang, Y.-C., Nalbant, P., Birkenfeld, J., Chang, Z.-F. & Bokoch, G. M. GEF-H1 couples nocodazole-induced microtubule disassembly to cell contractility via RhoA. *Mol. Biol. Cell* **19**, 2147–2153 (2008).
- Hara, Y., Shagirov, M. & Toyama, Y. Cell boundary elongation by non-autonomous contractility in cell oscillation. *Curr. Biol.* **26**, 2388–2396 (2016).
- Tsai, T. Y. *et al.* Robust, tunable biological oscillations from interlinked positive and negative feedback loops. *Science* **321**, 126–129 (2008).
- Peng, X., Maiers, J. L., Choudhury, D., Craig, S. W. & DeMali, K. A. α -Catenin uses a novel mechanism to activate vinculin. *J. Biol. Chem.* **287**, 7728–7737 (2012).
- Peng, X., Cuff, L. E., Lawton, C. D. & DeMali, K. A. Vinculin regulates cell-surface E-cadherin expression by binding to β -catenin. *J. Cell Sci.* **123**, 567–577 (2010).
- Critchley, D. R. Biochemical and structural properties of the integrin-associated cytoskeletal protein talin. *Annu. Rev. Biophys.* **38**, 235–254 (2009).
- Abe, K. & Takeichi, M. EPLIN mediates linkage of the cadherin catenin complex to F-actin and stabilizes the circumferential actin belt. *Proc. Natl Acad. Sci. USA* **105**, 13–19 (2008).
- Gingras, A. R. *et al.* Mapping and consensus sequence identification for multiple vinculin binding sites within the talin rod. *J. Biol. Chem.* **280**, 37217–37224 (2005).
- Engler, A. J., Sen, S., Sweeney, H. L. & Discher, D. E. Matrix elasticity directs stem cell lineage specification. *Cell* **126**, 677–689 (2006).
- Shtengel, G. *et al.* Imaging cellular ultrastructure by PALM, iPALM, and correlative iPALM-EM. *Methods Cell Biol.* **123**, 273–294 (2014).

METHODS

Surface modification of imaging substrates by oriented cadherin extracellular domains. Coverglasses (no. 1.5, 18 mm diameter) with pre-embedded plasmonic nanoparticles (Hestzig, LLC) were UV-sterilized for 15 min in a sterile laminar flow hood and rinsed with DPBS. Silicon oxide wafers, p-type (100)-orientation with ~500 nm thermal oxide (Bondatek; Addison Engineering), were pre-treated as described previously²¹, cut into ~1.2 cm × 1.2 cm chips with a diamond-tip pen, pre-rinsed with distilled water, sonicated for 20 min in 100% acetone, rinsed with distilled water, sonicated in 1 M potassium hydroxide, and post-rinsed with distilled water. Both the coverglasses and the silicon wafers were silanized for protein conjugation by incubation with 3-glycidyloxy-propyl-dimethoxymethylsilane (Sigma) (0.045% in 100% ethanol) for 1 h on a shaker at room temperature, and then cured at 110 °C for 1 h. Silanized substrates were rinsed with 70% ethanol and distilled water, and then air-dried. Subsequently, following a previously published protocol¹⁷, the substrates were incubated with goat anti-human or goat anti-mouse F_c fragment specific antibody for E-cadherin and N-cadherin substrate, respectively (Jackson ImmunoResearch, West Grove), at 1 μg cm⁻² in 0.1 M pH 8 borate buffer, and incubated at 4 °C overnight in a humidity chamber. The substrates were then rinsed with PBS and neutralized by NaHCO₃ (100 mM, pH 8.3) and aminoethoxy-ethanol (Sigma) for 1 h. After rinsing with PBS, the substrates were incubated for 2 h with human E-cadherin-F_c or mouse N-cadherin-F_c (R&D system) at 1 μg cm⁻², rinsed with PBS (with Ca²⁺ and Mg²⁺), and blocked with 0.2 % pluronic acid (Sigma) in PBS for 20 min at room temperature.

Cell culture and sample preparation. MDCK (Madin–Darby canine kidney) cells were cultured in DMEM media supplemented with 10% fetal bovine serum (FBS), and 100 units ml⁻¹ of penicillin/streptomycin (Life Technologies). The MDCK cell line with stable α-catenin shRNA expression³³ was a gift from W. J. Nelson (Stanford University, USA). The MDCK cell line with stable vinculin shRNA expression was a gift from S. Yamada (University of California, Davis)³⁴. The Eph4 mouse mammary epithelial cell line was a gift from J.-P. Thiery (IMCB, A-STAR, Singapore). Eph4 cells were cultured in DMEM with 10% FBS and 1% penicillin–streptomycin (complete DMEM). C2C12 (murine myoblast) cells were cultured in DMEM media supplemented with 20% FBS, to maintain the undifferentiated state, and 100 units ml⁻¹ of penicillin/streptomycin. Cells were transfected by electroporation with ~10 μg of endotoxin-free plasmid DNA per ~1 × 10⁶ cells using the Neon transfection system (Life Technologies) according to the manufacturer's protocol, except where indicated otherwise. No cell lines used in this study were found in the database of commonly misidentified cell lines that is maintained by ICLAC and NCBI Biosample. The cell lines were not authenticated. The cell lines used were regularly tested for mycoplasma contamination by PCR methods.

For astigmatism-based 3D super-resolution microscopy (Supplementary Fig. 1a) and wide-field fluorescence microscopy (Supplementary Fig. 4a) of epithelial monolayers, MDCK or Eph4 cells were cultured until confluent on sterile fibronectin-coated no. 1.5 fiducial coverslips (Hestzig LLC). Cells were fixed for 15 min with 4% paraformaldehyde (Electron Microscopy Sciences), rinsed, and blocked by 10% FBS in DPBS. The samples were then permeabilized by 0.2% Triton X-100 in DPBS for 2 min, followed by 1 h incubation at room temperature with the primary antibodies and followed with the secondary antibodies. Primary antibodies used were mouse anti-E-cadherin cytodomain (BD Biosciences) at a dilution of 1:200; mouse anti-β-catenin (Sigma-Aldrich), 1:400; mouse anti-vinculin (Sigma-Aldrich), 1:200; rabbit anti-α-catenin (Abcam), 1:400; and rabbit anti-myosin IIA (Sigma-Aldrich), 1:400. Afterwards, cells were post-fixed for 5 min in 3% PFA with 0.05% glutaraldehyde. Secondary antibodies used were donkey anti-mouse, and goat anti-rabbit, conjugated with Alexa Fluor 488, Alexa Fluor 568, or Alexa Fluor 647 (Life Technologies) at a dilution of 1:400.

For MDCK and C2C12 on planarized cadherin substrates, transfected cells were trypsinized and replated onto the silicon wafers or coverglasses, pre-coated with IgG and cadherin-F_c as described above, and incubated at 37 °C in 5% CO₂. Cells were replated using serum-free medium, since fetal bovine serum contains fibronectin, which may induce integrin-based focal adhesion formation. For the measurements of cell–cell junction recoil following laser ablation, MDCK cells were cultured on fibronectin-coated coverglass prepared by incubating 10 μg ml⁻¹ of bovine fibronectin (F1141, Sigma) in PBS for 1 h at 37 °C in a humidified atmosphere. Cells were transfected with the expression vectors for ZO-1 fused with either mEmerald or mApple as a marker for cell–cell junctions, in conjunction with vinculin constructs as appropriate.

For actin imaging, cytoskeleton buffer (CB: 10 mM MES, pH 6.1, 150 mM NaCl, 5 mM EGTA, 5 mM glucose and 5 mM MgCl₂) was used. Cells were briefly first washed with warm (37 °C) calcium-containing PBS, and pre-fixed by 0.2% glutaraldehyde and 0.1% Triton X-100 in CB for 2 min, followed by 2% glutaraldehyde in CB for 10 min. Afterwards, glutaraldehyde autofluorescence was quenched by incubation for 7 min in freshly prepared 0.1% NaBH₄ in PBS, followed

by three rinses in PBS for 10 min each. Samples were then incubated with 0.33 μM of Alexa Fluor 647 phalloidin (Life Technologies) for either 30 min at room temperature or overnight at 4 °C.

For pharmacological inhibition, cells were treated at the following concentration prior to fixation or laser ablation experiment: sodium orthovanadate (S6508, Sigma), 100 μM; PP2 (P0042, Sigma), 20 μM; Gleevec (imatinib, SML1027, Sigma), 20 μM; PPHS1 (P0039, Sigma), 15 μM; RK682 (RK2033, Sigma), 10 μg ml⁻¹; nocodazole (M1404, Sigma), 10 μM; Y-27632 (Y0503, Sigma), 10 μM. Cells were fixed for imaging ~4–6 h after replating, using 4% paraformaldehyde and stored in PHEM buffer (PIPES 60 mM, HEPES 25 mM, MgCl₂ 2 mM, without EGTA, pH 7.0). Rat monoclonal antibody against activated α-catenin (α18—dilution 1:50) was provided by A. Nagafuchi (Nara Medical University, Japan)³², rabbit anti-β-catenin (ab2365, Abcam) was used at a dilution 1:100 and mouse anti-vinculin (V9131, Sigma) at 1:100. For plasma membrane imaging, live cells were incubated for 1 h at 37 °C with DiD membrane-targeting fluorophore (Life Technologies) at 10 μM in phenol-red free cell culture medium, fixed for 10 min in 4% paraformaldehyde, and quenched with 50 mM NaBH₄ for 12 min.

Three-dimensional super-resolution microscopy by astigmatism-based single-molecule localization. The three-dimensional super-resolution micrographs of adherens junctions shown in Supplementary Fig. 1 were obtained using fixed Eph4 cells mounted in a PBS-based imaging buffer containing oxygen scavenger, made fresh before imaging: 45 mM Tris-HCl, 9.4 mM NaCl, 9% glucose, 100 mM mercaptoethylamine, 0.56 mg ml⁻¹ glucose oxidase, and 0.034 mg ml⁻¹ catalase. The imaging samples were assembled by placing a clean coverslip on top of the cell-containing coverslip. Excess imaging buffer was removed and the samples sealed by nail polish. In cases where cells were cultured on non-fiducial coverslips, 80–100 nm gold nanoparticles (790122-010, Corpuscular Inc.) were added prior to imaging to serve as fiducial markers for drift correction.

Raw single-molecule fluorescence images of Alexa Fluor 647 blinking were acquired on a Nikon N-STORM microscope, operated by NIS-Elements AR software and equipped with a piezo z stage (Mad City Labs), an Ixon3 EMCCD camera (Andor, Belfast), a cylindrical lens insert, and a motorized TIRF illuminator. Lasers used were fibre-coupled into the illuminator from 640 nm 100 mW and 405 nm 50 mW laser heads. The objective lens used was a Nikon 100× Apo TIRF NA 1.49. Thirty thousand frames were acquired at 30 frames per second for each data set. Since the adherens junctions in Eph4 are typically >2 μm into the sample, fluorophores in the basal region of cells were first illuminated for 5 min with the imaging laser using a low incidence angle for pre-depletion. Subsequently, the adherens junctions were imaged using a highly oblique incidence angle slightly smaller than the critical angle.

Image processing and super-resolution reconstruction were carried out by custom-developed software written in IDL described previously¹⁹. Briefly, each single-molecule peak is fitted to a 2D Gaussian approximation of the point spread function (PSF): $I(x, y) = I_b + I_a e^{-((x-x_c)^2/2s_x^2) - ((y-y_c)^2/2s_y^2)}$, where $I(x, y)$ is the best-fit PSF, I_b is the background intensity, I_a is the amplitude, s_x and s_y are the Gaussian widths, and x_c and y_c are the centroid coordinate. The Thompson–Webb uncertainty of the centroid estimate⁵² is determined by: $\sigma_{x,y} = \sqrt{(s^2/N) + ((a^2/12)/N) + (8\pi s^2 b^2/a^2 N^2)}$, where $\sigma_{x,y}$ is the localization uncertainty, s is the peak width, N is the photon number, a is the pixel size, and b is the background photons. A z-coordinate calibration curve was measured by translating the piezo z stage over 2 μm at 25 nm steps, while imaging a fluorescent fiducial, yielding a plot of z versus ellipticity (ϵ), as defined by: $\epsilon = (\sigma_x - \sigma_y)/(\sigma_x + \sigma_y)$, which is then fitted to a polynomial function. Subsequently, z coordinates were extracted for each single molecule using ϵ calculated from the Gaussian fitting⁵³. Super-resolution images were reconstructed using a normalized 2D Gaussian to represent each molecule⁵⁴, with the widths corresponding to σ_x and σ_y . 3D data are rendered with colour encoding the z coordinate¹⁸.

Three-dimensional super-resolution microscopy by interferometric photoactivated localization microscopy (iPALM). The iPALM 3D super-resolution microscope system was built, calibrated, and operated as described earlier^{18,19,51} (Supplementary Fig. 2a). Briefly, a pair of dual-opposed 60× NA 1.49 Apo TIRF (Nikon Instruments) objective lenses were aligned and focused using Picomotors piezoelectric actuators (Newport). The custom-manufactured three-way Hess multiphase beamsplitter (Rocky Mountain Instruments) was positioned by a 5-axis Picomotor actuator (Newport). Optimal mutual phase interference was adjusted by a dielectric mirror on a z-tip-tilt piezoelectric mount (Physik Instrument), index-matched to the beamsplitter⁵¹. All major optical parts are mounted on custom-machined Invar parts to minimize drift. Three deep-cooled back-illuminated EMCCD cameras (Ixon Ultra, Andor) were used for acquisition of raw images in frame transfer mode (50 ms exposure time), each controlled by a dedicated computer. Room-temperature control was overridden prior to experiments by a custom-installed switch and allowed to equilibrate for minimal temperature fluctuation. Calibration,

alignment, and acquisition were performed using custom-written codes in LabVIEW (National Instruments), while image processing and data analysis were performed using custom-written IDL software, described previously^{18,19}. Light sources for excitation and photoswitching were 642 nm 100 mW and 405 nm 100 mW lasers (Coherent), respectively, with intensity and timing controlled by an AOTF (A-A Optoelectronics). Emission filters used for each camera are BrightLine FF01-676/37 and a 4-band notch filter, NF03-405488/561/635E-25 (Semrock), to reject stray excitation light. PHEM buffer supplemented with 100 mM cysteamine to promote blinking was used as the imaging buffer. Samples were sealed by epoxy and vaseline-paraffin mixture and mounted on a custom-machined stainless-steel holder equipped with dual piezo actuators (Physik Instruments). The *z*-coordinate was determined from a calibration curve recorded pre-acquisition for each imaging site by scanning the piezo sample holder in 8-nm steps (Supplementary Fig. 2b). Channel registration and drift correction was performed using plasmonic fiducials immobilized in coverglasses, while super-resolution images were reconstructed using hue-encoding for the *z* coordinate and normalized Gaussian as described previously¹⁸.

Nanoscale-precision *z*-position measurement by surface-generated structured illumination. The theoretical foundation and implementations of protein *z*-position mapping by surface-generated structured illumination techniques (variable incidence angle fluorescence interference contrast microscopy, or scanning angle interference microscopy) were described previously^{20,21}, and were performed on a Nikon Eclipse Ti inverted microscope (Nikon Instruments), with a motorized TIRF illuminator, a 60× NA 1.49 ApoTIRF objective lens, a sCMOS camera (Orca Flash 4.0, Hamamatsu), and a laser combiner (488 nm and 561 nm, Omicron Laserage) coupled with a polarization-maintaining optical fibre. The thermal oxide thickness of each batch of silicon wafers was determined to nanometre-precision using an ellipsometer (UV-VIS-VASE, JA-Woollam) at the Institute of Materials Research and Engineering, A-STAR, Singapore.

For imaging, the sample side of the silicon wafer was placed into a PBS-filled 27-mm glass-bottom dish (Iwaki), facing downward, maintained at neutral buoyancy by a thumb screw²⁷. Raw fluorescence image series were acquired at 4° incidence angle interval between 0° (normal) and 52°, as described previously²⁷, using pre-tabulated values for either 488 nm (for EGFP, mTFP1, or mEmerald) or 561 nm laser (for mCherry, mApple, or photoconverted EosFP), with a typical exposure time of 100–200 ms per frame. As needed, photoconversion of mEos2 and tEOS was carried out using LED excitation and a DAPI filter set (Lumencor SOLA). Two-colour measurements were performed sequentially. Analysis was performed using IDL-based custom-written software (available upon request). Simple or Otsu thresholding was used to generate binary masks for regions of interest (ROIs). Topographic height (*z*) and other model parameters were determined by Levenberg–Marquardt nonlinear least-square fitting, with multiple initial guesses for exhaustive search, for each pixel in the ROI²⁷. The median *z*-position value of each ROI was denoted z_{centre} , and used as the representative *z*-position for a given ROI. The representative protein positions, z_{median} , were obtained from the distributions of z_{centre} , such as shown in Supplementary Fig. 2h and Supplementary Fig. 5a,c. Alternative, histograms were calculated using the *z*-position of all pixels, and normalized with the integrated area set to unity to reflect the probability distribution of locating a protein as a function of *z*-position (Figs 3 and 4e,j and Supplementary Fig. 2i). Topographic *z* maps were plotted using colour to encode the *z*-position.

Fluorescent protein fusion constructs. The E-cadherin-EGFP expression vector was a gift from W. J. Nelson (Stanford University, USA). N-cadherin-EGFP was obtained from the Addgene depository (no. 18870, contributed by V. Vasioukhin, Fred Hutchinson Cancer Center, USA). The mouse α_E -catenin expression vector was created in the laboratory of R.-M.M. (Université Paris Diderot/CNRS, France), based on a previously described vector²⁵, as a dual tag construct with EGFP at the N terminus and mCherry at the C terminus in the pEGFP-C2 vector, via recombination of overlapping PCR products (Infusion, Clontech). Based on this, a dual tag construct with mApple at the N terminus and EGFP at the C terminus was also generated using a forward primer 5'-AAAAAAGGATCCCTGTCAGCTCGCCACCA TGGTGAGCAAGGGCGAG-3' and reverse primer 5'-GGGCCGAATTCTCT TGTACAGCTCGTCCATGC-3', for AgeI and EcoRI restriction sites. Forward primer 5'-AAAAAAGGATCCGGTGGATGTTGAGCAAGGGCGAGGA-3' and reverse primer 5'-AAAAAAGGATCCCTGTCAGCTCGTCCATGC-3' were used for PvuI and BamHI restriction sites for the cloning of EGFP to the C terminus of α_E -catenin. The α -catenin conformational FRET sensor⁹ and α -catenin delta ABD (actin-binding domain) FRET sensor were generously provided by Y. Wang (University of California, USA). N- and C-terminal EGFP fusions of β -catenin were provided by R. Kypta (MRC Laboratory for Molecular Cell Biology, University College London, UK) and described previously⁵⁶. EGFP fusion of p120-catenin was obtained from Reynolds laboratory, Vanderbilt University, Nashville,

Tennessee, and described previously⁵⁷. FP fusion constructs of vinculin, zyxin, VASP, vinexin, palladin, myosinIIA, myosinIIB, α -actinin, and ZO-1 were created in the laboratory of M.W.D., The Florida State University, and are available from Addgene depository.

EGFP-vinculin head (residues 1–258), the N-terminal fusion of vinculin-T12, and Vinculin 'tail-probe' conformational FRET sensor³⁵ were obtained from Addgene (no. 46270, no. 46266 and no. 46268 contributed by S. Craig, Johns Hopkins University, USA). The vinculin FRET-based tension sensor (TS) and tailless-tension sensor²⁹ were obtained from Addgene (no. 26019 and 26020, contributed by M. Schwartz, Yale University, USA). The C-terminal fusion of vinculin-T12 and the Y822E and Y822F mutants of vinculin were generated by H. Chen (MBI Protein Expression Facility, Singapore). Briefly, forward primer 5'-CCCTCGAGATGCCCGTCTCCACACGC-3' and reverse primer 5'-CGGAATTGCTGATACCATGGGGTTC-3', for XhoI and EcoRI sites, were used for the creation of the vinculin-T12 C-terminal fusion. The primer 5'-TTTCGGATCTGGGAGCTGTGGCCAAG-3' was used for the Y822F (the reverse primer is the same as for Y822E) mutagenesis based on wt-vinculin C-terminal fusion construct Y822E. EGFP fusions of the Eplin α and β isoforms were obtained from Addgene (no. 40947-8, contributed by E. Luna, University of Massachusetts Medical School, USA). RhoA-V12-EGFP construct was a gift from M. Sheetz (Mechanobiology Institute, Singapore). Rac1-V12-BFP and cdc42-Q61L-EGFP were gifts from C. Waterman (National Institutes of Health). Src Y529F was obtained from Addgene (no. 17686, contributed by D. Shalloway, Cornell University, USA). All constructs created in-house were verified by sequencing. Localizations to the cell–cell junctions were verified in MDCK or C2C12 cells plated on fibronectin, cultured to confluence, and imaged by epifluorescence microscopy (Supplementary Fig. 4a,f).

Western blot analysis. Whole-cell lysates of MDCK cells (control), MDCK with stable expression of shRNA against vinculin (Vcl-KD)³⁴ or α -catenin (α -catenin KD)³³ and C2C12 cells were prepared in 1× RIPA lysis buffer (Pierce) supplemented with 1× protease inhibitor cocktail (04693159001, Roche). Cells were freeze–thawed thrice at –80 °C and clarified by centrifugation at 4 °C at 14,000 r.p.m. (21,000g) for 20 min. Protein amounts in the supernatants were quantified by the BCA Pierce kit (Thermo Scientific). Thirty micrograms was separated via SDS–PAGE using 4–15% Mini-PROTEAN TGX Precast Protein Gels (Bio-Rad) and transferred to Immobilon-P PVDF (poly-vinylidene fluoride) membranes. The membranes were blocked for 1 h at room temperature with 5% non-fat dry milk (wt/vol) in TBS-T buffer (0.1% vol/vol of Tween-20 in 1× TBS buffer solution, no. 1706435 Bio-Rad), and were subsequently incubated for 1 h at room temperature or overnight at 4 °C with antibodies in 3% non-fat dry milk (wt/vol) in TBS-T buffer. Antibodies used were: vinculin (V9131, Sigma), 1:5,000; α -catenin (EP1793Y, Sigma), 1:10,000; Abl kinase (no. ab15130, Abcam), 1:500; PTP1B (no. ab124375, Abcam), 1:500; and α -tubulin (Abcam ab18251), 1:5,000. After primary antibody incubation, the membranes were washed once in TBS-T, once in 2.5% non-fat dry milk (wt/vol) in TBS-T buffer, and once in 5% non-fat dry milk (wt/vol) in TBS-T buffer (10 min each). After the washing steps, the membranes were incubated with the appropriate horse radish peroxidase-conjugated antibodies in 3% non-fat dry milk (wt/vol) in TBS-T buffer at a dilution of 1:5,000. After secondary antibody incubation, membranes were washed three times in TBS-T (10 min each). The membranes were then incubated for 3–5 min with SuperSignal West Pico Chemiluminescent Substrate and imaged using the Chemidoc MP Gel Documentation System (Bio-Rad). In case of PVDF membrane reprobing by different antibodies, the membranes were stripped using Restore Western Blot Stripping Buffer (21059, Thermo Scientific) for 15 min, washed in TBS-T for 10 min, and blocked in 5% non-fat dry milk (wt/vol) in TBS-T buffer at 4 °C overnight.

Preparation of compliant substrates. Soft substrates, used for FRET experiments, were generated using Cy52-276 silicone (Dow Corning). The two components (A and B) of the silicone were mixed at 1:1 ratio (w/w). Approximately 50 μ l of the viscous mixture was placed in the centre of a coverglass and spread into a thin film by a spin-coater (1 min at 800 r.p.m.) to achieve a thickness of ~50 μ m. The silicone gel was allowed to crosslink for 2 h at 80 °C to obtain a final Young's modulus of ~15 kPa (ref. 58). The silicon-coated glass coverslips were then treated for E- or N-cadherin deposition as described above.

Forster resonance energy transfer (FRET) measurements. The method of acceptor photobleaching was used to measure the FRET efficiency for intramolecular tension in vinculin (Vinculin-TS)²⁹, conformational change in the vinculin tail region (tail-probe)³⁵, and conformational change in α -catenin⁹. These constructs rely on FRET between the donor in the cyan fluorescent protein channel (mTFP1, CFP or ECFP) and the acceptor in the yellow fluorescent protein channel (YFP, YPet or Venus). MDCK and C2C12 cells were transfected with the FRET sensors or their respective control constructs, and cultured on E- or N-cadherin substrates described above. Imaging was performed using a Nikon Eclipse Ti-E inverted microscope

(Nikon) equipped with a spinning-disc confocal unit, CSU-W1 (Yokogawa), an iLas² illumination system, and a ProEM HS EMCCD camera (Princeton instruments). The objective lens used was a CFI Plan Apo 100× NA 1.45 oil immersion (Nikon).

Nine consecutive images were acquired every two seconds using the settings shown in Supplementary Table 4. Cross-excitation and cross-emission between channels were determined to be negligible. After the fourth acquisition, acceptor photobleaching in an ROI was carried out by scanning the 514 nm laser at 10 mW power for 180 ms. Acquired images were background subtracted and thresholded to segment for cadherin adhesions. Donor and acceptor images were adjusted for structural photobleaching⁵⁹. FRET efficiency extrapolated for full acceptor photobleaching (extFRETEff) was calculated⁶⁰ as follows: $\text{extFRETEff} = 1 - (\alpha \times D^b / (D^a - (\beta \times D^b)))$, where D^b and D^a are the intensities of the donor before (second acquisition) and after acceptor photobleaching (third acquisition), respectively. α and β are the correction factors and are calculated as follows: $\alpha = 1 - \beta$, and $\beta = (A^a / A^b)$, where A^b and A^a are the intensities of the acceptor before (second acquisition) and after (third acquisition) photobleaching, respectively.

Laser ablation of cell–cell junctions. Cell–cell junctions in MDCK epithelial monolayers were selectively excised by UV laser nanoscissor ablation performed on a Nikon A1R MP laser scanning confocal microscope, equipped with an ultraviolet laser (PowerChip PNV-0150-100, Team Photonics: 355 nm, 300 ps pulse duration, 1 kHz repetition rate). The UV laser beam was merged onto the optical axis via a customized optical path and a dichroic filter, with the beam controlled independently from the microscope to allow simultaneous ablation and imaging. The beam position was steered by a mirror mounted on two linear actuators (TRA12CC), adjusted via an actuator controller (ESP301-3G). The exposure time was controlled by a mechanical shutter (VS25S2ZM0, Uniblitz). A custom ImageJ plug-in was used to control both the actuators and the shutter⁶¹. Laser ablation was carried out at the z -plane of adherens junctions using 15 nW laser power focused at the back aperture of the objective lens with an exposure time of 350 ms. Time-lapse confocal images were acquired every 2 s, starting from 3 frames prior to the ablation until 30 frames post-ablation with a scan speed of 1 frame s^{-1} , and a pinhole size of 74 μm .

Image analysis of the recoil speed was performed in ImageJ using the MTrackJ plug-in⁶². This plug-in allows the tracking of the two edges of the cut in subsequent frames and extracts the coordinates of the two points of time. The recoil speed ($\mu\text{m s}^{-1}$) was defined as the rate of change of the two edges⁶³. The initial recoil speeds were measured using the first 2 s after ablation.

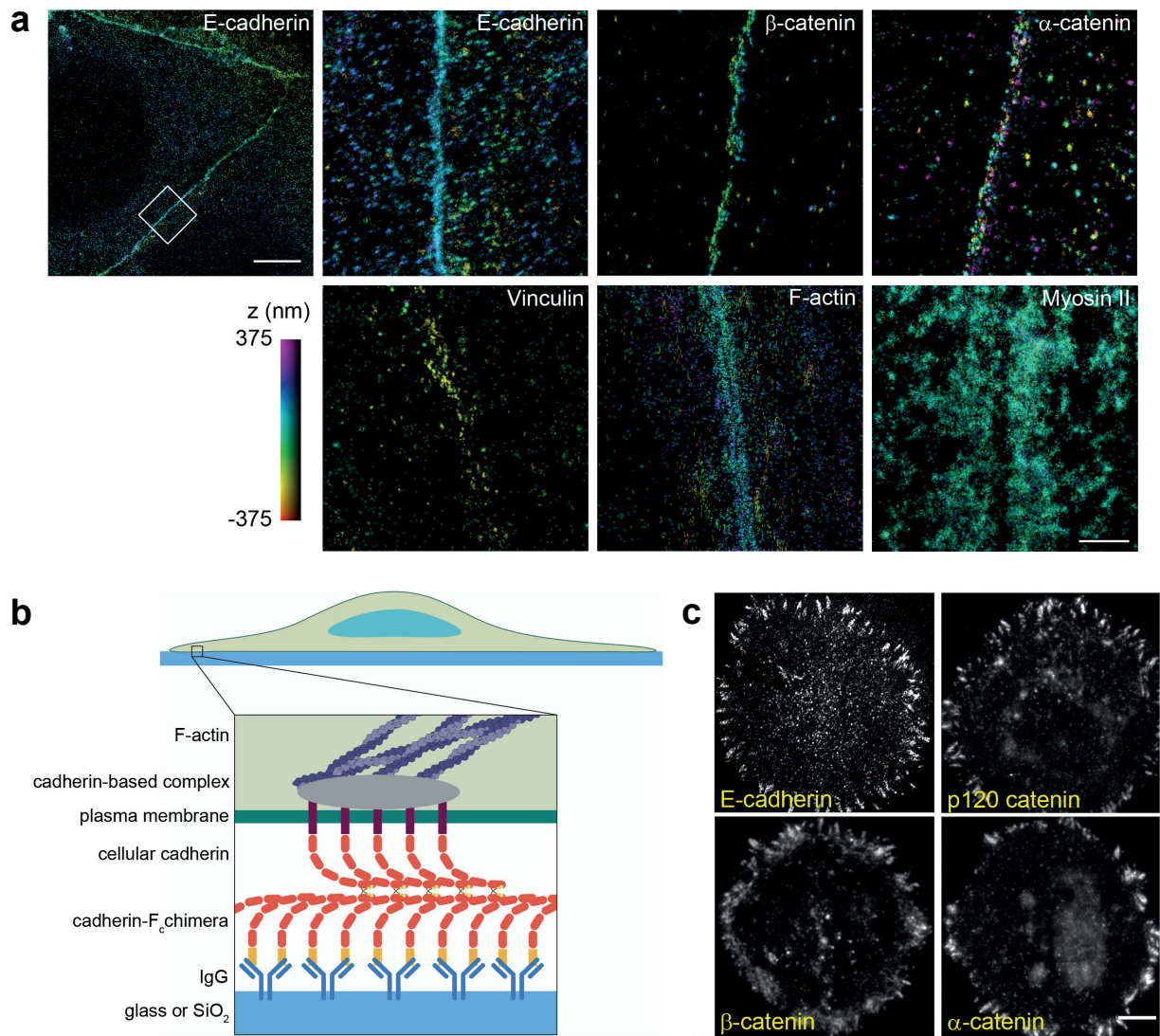
Statistics and reproducibility. Plotting and statistical analysis for super-resolution z -position measurements and FRET (Welch's t -test), and laser ablation data (one-way ANOVA, followed by pairwise Tukey test), were performed using OriginPro software (Northampton). For protein z -position, data are presented as the median, with the full distribution shown in Fig. 3 and Supplementary Fig. 5, and the mean, median, and standard deviation, and n values (number of adhesions) in

Supplementary Tables 1–3. P values (Welch's t -test) are indicated in Supplementary Table 4. For laser ablation experiments, the mean, standard deviation, s.e.m., and n are indicated in Supplementary Table 6, with pairwise Tukey test in Supplementary Table 7. Differences were considered significant at $P < 0.05$ (as stated in each individual figure legend). Western blots and immunofluorescence microscopy were performed with at least three independent repeats. All representative microscopy images are presented with quantification of the entire data set. Detailed information on replication of experiments can be found indicated on the plots and in their corresponding legends. For determination of sample size, s.d. from initial trials was used to estimate the sample size based on confidence interval calculations at confidence levels of 95%. The number of adhesions analysed was assessed from 9–30 cells from at least 3 independent sample preparations per condition.

Code availability. Computation code used in this study is available from the corresponding author on request.

Data availability. All data supporting the conclusions are available from the corresponding author on request.

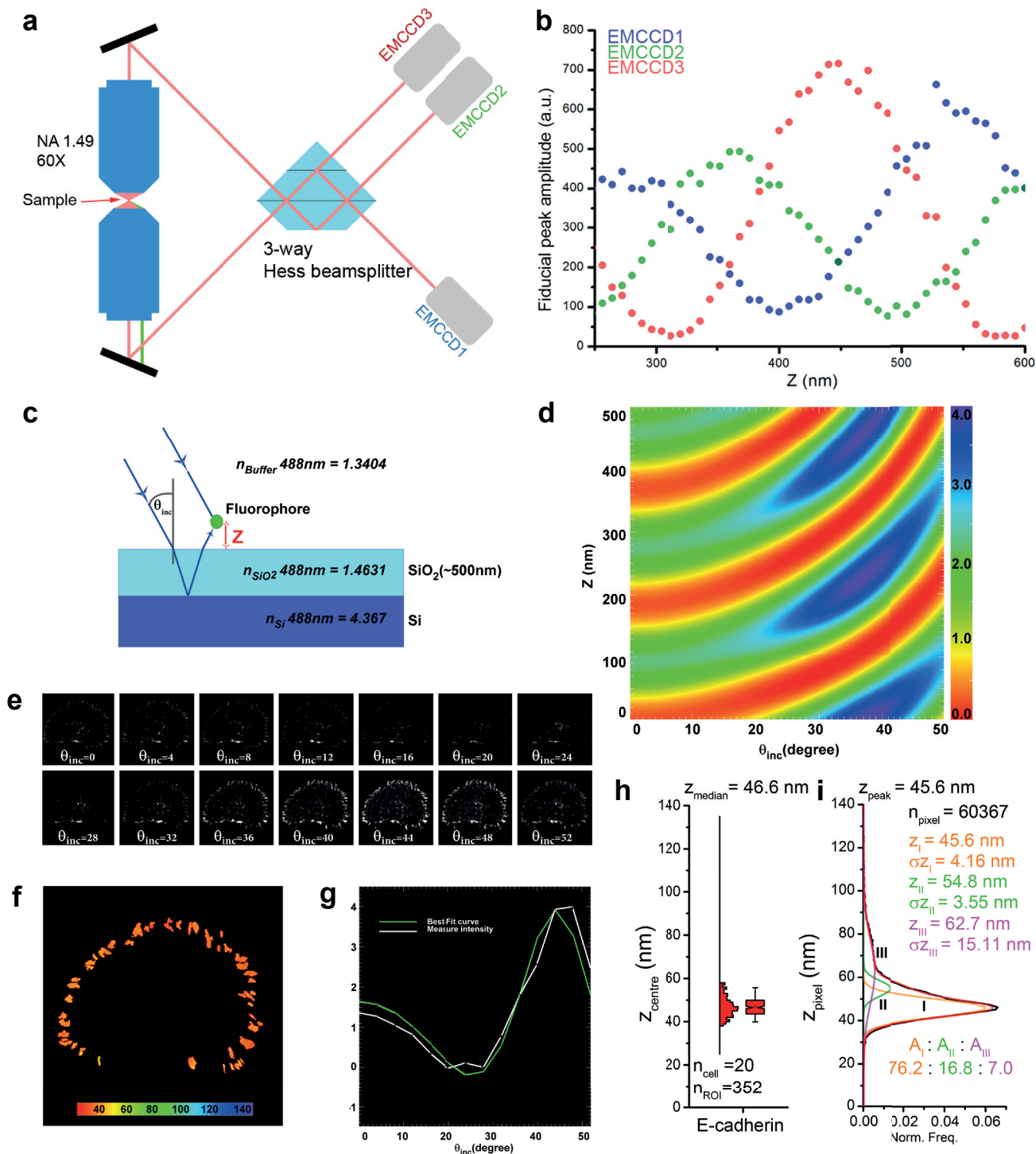
52. Thompson, R. E., Larson, D. R. & Webb, W. W. Precise nanometer localization analysis for individual fluorescent probes. *Biophys. J.* **82**, 2775–2783 (2002).
53. Brown, T. A. *et al.* Superresolution fluorescence imaging of mitochondrial nucleoids reveals their spatial range, limits, and membrane interaction. *Mol. Cell. Biol.* **31**, 4994–5010 (2011).
54. Betzig, E. *et al.* Imaging intracellular fluorescent proteins at nanometer resolution. *Science* **313**, 1642–1645 (2006).
55. Thomas, W. A. *et al.* α -Catenin and vinculin cooperate to promote high E-cadherin-based adhesion strength. *J. Biol. Chem.* **288**, 4957–4969 (2013).
56. Giannini, A. L., Vivanco, M. M. & Kypta, R. M. Analysis of β -catenin aggregation and localization using GFP fusion proteins: nuclear import of α -catenin by the β -catenin/Tcf complex. *Exp. Cell Res.* **255**, 207–220 (2000).
57. Roczniak-Ferguson, A. & Reynolds, A. B. Regulation of p120-catenin nucleocytoplasmic shuttling activity. *J. Cell Sci.* **116**, 4201–4212 (2003).
58. Rivasio, A. *et al.* Regulation of epithelial cell organization by tuning cell–substrate adhesion. *Integr. Biol.* **7**, 1228–1241 (2015).
59. Hodgson, L., Nalbant, P., Shen, F. & Hahn, K. Imaging and photobleach correction of Mero-CBD, sensor of endogenous Cdc42 activation. *Methods Enzymol.* **406**, 140–156 (2006).
60. Jobin, C. M. *et al.* Receptor-regulated dynamic interaction between endothelial nitric oxide synthase and calmodulin revealed by fluorescence resonance energy transfer in living cells. *Biochemistry* **42**, 11716–11725 (2003).
61. Hutson, M. S. *et al.* Forces for morphogenesis investigated with laser microsurgery and quantitative modeling. *Science* **300**, 145–149 (2003).
62. Meijering, E., Dzyubachyk, O. & Smal, I. Methods for cell and particle tracking. *Methods Enzymol.* **504**, 183–200 (2012).
63. Rivasio, A. *et al.* Gap geometry dictates epithelial closure efficiency. *Nat. Commun.* **6**, 7683 (2015).



Supplementary Figure 1 Planarized biomimetic cadherin substrate a, Superresolution microscopy of Adherens Junctions (AJs) in epithelial monolayer. Astigmatism-based 3D superresolution microscopy of Eph4 cell monolayer, showing the organization of E-cadherin (Top left and second to left), zoomed area corresponds to top left inset, and other key proteins (all other panels, cell-cell contacts aligned approximately vertically). E-cadherin, β -catenin, α -catenin, vinculin, and myosin IIA were probed using primary and Alexa Fluor 647-labeled secondary antibodies. F-actin is probed by Alexa Fluor 647-phalloidin. Color bar: z-position from -375 to 375 nm. Scale bars: 5 μ m (top left), 1 μ m (all other panels). b, Model

of planarized biomimetic (N- or E-) cadherin-Fc substrate. Silanized glass coverslips or silicon wafers were coated by anti-Fc IgG, followed by purified cadherin-Fc chimeric protein. Cells were seeded onto the substrate in absence of serum to avoid extracellular matrix deposition so that adhesions were formed primarily via cellular cadherin engagement to the substrate-bound cadherin-Fc. c, E-cadherin-based adhesions recruited canonical cell-cell junction proteins. MDCK cells expressing EGFP fusions of E-cadherin, p120 catenin, β -catenin, and α -catenin, spreading on E-cadherin-coated substrate, fixed and imaged after 3 h. Cadherin and associated proteins localize to clusters at cell edge and lamellipodia. Scale bar, 5 μ m.

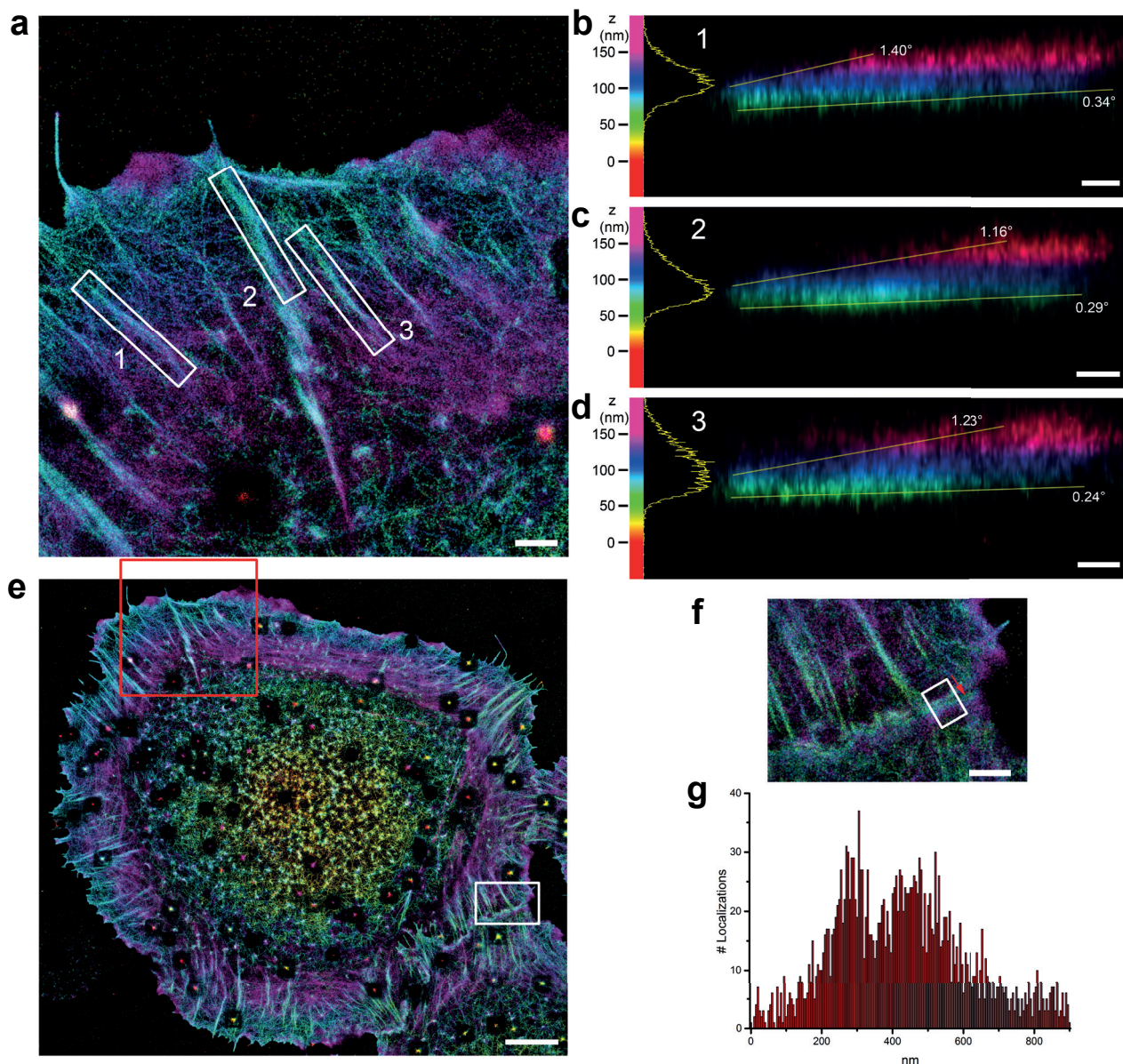
SUPPLEMENTARY INFORMATION



Supplementary Figure 2 Nanoscale Fluorescence Imaging Methods. a, Schematics for interferometric PhotoActivated Localization Microscopy (iPALM). For details see Methods section. b, iPALM calibration curve, measured by piezo-based translation along z-axis at 8-nm step. Amplitudes of a fluorescent fiducial observed in EMCCD 1-3 exhibit oscillation with mutual $\sim 120^\circ$ phase differences. c, Principles of surface-generated structured illumination, (VIAFLIC, Variable Incidence Angle Fluorescence Interference Contrast; or SAIM, Scanning Angle Interference Microscopy)^{20,21}. d, Intensity of the fluorescence excitation field as a function of incidence angle (θ_{inc}) and fluorophore z-position (nm). e, Montage showing the variation of fluorescence intensity with θ_{inc} (degree). f, Topographic z-position map of fluorophores (E-cadherin-EGFP expressed in

MDCK cell). Z-position is calculated pixel-by-pixel by least-square fitting of the measured angle-dependence curve (white) to theoretical model (green), as show in g. h, Notched box plots and histograms for z-position calculated from the median of each adhesion ROI: first and third quartiles, median and confidence intervals; whiskers, 5th and 95th percentiles. Histogram bin size, 1 nm. The median of this distribution is the representative protein z-position, zcentre. n=352 adhesions (nROI) pooled from 20 cells (ncell). i, Profile of E-cadherin distribution along the z-axis. Normalized histogram (black, 1-nm bin) of pixel z-position. Also shown are the decomposition into 3 Gaussian functions along with the Gaussian centers (zI, zII, zIII), widths (σz_I , σz_{II} , σz_{III}), and relative amplitude (AI, AII, AIII). Peak z-position of the distribution (zpeak) and number of pixels analyzed (npixel) indicated.

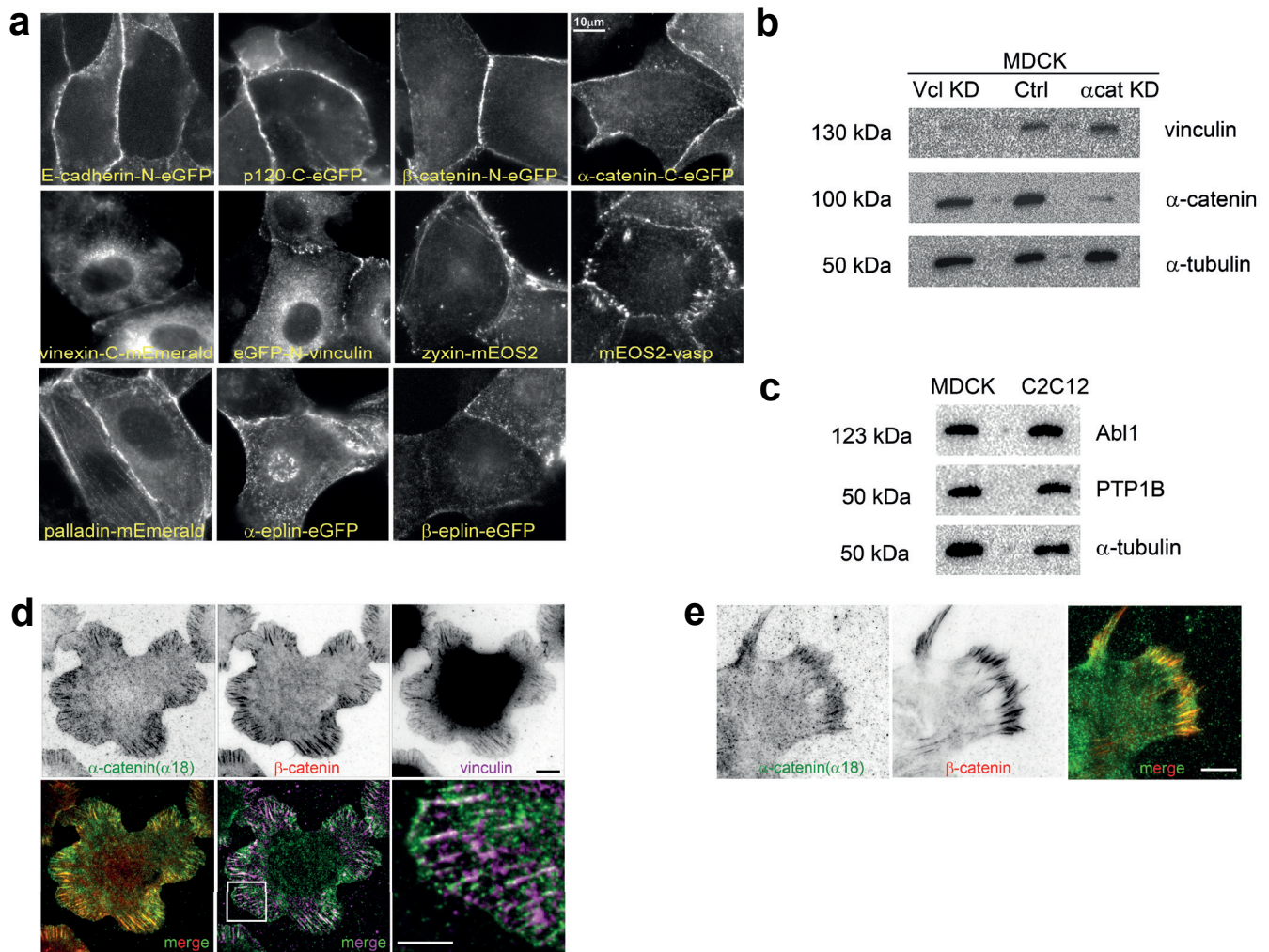
SUPPLEMENTARY INFORMATION



Supplementary Figure 3 iPALM superresolution images of F-Actin, F-actin organization at the edge of a MDCK cell cultured on planar cadherin substrate. b-d, Side view iPALM images of regions 1-3 in (a). Yellow lines approximate the envelope of the actin bundles, angles indicated. Horizontal scale indicated by the scale bars; vertical (z) scale indicated by colour bars. e, Zoomed-out view of the cell shown in a. Red box, area shown in a. White box, area of cell-cell contacts shown in f. g, Histogram of actin density

(number of single-molecule localizations per 5-nm bin) for white box area in f. Red arrow in f indicates horizontal axis direction in g. Peaks at ~300 and ~450 nm bracket the intercellular space seen as low density gap in e, f. Bright dots surrounded by dark halos in a, e are due to substrate-embedded fluorescent nanoparticles used as fiducials for calibration and alignment. Color bars, z-position (0-150 nm) relative to substrate surface, shown in b-d. Scale bars: 1 μ m (a, f), 250 nm (b-d), 5 μ m (e).

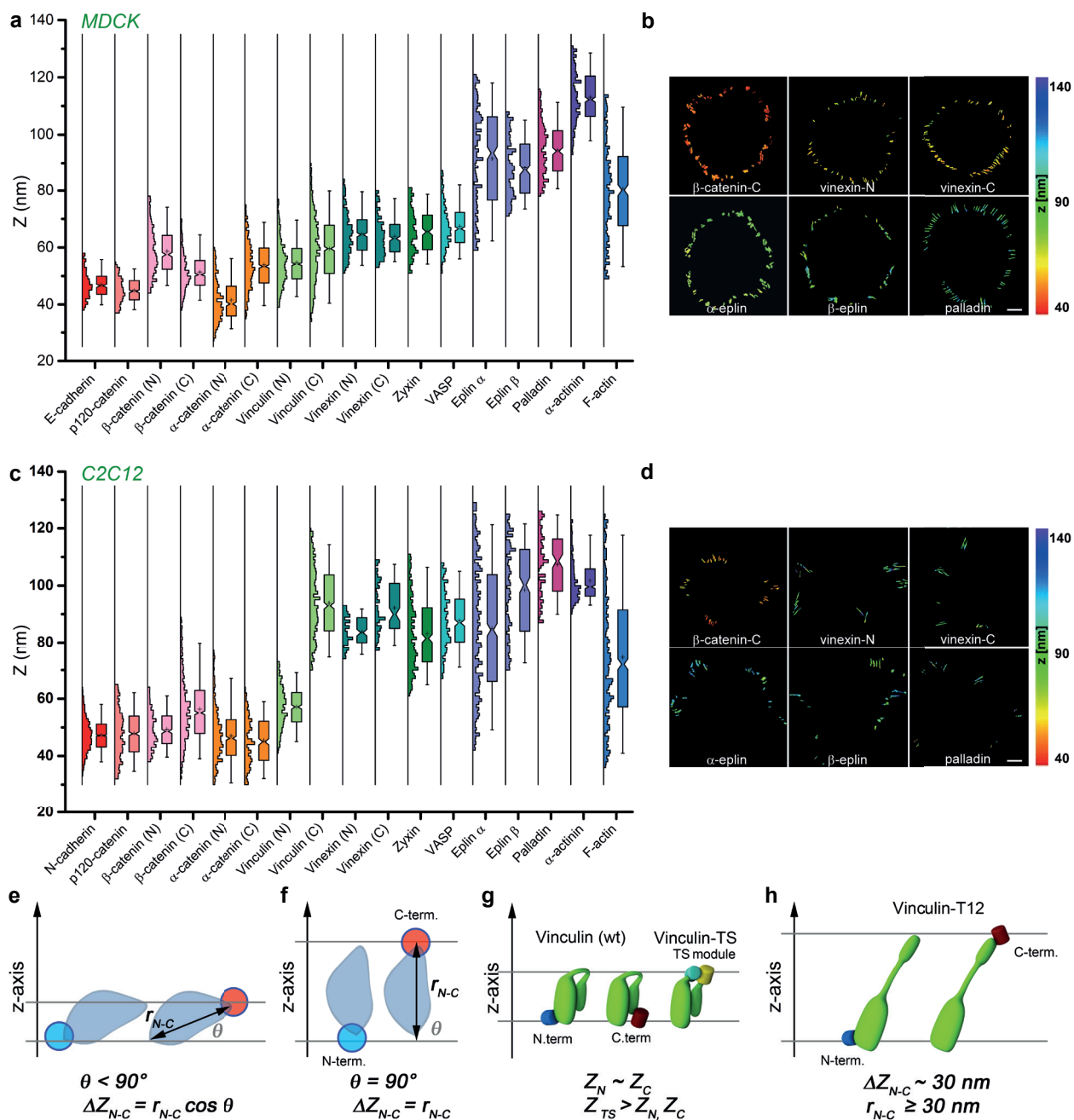
SUPPLEMENTARY INFORMATION



Supplementary Figure 4 Localization and expression of cadhesome proteins. **a**, Fluorescence micrographs of MDCK epithelial monolayer expressing fusion constructs. Protein names indicate the FP used and tag position (e.g. E-cadherin-EGFP: C-terminal EGFP tag): E-cadherin-EGFP; EGFP-p120 catenin; EGFP-β-catenin; α-catenin-EGFP; vinexin-mEmerald; EGFP-vinculin; zyxin-mEos2; mEOS2-VASP; palladin-mEmerald; α-eplin-eGFP; β-eplin-EGFP. Scale bar: 10 μm. **b**, Western blots of cell lysates from MDCK (control), and MDCK with stable expression of vinculin shRNA (Vcl KD) and α-catenin shRNA (α-cat KD), probed for vinculin, α-catenin. Loading control, α-tubulin. **c**, Abl1 kinase and PTP1B are expressed in both MDCK and C2C12 cells. Western blot analysis of lysates from MDCK and C2C12, probed for

Abl1 and PTP1B, with α-tubulin as loading control. **d**, Epifluorescence micrographs of MDCK cells seeded on E-cadherin-Fc substrate, stained with α18 antibody for activated α-catenin, β-catenin, and vinculin. (Top row) Inverted contrast, single channel images. (Bottom row) Merged 2-channel images of α-catenin (green) and β-catenin (red), and α-catenin (green) and vinculin (magenta). (Bottom right) Zoom-in view for area in centre panel, highlighting relative distribution of α-catenin and vinculin at cell edges. Scale bar, 10 μm (5 μm for bottom right panel). **e**, Epifluorescence micrographs of C2C12 cells seeded on N-cadherin-Fc substrate, stained with α18 antibody for activated α-catenin and β-catenin. Single channel (inverted contrast) and merged 2-channel images of α-catenin (green) and β-catenin (red). Scale bar, 10 μm.

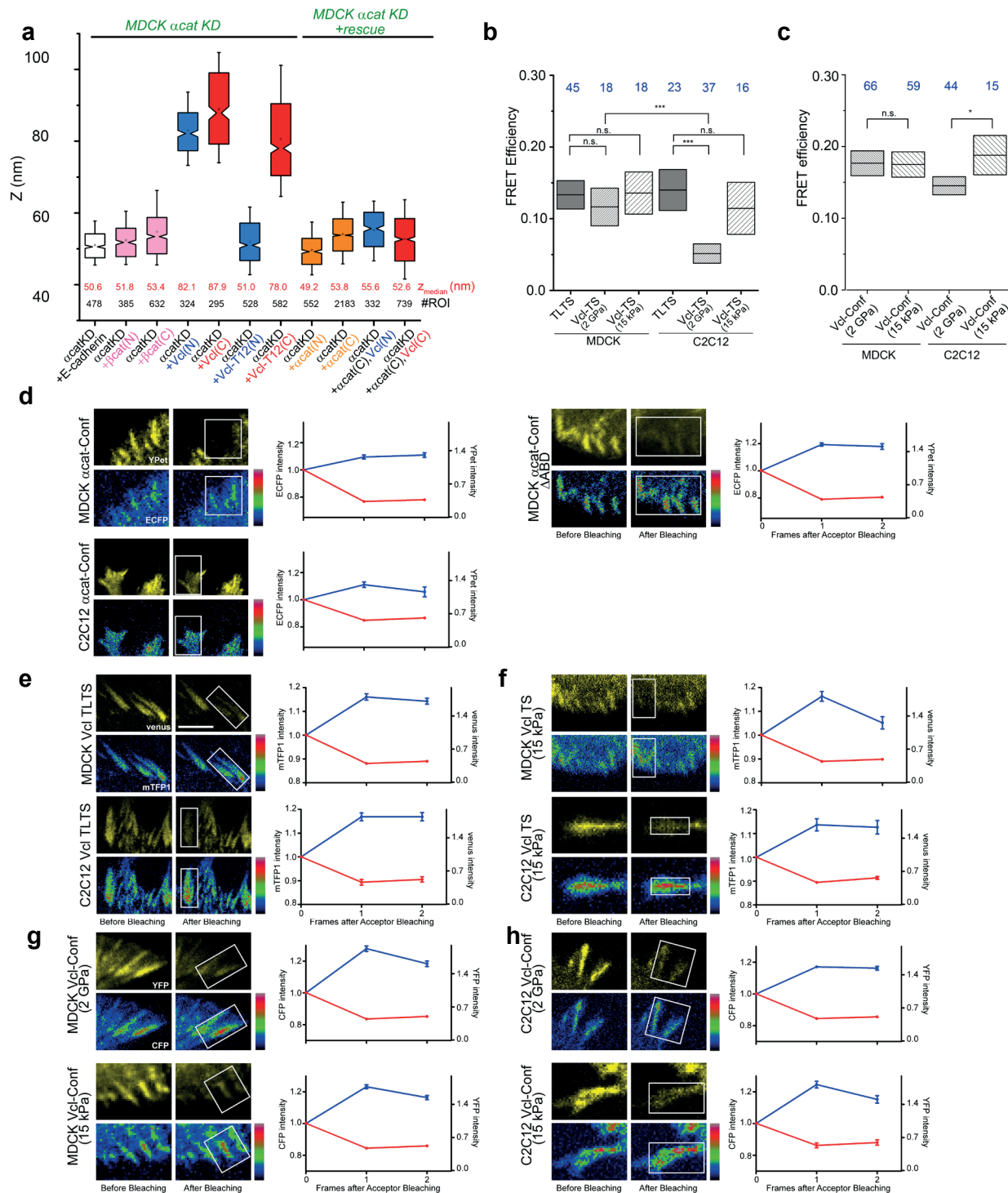
SUPPLEMENTARY INFORMATION



Supplementary Figure 5 Measurements of protein positions and orientation in cadherin-based adhesions a and c, Notched box plots and histograms for z-position of indicated proteins in MDCK (a) and C2C12 (c) cells: first and third quartiles, median and confidence intervals; whiskers, 5th and 95th percentiles. n values (number of adhesions) are described in Supplementary Tables 1 and 2. Histogram bin size, 1 nm. b and d, Topographic map of z-positions (nm) for proteins not displayed in Fig. 2 in cadherin-based adhesions of MDCK (b) and C2C12 (c) cells. Colour bar indicates z-position relative to substrate surface. Scale bar, 10 μ m. e-f, Inference of protein orientation from z-position of fluorophores. Difference in Z-position of N-terminus (blue) and C-terminus (red) z-position, ΔZ_{N-C} , is a z-projection

of the N-C distance in the molecular frame, r_{N-C} . For oblique protein orientation ($\theta < 90^\circ$), $\Delta Z_{N-C} < r_{N-C}$, while for perpendicular orientation ($\theta = 90^\circ$), $\Delta Z_{N-C} = r_{N-C}$. g, Inference of protein conformation from 3-point z-position measurement. The z-position of the N-terminus, Z_N , C-terminus, Z_C , and mTFP1 in vinculin-tension sensor, ZTS, serve as constraints that can be satisfied only by the compact vinculin conformation. Illustrations approximate FP positions in a coarse-grained model of vinculin. h, Elongated conformation of vinculin-T12. Since $r_{N-C} \geq \Delta Z_{N-C}$, the large (~ 30 nm) observed for ΔZ_{N-C} indicates an elongated conformation, and a large separation between VH and VT domain of vinculin, indicating a relief of autoinhibition.

SUPPLEMENTARY INFORMATION



Supplementary Figure 6 Spatial organization and configurations of vinculin and α -catenin in cadherin-based adhesions a, Notched box plots for z-center of indicated proteins in MDCK α -catenin KD cells: first and third quartiles, median and confidence intervals; whiskers, 5th and 95th percentiles. n values (number of adhesions) are indicated in Supplementary Table 3. Absence of α -catenin results in an upshifted of vinculin z-position to the actin compartment (blue and red column on left, for N- and C-terminal vinculin, respectively), rescued upon α -catenin re-expression (orange). Positioning of vinculin T12 in MDCK α -catenin KD cells could be due to β -catenin interaction with open vinculin. b-c, Tension (b) or conformation (c) of vinculin as reported by FRET sensors for cells on soft (15 kPa) and stiff (glass, 2GPa) planar cadherin substrate. Box plots: median, first and third quartile.

Representative frames from FRET measurement by acceptor photobleaching for, f, α -cat-conf or α -cat-conf Δ ABD, expressed in MDCK or C2C12 cells; g, h Vinculin tension-sensor (Vcl-TS) and tailless tension-sensor control (Vcl-TLTS), i, j Vinculin tail-probe conformation sensor (Vcl-conf) expressed in MDCK or C2C12 cells plated on stiff (glass, 2GPa) and soft substrate (15 kPa), respectively. (Left columns), acceptor channel images (YPet, venus, YFP) and donor channel images (ECFP, mTFP1, CFP) for pre-bleach and post-bleach. (Right columns), plots of relative intensity changes for acceptor (red) and donor (blue), measured from the ROI (white boxes on left) for three consecutive frames after acceptor photobleaching. Data are represented as mean \pm s.e.m.; n values (number of measurements) are indicated in blue in b and c. *, $p < 0.05$, ***, $p < 5 \times 10^{-4}$. Welch's t-test. Scale bar, 5 μ m.

Supplementary Table Legends

Supplementary Table 1 Statistics of protein z-positions in cadherin-based adhesions of MDCK cells.

Protein z-positions in MDCK (Madin-Darby Canine Kidney) epithelial cells measured by surface-generated structured illumination^{20,21}. Measurements performed using fluorescent protein (FP) fusion, except for F-actin, where phalloidin-conjugated fluorophore is used instead. (N) or (C) indicates the positions of the FP probes at the amino- or carboxy- terminus of the protein, respectively. Zpeak, FWHM, and Npixels indicate the maximum of the z-profile plot, the full-width-at-half-maximum-and the number of pixels analyzed, respectively. Histograms were calculated using 1-nm bin using all analyzed pixel with $\sigma < 10\text{nm}$.

Supplementary Table 2 Statistics of protein z-positions in cadherin-based adhesions of C2C12 cells. Protein z-positions in C2C12 murine myoblast epithelial cells measured by surface-generated structured illumination^{20,21}. Measurements performed using fluorescent protein (FP) fusion, except for F-actin, where phalloidin-conjugated fluorophore is used instead. (N) or (C) indicates the positions of the FP probes at the amino- or carboxy- terminus of the protein, respectively. Zpeak, FWHM, and Npixels indicate the maximum of the z-profile plot, the full-width-at-half-maximum-and the number of pixels analyzed, respectively. Histograms were calculated using 1-nm bin using all analyzed pixel with $\sigma < 10\text{nm}$.

Supplementary Table 3 Z-position measurements for vinculin and associated proteins. Statistics of z-positions of vinculin or related constructs, measured in MDCK (Madin-Darby Canine Kidney) epithelial cells, C2C12 murine myoblast cells, or MDCK cells with stable shRNA knockdown against vinculin or β -catenin (MDCK Vcl KD and MDCK α cat KD, respectively), along with indicated perturbations. (N) or (C) indicates the positions of the FP probes at the amino or carboxy terminus of the protein, respectively. T12 indicates the constitutively active mutants of vinculin, while TS and TL-TS indicate the tension sensor, and tailless tensions constructs of vinculin²⁹.

Supplementary Table 4 Statistical test for protein z-position measurements. Welch's t-test of important pairs of measurements, with the null hypothesis being equal mean, for the box and whisker plots in indicated figure. * indicates p-value less than the minimum value of double precision number ($\sim 4.9\text{E-}324$).

Supplementary Table 5 Optical configurations used for FRET measurements by acceptor photobleaching

Supplementary Table 6 Statistics of cell-cell junction ablation experiments. Statistics of the cell-cell junction recoil after UV laser ablation for Madin-Darby Canine Kidney cells (MDCK ctrl) or MDCK with stable expression of vinculin shRNA (Vcl-KD). Cells were transfected with Z01-mEmerald or Z01-mApple and vinculin constructs as indicated and cultured to confluence on fibronectin-coated coverglass, prior to the ablation experiments.

Supplementary Table 7 Pairwise Statistical Test for Laser Ablation Experiments. Tukey's test between all pairs of recoil rate measurements from the UV laser ablation of MDCK cell-cell junctions. LCL and UCL indicate lower and upper confidence level, respectively.

Supplementary References

- 1 Kanchanawong, P. et al. Nanoscale architecture of integrin-based cell adhesions. *Nature* 468, 580-584 (2010).
- 2 Shtengel, G. et al. Imaging cellular ultrastructure by PALM, iPALM, and correlative iPALM-EM. *Methods Cell Biol* 123, 273-294, doi:10.1016/B978-0-12-420138-5.00015-X (2014).
- 3 Dani, A., Huang, B., Bergan, J., Dulac, C. & Zhuang, X. Superresolution imaging of chemical synapses in the brain. *Neuron* 68, 843-856, doi:10.1016/j.neuron.2010.11.021 (2010).
- 4 Huang, B., Bates, M. & Zhuang, X. Super-resolution fluorescence microscopy. *Annual review of biochemistry* 78, 993-1016 (2009).
- 5 Patterson, G., Davidson, M., Manley, S. & Lippincott-Schwartz, J. Superresolution imaging using single-molecule localization. *Annual review of physical chemistry* 61, 345-367 (2010).
- 6 Betzig, E. et al. Imaging intracellular fluorescent proteins at nanometer resolution. *Science (New York, N.Y)* 313, 1642-1645 (2006).
- 7 Yonemura, S., Itoh, M., Nagafuchi, A. & Tsukita, S. Cell-to-cell adherens junction formation and actin filament organization: similarities and differences between non-polarized fibroblasts and polarized epithelial cells. *Journal of cell science* 108 (Pt 1), 127-142 (1995).
- 8 Buckley, C. D. et al. Cell adhesion. The minimal cadherin-catenin complex binds to actin filaments under force. *Science (New York, N.Y)* 346, 1254211, doi:10.1126/science.1254211 (2014).
- 9 Pertsinidis, A., Zhang, Y. & Chu, S. Subnanometre single-molecule localization, registration and distance measurements. *Nature* 466, 647-651 (2010).
- 10 Huang, B., Wang, W., Bates, M. & Zhuang, X. Three-dimensional super-resolution imaging by stochastic optical reconstruction microscopy. *Science (New York, N.Y)* 319, 810-813 (2008).
- 11 Thompson, R. E., Larson, D. R. & Webb, W. W. Precise nanometer localization analysis for individual fluorescent probes. *Biophys J* 82, 2775-2783 (2002).
- 12 Mortensen, K. I., Churchman, L. S., Spudich, J. A. & Flyvbjerg, H. Optimized localization analysis for single-molecule tracking and super-resolution microscopy. *Nature Methods* 7, 377-381 (2010).
- 13 Shroff, H. et al. Dual-color superresolution imaging of genetically expressed probes within individual adhesion complexes. *Proceedings of the National Academy of Sciences of the United States of America* 104, 20308-20313 (2007).
- 14 Wu, Y., Kanchanawong, P. & Zaidel-Bar, R. Actin-delimited adhesion-independent clustering of e-cadherin forms the nanoscale building blocks of adherens junctions. *Developmental Cell* 32, 139-154, doi:10.1016/j.devcel.2014.12.003 (2015).
- 15 Xu, K., Babcock, H. P. & Zhuang, X. Dual-objective STORM reveals three-dimensional filament organization in the actin cytoskeleton. *Nature Methods* 9, 185-188, doi:10.1038/nmeth.1841 (2012).
- 16 Lukinavicius, G. et al. Fluorogenic probes for live-cell imaging of the cytoskeleton. *Nature Methods* 11, 731-733, doi:10.1038/nmeth.2972 (2014).
- 17 Ries, J., Kaplan, C., Platonova, E., Eghlidi, H. & Ewers, H. A simple, versatile method for GFP-based super-resolution microscopy via nanobodies. *Nature Methods* 9, 582-584, doi:10.1038/nmeth.1991 (2012).
- 18 Fernández-Suárez, M. & Ting, A. Y. Fluorescent probes for super-resolution imaging in living cells. *Nature Reviews Molecular Cell Biology* 9, 929-943 (2008).
- 19 Shtengel, G. et al. Interferometric fluorescent super-resolution microscopy resolves 3D cellular ultrastructure. *Proceedings of the National Academy of Sciences of the United States of America* 106, 3125-3130 (2009).

- 20 Paszek, M. J. et al. Scanning angle interference microscopy reveals cell dynamics at the nanoscale. *Nature Methods* 9, 825-827, doi:10.1038/nmeth.2077 (2012).
- 21 Ajo-Franklin, C. M., Ganesan, P. V. & Boxer, S. G. Variable incidence angle fluorescence interference contrast microscopy for z-imaging single objects. *Biophysical Journal* 89, 2759-2769, doi:10.1529/biophysj.105.066738 (2005).
- 22 Press, W. H., Teukolsky, S. A., Vetterling, W. T. & Flannery, B. P. *Numerical recipes in C*. Vol. 2 (Citeseer, 1996).
- 23 Borghi, N. et al. E-cadherin is under constitutive actomyosin-generated tension that is increased at cell-cell contacts upon externally applied stretch. *Proc Natl Acad Sci U S A* 109, 12568-12573, doi:10.1073/pnas.1204390109 (2012).
- 24 Liu, J. et al. Talin determines the nanoscale architecture of focal adhesions. *Proceedings of the National Academy of Sciences*, 201512025 (2015).
- 25 Grashoff, C. et al. Measuring mechanical tension across vinculin reveals regulation of focal adhesion dynamics. *Nature* 466, 263-266, doi:10.1038/nature09198 (2010).
- 26 Chen, H., Cohen, D. M., Choudhury, D. M., Kioka, N. & Craig, S. W. Spatial distribution and functional significance of activated vinculin in living cells. *The Journal of cell biology* 169, 459-470, doi:10.1083/jcb.200410100 (2005).
- 27 Zaidel-Bar, R. Cadherin adhesome at a glance. *Journal of cell science* 126, 373-378, doi:10.1242/jcs.111559 (2013).
- 28 Guo, Z. et al. E-cadherin interactome complexity and robustness resolved by quantitative proteomics. *Science signaling* 7, rs7, doi:10.1126/scisignal.2005473 (2014).
- 29 Yamada, S., Pokutta, S., Drees, F., Weis, W. I. & Nelson, W. J. Deconstructing the cadherin-catenin-actin complex. *Cell* 123, 889-901, doi:10.1016/j.cell.2005.09.020 (2005).
- 30 Drees, F., Pokutta, S., Yamada, S., Nelson, W. J. & Weis, W. I. Alpha-catenin is a molecular switch that binds E-cadherin-beta-catenin and regulates actin-filament assembly. *Cell* 123, 903-915, doi:10.1016/j.cell.2005.09.021 (2005).
- 31 Kovacs, E. M. et al. N-WASP regulates the epithelial junctional actin cytoskeleton through a non-canonical post-nucleation pathway. *Nature cell biology* 13, 934-943, doi:10.1038/ncb2290 (2011).
- 32 Engl, W., Arasi, B., Yap, L. L., Thiery, J. P. & Viasnoff, V. Actin dynamics modulate mechanosensitive immobilization of E-cadherin at adherens junctions. *Nature cell biology* 16, 587-594, doi:10.1038/ncb2973 (2014).
- 33 Hyman, A. A., Weber, C. A. & Julicher, F. Liquid-liquid phase separation in biology. *Annual review of cell and developmental biology* 30, 39-58, doi:10.1146/annurev-cellbio-100913-013325 (2014).
- 34 Li, P. et al. Phase transitions in the assembly of multivalent signalling proteins. *Nature* 483, 336-340, doi:10.1038/nature10879 (2012).
- 35 Zhang, J. et al. Actin at cell-cell junctions is composed of two dynamic and functional populations. *Journal of cell science* 118, 5549-5562, doi:10.1242/jcs.02639 (2005).
- 36 Yao, M. et al. Force-dependent conformational switch of alpha-catenin controls vinculin binding. *Nat Commun* 5, 4525, doi:10.1038/ncomms5525 (2014).
- 37 Yonemura, S., Wada, Y., Watanabe, T., Nagafuchi, A. & Shibata, M. alpha-Catenin as a tension transducer that induces adherens junction development. *Nature cell biology* 12, 533-542, doi:10.1038/ncb2055 (2010).
- 38 Peng, X., Maiers, J. L., Choudhury, D., Craig, S. W. & DeMali, K. A. alpha-Catenin uses a novel mechanism to activate vinculin. *J Biol Chem* 287, 7728-7737, doi:10.1074/jbc.M111.297481 (2012).
- 39 Abe, K. & Takeichi, M. EPLIN mediates linkage of the cadherin catenin complex to F-actin and stabilizes the circumferential actin belt. *Proc Natl Acad Sci U S A* 105, 13-19, doi:10.1073/pnas.0710504105 (2008).
- 40 Peng, X., Cuff, L. E., Lawton, C. D. & DeMali, K. A. Vinculin regulates cell-surface E-cadherin expression by binding to beta-catenin. *Journal of cell science* 123, 567-577, doi:10.1242/jcs.056432 (2010).
- 41 Sumida, G. M., Tomita, T. M., Shih, W. & Yamada, S. Myosin II activity dependent and independent vinculin recruitment to the sites of E-cadherin-mediated cell-cell adhesion. *BMC Cell Biol* 12, 48, doi:10.1186/1471-2121-12-48 (2011).
- 42 Case, L. B. et al. Molecular mechanism of vinculin activation and nanoscale spatial organization in focal adhesions. *Nature cell biology*, doi:10.1038/ncb3180 (2015).
- 43 Krause, M., Dent, E. W., Bear, J. E., Loureiro, J. J. & Gertler, F. B. Ena/VASP proteins: regulators of the actin cytoskeleton and cell migration. *Annu Rev Cell Dev Biol* 19, 541-564 (2003).
- 44 Leerberg, J. M. et al. Tension-sensitive actin assembly supports contractility at the epithelial zonula adherens. *Curr Biol* 24, 1689-1699, doi:10.1016/j.cub.2014.06.028 (2014).